ISSN 2587-1366

TUJE

TURKISH JOURNAL OF ENGINEERING

VOLUME 6 ISSUE 4 OCTOBER 2022

Dr. Ghazi DROUBI
Robert Gordon University Engineering Faculty
Scotland, UK

JOURNAL SECRETARY

Nida DEMİRTAŞ
nidademirtas@mersin.edu.tr

TURKISH JOURNAL OF ENGINEERING (TUJE)

Turkish Journal of Engineering (TUJE) is a multi-disciplinary journal. The Turkish Journal of Engineering (TUJE) publishes the articles in English and is being published 4 times (January, April, July and October) a year. The Journal is a multidisciplinary journal and covers all fields of basic science and engineering. It is the main purpose of the Journal that to convey the latest development on the science and technology towards the related scientists and to the readers. The Journal is also involved in both experimental and theoretical studies on the subject area of basic science and engineering. Submission of an article implies that the work described has not been published previously and it is not under consideration for publication elsewhere. The copyright release form must be signed by the corresponding author on behalf of all authors. All the responsibilities for the article belongs to the authors. The publications of papers are selected through double peer reviewed to ensure originality, relevance and readability.

AIM AND SCOPE

The Journal publishes both experimental and theoretical studies which are reviewed by at least two scientists and researchers for the subject area of basic science and engineering in the fields listed below:

Aerospace Engineering
Environmental Engineering
Civil Engineering
Geomatic Engineering
Mechanical Engineering
Geology Science and Engineering
Mining Engineering
Chemical Engineering
Metallurgical and Materials Engineering
Electrical and Electronics Engineering
Mathematical Applications in Engineering
Computer Engineering
Food Engineering

PEER REVIEW PROCESS

All submissions will be scanned by iThenticate® to prevent plagiarism. Author(s) of the present study and the article about the ethical responsibilities that fit PUBLICATION ETHICS agree. Each author is responsible for the content of the article. Articles submitted for publication are priorly controlled via iThenticate ® (Professional Plagiarism Prevention) program. If articles that are controlled by iThenticate® program identified as plagiarism or self-plagiarism with more than 25% manuscript will return to the author for appropriate citation and correction. All submitted manuscripts are read by the editorial staff. To save time for authors and peer-reviewers, only those papers that seem most likely to meet our editorial criteria are sent for formal review. Reviewer selection is critical to the publication process, and we base our choice on many factors, including expertise, reputation, specific recommendations and our own previous experience of a reviewer's characteristics. For instance, we avoid using people who are slow, careless or do not provide reasoning for their views, whether harsh or lenient. All submissions will be double blind peer reviewed. All papers are expected to have original content. They should not have been previously published and it should not be under review. Prior to the sending out to referees, editors check that the paper aim and scope of the journal. The journal seeks minimum three independent referees. All submissions are subject to a double blind peer review; if two of referees gives a negative feedback on a paper, the paper is being rejected. If two of referees gives a positive feedback on a paper and one referee negative, the editor can decide whether accept or reject. All submitted papers and referee reports are archived by journal Submissions whether they are published or not are not returned. Authors who want to give up publishing their paper in TUJE after the submission have to apply to the editorial board in written. Authors are responsible from the writing quality of their papers. TUJE journal will not pay any copyright fee to authors. A signed Copyright Assignment Form has to be submitted together with the paper.

PUBLICATION ETHICS

Our publication ethics and publication malpractice statement is mainly based on the Code of Conduct and Best-Practice Guidelines for Journal Editors. Committee on Publication Ethics (COPE). (2011, March 7). Code of Conduct and Best-Practice Guidelines for Journal Editors. Retrieved from http://publicationethics.org/files/Code%20of%20Conduct_2.pdf

PUBLICATION FREQUENCY

The TUJE accepts the articles in English and is being published 4 times (January, April, July and October) a year.

CORRESPONDENCE ADDRESS

Journal Contact: tuje@mersin.edu.tr

CONTENTS

Volume 6 – Issue 4

RESEARCH ARTICLES

REVIEW ARTICLES

Turkish Journal of Engineering
https://dergipark.org.tr/en/pub/tuje
e-ISSN 2587-1366

3-dimensional printing of PLA scaffolds for medical applications

Azade Yelten*[1], Mehmet Halit Öztürk [1], Suat Yılmaz [1]

[1]*Istanbul University-Cerrahpasa, Engineering Faculty, Metallurgical and Materials Engineering Department, Istanbul, Turkey*

Keywords
3d Printing
PLA
Scaffold
Porosity
Medical Applications

ABSTRACT

Scaffolds encourage the new tissue formation through biological substitution of the damaged or lost tissues. Therefore, scaffold characteristics become more important and should be precisely controlled. Production of scaffolds using a three dimensional (3d) printer appears as a promising method in terms of enabling homogeneous pore distribution and uniform pore size arrangement. In this study, polylactic acid (PLA) scaffold structures were obtained through 3d printing, based on the design parameters such as the scaffold geometry, porosity (%), pore shape, pore size, and the pore interconnectivity. An open source computer-aided design (CAD) program (Interface Scaffold) was employed to design the PLA scaffolds. Scaffold structures with ~72% porosity were generated through a 3D Systems Cube 2nd Generation 3d printer. The design parameters have been optimized by the scaffold design software tool, which includes different unit cells, i.e. Schwartz P, Schwartz D, Gyroid, Skeletal (1-4), Neovius and W (iWP) for designing scaffold structures through mathematical formulations. It was found out that the mean pore size of the 3d-printed Gyroid unit cell scaffolds vary between 1.9 mm and ~4.54 mm according to the microstructural observations done by a scanning electron microscope (SEM).

1. INTRODUCTION

Three dimensional (3d) printing systems play a significant role in fulfilling the demand for biomedical applications. It is possible to enable better anatomic compatibility between the defect area and 3d-printed patient-specific implant materials so that a better healing process can be managed. Complicated shaped implant materials can be designed and produced one-to-one coherent to the damaged tissue such as bone fractures by using the computed tomography (CT) scan and rapid prototyping systems collaboration. In this context, researchers pay considerable attention to the porous materials, which are frequently utilized as bone scaffolds in hard tissue implants. Porous implants not only reduce the elastic (E) modulus of the material but also ensure superior osseointegration with the bone tissue and the implant material by facilitating the migration of the bone cells through the pores. An interconnected pore network on the implant surface provide potential surface area for the cells to adhere, grow and proliferate. The increased surface area owing to the porous structure of the material enhances the biological interactions between the material and the bone tissue so that osseointegration is promoted. Besides, the decreased E-modulus allows the implant material and the bone tissue properly share the applied load compatible with the human anatomy; hence, stress shielding can be avoided [El-Hajje et al. 2014; Wang et al. 2016]. Since bone is a structure composed of parts with different mechanical strength, mimicking the E-modulus characteristics of the host tissue, i.e. spongy (cancellous) bone and cortical bone, is an inevitable condition for the implant materials that are employed for hard tissue treatments. Therefore, porous materials draw interest in terms of possessing E-modulus values close to that of the spongy bone. Porous structures improve the mechanical integrity between the implant material and tissue while accelerating the bone growth depending on the interconnected pore network that assures the continuous transition of the body fluids, nutrition, and oxygen towards the open pores. Thus, it should be emphasized that porous structures function for both better mechanical fixation and osseointegration [Wang et al. 2016; Ryan et al. 2008; Limmahakhun et al, 2017].

There are several factors that should be taken into consideration to design and prepare a convenient bone scaffold for the target hard tissue. Pore size, por shape,

* **azade.yelten@iuc.edu.tr**

*(azade.yelten@iuc.edu.tr) ORCID ID 0000 – 0001 – 6089 – 6257
(mehmethalitozturk@gmail.com) ORCID ID 0000 – 0003 – 1855 – 4477
(syilmaz@iuc.edu.tr) ORCID ID 0000 – 0002 – 6092 – 9319

Cite this article

Yelten A, Öztürk M H & Yılmaz S (2022). 3-dimensional printing of PLA scaffolds for medical applications. Turkish Journal of Engineering, 6(4), 262-267

Research Article / DOI: 10.31127/tuje.958192

Received: 27/06/2021; Accepted: 26/11/2021

pore interconnectivity, porosity (%) and strut (cell wall) thickness are the essential criteria that should be elaborately designated before the production process [Van Bael et al. 2011; Kang et al. 2017]. Indeed, in order to realize rapid bone growth, porosity (%) amount should be in the range (~75-85%) that will enable the implant material to have an E-modulus value close to that of the spongy bone [Wally et al. 2015]. Pore size is reported to be larger than 100 μm for the scaffolds that are intended to be used for orthopedic applications to provide better biological interactions between the scaffold and bone tissue and therefore, rapid bone regeneration [Papadimitropoulos et al. 2007; Tarafder et al. 2013]. Recently, 3d printing has been widely implemented as an efficient way to produce scaffold structures with controlled pore size, porosity %, pore interconnectivity, strut thickness, etc. for biomedical applications [Wally et al. 2015; Bose et al. 2012]. As the scaffold structures are employed as the templates for tissue regeneration, scaffolds made of different materials such as metallic, ceramic, polymer or composite of them are extensively used in tissue engineering applications to promote the repairing process. From this point of view, it was aimed to design polylactic acid (PLA) scaffolds, which have suitable design characteristics to be the template candidates for regeneration.

PLA is a biocompatible material widely used in biomedical applications such as orthopedic implants/prostheses (pins, screws, sutures, synthetic constructs, plates, etc.), tissue engineering scaffolds, dental resin, drug delivery systems and theranostics, etc. PLA is defined as a biodegradable material, and the degradation products of PLA are not harmful to the body. This situation enables PLA to be utilized in the demands above [Navarro et al. 2005; Felfel et al. 2012; Senatov et al. 2016; Da Silva et al. 2018; DeStefano et al. 2020; Gendviliene et al. 2020; Wu et al. 2020]. Although PLA is well known for being bioresorbable, its mechanical properties limit the usage areas to non-load bearing applications. Therefore, a composite can be prepared, where PLA is reinforced by bioceramics like hydroxyapatite (HA) and bioactive glasses. Consequently, the mechanical strength could be increased, and osseointegration of PLA could be enhanced, as noted in the literature [Navarro et al. 2005; Serra et al. 2013; Senatov et al. 2016; DeStefano et al. 2020; Gendviliene et al. 2020; Wu et al. 2020]. These composites can be implemented for bone defects to provide bone regeneration. Moreover, since PLA is a biodegradable polymer material, it is commonly used as a fixation device like screws and plates (Felfel et al., 2012). It is aimed to overcome the stress shielding problem that arises when metallic materials are employed due to the mismatch between the E-modulus values of the metallic implant material and hard tissue. In fact, Stener et al. 2010 demonstrated in a study carried out on 77 patients that poly-L-lactic acid (PLLA) screws used in the tibia and femur showed similar performance as metal screws during tendon reconstruction [Da Silva et al. 2018].

PLA scaffolds were developed with a computer aided design (CAD) software and manufactured via 3d printing. Microstructure and porosity properties of the scaffolds were investigated with a scanning electron microscope (SEM) and the operated scaffold design software.

2. METHOD

2.1. 3d Printer & PLA Filament

Porous scaffold structures were produced by employing a 3D Systems Cube 2nd Generation 3d printer. This 3d printer (**Fig. 1**) works with the fused deposition modelling (FDM) principle. FDM technique is based on melting and then layer by layer deposition of a thermoplastic material [Ngo et al. 2018]. In this research, polylactic acid (PLA) -a recyclable biodegradable thermoplastic polymer material- is used as the precursor in filament form. Properties of the 3d printer and PLA starting material are given in **Table 1**. Scaffold structures were obtained taking into account the design parameters such as porosity (%), pore interconnections, strut thickness and pore shape. Firstly, the properties and design parameters of the scaffold structures were investigated through a detailed literature research. By comparing the previous studies [Wang et al. 2016; Bose et al. 2012; Leong et al. 2003; Holzapfel et al. 2013; Cheung et al. 2007; Khang 2017], the characteristics and design parameters of an ideal scaffold structure were determined. CAD design of the scaffold structures were realized by benefitting from the open source software tool, i.e. "*Interface Scaffold"* presented and reported by Dinis et al. 2014 and Castro et al. 2019.

2.2. Designing the Scaffold Structures

Scaffold structures can be designed with various CAD programs. Several researchers managed to design scaffolds by employing already existing CAD programs such as Solidworks [Wang et al. 2017], CASTS (for tissue engineering scaffolds) [Sudarmadji et al. 2012], Pro/Engineer [Naing et al. 2005], CATE [Nam et al. 2004] and MATLAB [Monkova et al. 2017]. Researchers have a tendency to create scaffolds by associating unit cell structures. Creating scaffold designs by combining the unit cells with different geometric shapes is pretty convenient. For example, Chantarapanich et al. 2012, designed scaffolds with a 119 polyhedron unit cell model in their work. Although CAD programs can be directly used for designing the scaffold structures, actually it can be occasionally difficult to realize such complicated designs. Scaffold structures may have sophisticated geometries and the complex design parameters may obstruct the possibility of a feasible design, especially for the researchers who newly begin creating scaffolds. Therefore, software programs, which form scaffold structures from unit cells can be evaluated as a remedy. Scaffold structures can be easily created by selecting the unit cell type and determining the design parameters with these scaffold designing software programs. Dinis et al. 2014 presented an open source software tool, which is named as "*Interface Scaffold"* for this purpose and the mentioned tool includes different unit cells, i.e. Schwartz P, Schwartz D, Gyroid, Skeletal (1-4), Neovius and W (iWP) for designing scaffold structures through mathematical formulations. Unit cells are converted to

the scaffold structures according to the x-y-z dimensions and pore size values that are manually entered by the user [Dinis et al. 2014].

In the current work, Interface Scaffold software tool was used to design the scaffold structures. The user can individually decide the design parameters such as scaffold geometry, scaffold dimensions, porosity (%), pore size, pore shape, etc. utilizing the Interface Scaffold software tool (**Fig. 2**). A 15 x 15 x 30 mm *Gyroid* unit cell scaffold structure was designed via the Interface Scaffold software tool [Dinis et al. 2014; Castro et al. 2019]. Moreover, it can be stated that the Gyroid unit cell has a suitable morphology for tissue regeneration applications due to its superior pore interconnectivity [Khang 2017; Dinis et al. 2014; Castro et al. 2019].

Figure 1. Picture of the 3D Systems Cube 2nd generation 3d printer

Designs that are created with Interface Scaffold software tool can be saved directly in *stl* file type. Since the 3d printer functions with the stl files, the designs should be transferred to the 3d printer slicing programs. Hence, the design file was saved as a stl file. Then, the ready-to-print stl file was transferred to the Cube 2nd generation 3d printer's own *Cubify* software. Pre-printing parameter selections were done with this software. In this context, the position of the part on the tray, number of the layers, printing time, support structure usage (support and/or raft) and the raw material (PLA or ABS) adjustments were carried out (**Fig. 3**). Following the necessary adjustments, the production time of the scaffold structure was revealed as 48 min. by the Cubify software. According to the printing software, thickness of each molten PLA layer is maintained as 0.25 mm to enable the maximum printing resolution. The z length of the designed scaffold was determined as 32.25 mm (including the support parts) by the software. When the z length (32.25 mm) is divided to the layer thickness (0.25 mm), it is found out that the scaffold structure will be composed of 129 layers. This indicates that the 3d part will be ready after the sequential printing of 129 PLA layers.

Table 1. Features of the 3D Systems Cube 2nd Generation 3d Printer and polylactic acid (PLA) filament used for 3d printing [3D Systems 2014]

Property	Description/Value
Technology	Fused Deposition Modelling (FDM)
Max. print area	140 x 140 x 140 mm
Material	Durable thermoplastic polymers (ABS and PLA)
Layer thickness	250 µm
Support and raft	Fully automated
Cartridge	Roll filament
Filament diameter	1.75 mm
Nozzle operating temperature	280 °C
Adhesive for the printing tray	Water based adhesive

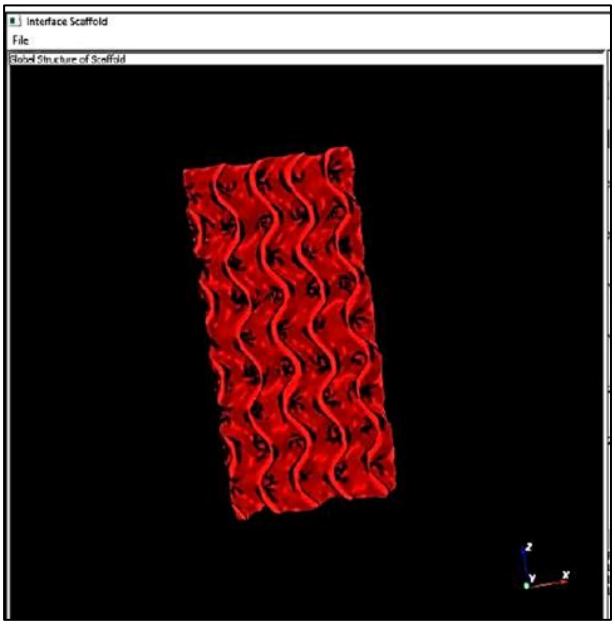

Figure 2. Design of the Gyroid unit cell scaffold structure

2.3. 3d Printing Process

The settings of the 3d printer has to be performed before each printing process. First, the thermoplastic filament (PLA) is fitted into the 3d printer. After selecting the new filament settings from the 3d printers' software, the print head automatically moves to the appropriate position. The small heater inside the 3d printer begins to heat up to 250 °C. The tip of the filament is then inserted through the hole that is placed on the top of the print head. The 3d printer transfers the filament to the heater by means of gear wheels. A little amount of filament may spill from the nozzle tip when the heater is completely filled with the material. However, this situation points out that the filament is properly connected to the printer. Then, the distance between the print head and the tray (z-axis) should be arranged. Since a fault in the z axis will disrupt the layers, this adjustment should be optimal. The 3d printer's print head and the tray automatically take the adjustment position while calibration is in progress. Afterwards, an A4 paper is placed between the

nozzle tip and the tray. The nozzle tip and the tray are brought closer to each other by leaving a distance such that an A4 paper can move smoothly. When this implementation is completed, the 3d printer is ready to print. The filament placement and calibration of the 3d printer steps were repeated before each printing practice.

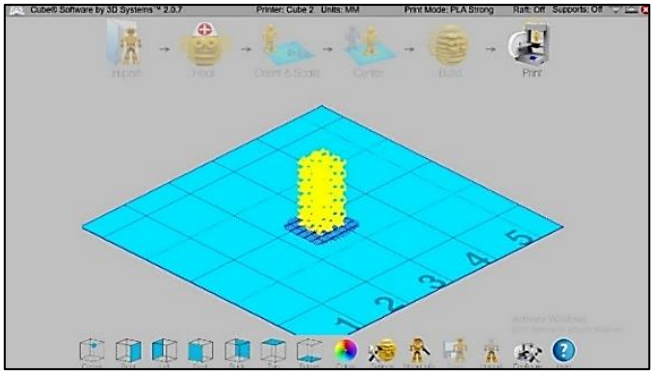

Figure 3. Ready-to-print version of the scaffold (Cubify software)

Within the 3d printing process (**Fig. 4**), primarily the water-based adhesive of the 3d printer was applied to the surface of the tray before printing starts. This adhesive allows the first molten filament layer to adhere to the tray surface. If the first layer does not adhere properly to the tray, then the following layers will be corrupted. As a result, the printing quality will decrease. The tray was removed from the 3d printer after the printing process was completed. The water-based adhesive of the 3d printer can be simply dissolved in water in approximately 5 min. so that the printed scaffold structure can be easily separated from the tray. The support parts of the scaffold structure can be extracted by applying slight mechanical impacts. The 3d printing process finished after separating the support parts and took totally 1 h and 5 min. including the pre-printing, printing (48 min.) and post-printing stages. Microstructural features of the 3d-printed PLA scaffolds were investigated with a FEI Quanta FEG 450 branded SEM and porosity value of the scaffolds was determined with the Interface Scaffold software tool.

Figure 4. Pictures of **(a)** the 3d printing process of the PLA scaffold and **(b)** the screen view of the 3d printer during the printing procedure

3. RESULTS & DISCUSSION

The 3d-printed porous scaffold structures were properly obtained by using the FDM method. It was macroscopically observed that the 3d-printed PLA scaffolds have a highly porous structure with superior interconnectivity and no deformities were recognized on the surface or general construction of the 3d-printed parts. It was proven that the actual dimensions (15 x 15 x 30 mm) of the 3d-printed PLA scaffolds are compatible with the CAD design created with the Interface Scaffold open source software tool (**Fig. 5**). The ellipsoid pore shape of the scaffolds can be realized from the SEM images **(Fig. 6)** of the top and lateral surfaces of the scaffolds. The 3d-printed scaffold structures possess a porosity of 72%, which was assigned by the employed scaffold design software tool. 72% porosity is appropriate for the tissue engineering applications, where the healing process is accelerated and osseointegration between the tissue and material is enhanced due to the highly porous structure of the scaffolds [Wang et al. 2016; Ryan et al. 2008; Limmahakhun et al. 2017; Papadimitropoulos et al. 2007; Tarafder et al. 2013]. The mean longitudinal size of the pores and the mean latitudinal size of the pores were measured as ~4.54 mm and ~1.9 mm from the SEM images **(Fig. 6)** of the top and lateral surfaces of the 3d-printed PLA parts by means of the digital ruler in the software of the SEM facility.

The SEM images in **Fig. 7** clearly indicate the layer-by-layer deposition of the fused PLA filaments around the pore walls. The 3d-printed layers have a pretty smooth surface despite the unattached tiny molten filament pieces. No gaps, voids or looseness between the molten PLA layers were detected, in spite of the highly porous structure of the part. This has demonstrated the effectiveness of the 3d-printing techniques in terms of generating components with complex geometries.

4. CONCLUSION

PLA is a biocompatible material widely used in biomedical applications and a popular material that can effectively function in 3d printing mechanisms. Recently, the production of PLA scaffolds with complicated structures for different medical demands such as orthopedic implants or tissue engineering studies has become more attractive. Design parameters of the scaffold structures are very important for the target biomedical application. Scaffolds with complex morphologies and more accurate characteristics like porosity (%), pore interconnectivity, etc. have been produced by employing 3d printing as a new generation manufacturing method. Since the design parameters influence the application area of the scaffold structures, they should be considered carefully. At this point, 3d printing offers a precise control of the design parameters. In the present report, Gyroid unit cell PLA scaffolds, which were one-to-one compatible with the CAD data, were practically obtained by using a 3d printer that works based on the FDM principle.

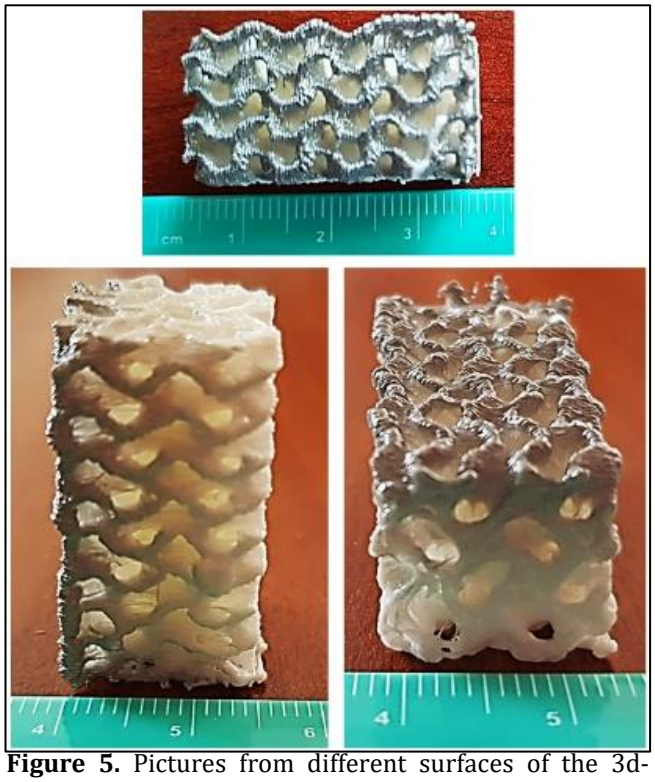

Figure 5. Pictures from different surfaces of the 3d-printed PLA scaffolds

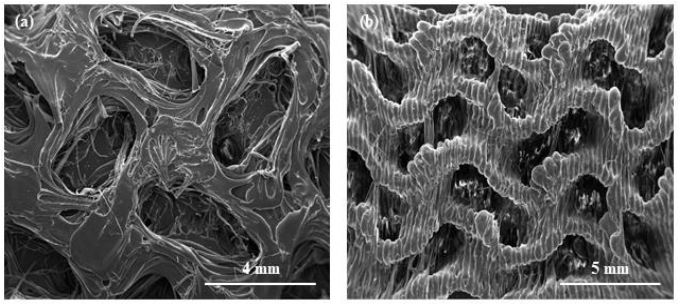

Figure 6. SEM images of the 3d-printed PLA scaffolds (**a:** top surface, **b:** lateral surface)

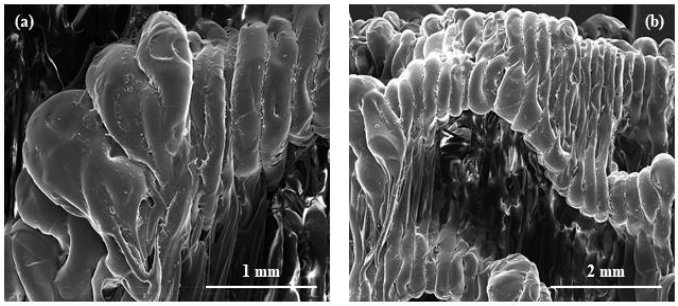

Figure 7. SEM images of the pore walls of the 3d-printed PLA scaffolds

ACKNOWLEDGEMENT

The authors cordially thank to Dr. Rui B. Ruben (Polytechnic Institute of Leiria, Portugal) for providing the "*Interface Scaffold"* open source software tool.

Author contributions

Azade Yelten: Determining the aim and creating the methodology of the study, Analyzing the characterization data, Writing-Reviewing and Editing the manuscript. **Mehmet Halit Öztürk:** Designing the Scaffold Structures, Printing Process, Help with the preparation of the manuscript draft. **Suat Yılmaz:** Coordinating the study.

Conflicts of interest

The authors declare no conflicts of interest.

REFERENCES

Bose S, Roy M & Bandyopadhyay A (2012). Recent advances in bone tissue engineering scaffolds. Trends in Biotechnology, 30(10), 546-554.

Castro A P G, Ruben R B, Gonçalves S B, Pinheiro J, Guedes J M & Fernandes P R (2019) Numerical and experimental evaluation of TPMS Gyroid scaffolds for bone tissue engineering. Computer Methods in Biomechanics and Biomedical Engineering, 22(6), 567-573.

Chantarapanich N, Puttawibul P, Sucharitpwatskul S, Jeamwatthanachai P, Inglam S & Sitthiseripratip K (2012). Scaffold library for tissue engineering: A geometric evaluation. Computational and Mathematical Methods in Medicine, 407805.

Cheung H Y, Lau K T, Lu T P & Hui D (2007). A critical review on polymer-based bio-engineered materials for scaffold development. Composites Part B: Engineering, 38(3), 291-300.

Da Silva D, Kaduri M, Poley M, Adir O, Krinsky N, Shainsky-Roitman J & Schroeder A (2018). Biocompatibility, biodegradation and excretion of polylactic acid (PLA) in medical implants and theranostic systems. Chemical Engineering Journal, 15(340), 9-14.

DeStefano V, Khan S & Tabada A (2020). Applications of PLA in modern medicine. Engineered Regeneration 1, 76-87.

Dinis J C, Morais T F, Amorim P H J, Ruben R B, Almeida H A, Inforçati P N, Bartolo P J & Silva J V L (2014). Open source software for the automatic design of scaffold structures for tissue engineering applications. Procedia Technology, 16, 1542-1547.

El-Hajje A, Kolos E C, Wang J K, Maleksaeedi S, He Z, Wiria F E, Choong C & Ruys A J (2014). Physical and mechanical characterization of 3D-printed porous titanium for biomedical applications. Journal of Materials Science: Materials in Medicine, 25(11), 2471-2480.

Felfel R M, Ahmed I, Parsons A J, Haque P, Walker G S & Rudd C D (2012). Investigation of crystallinity, molecular weight change, and mechanical properties of PLA/PBG bioresorbable composites as bone fracture fixation plates. Journal of Biomaterials Applications, 26, 765-789.

Gendviliene I, Simoliunas E, Rekstyte S, Malinauskas M, Zaleckas L, Jegelevicius D, Bukelskiene V & Rutkunas V (2020). Assessment of the morphology and dimensional accuracy of 3D printed PLA and PLA/HAp scaffolds. Journal of the Mechanical Behavior of Biomedical Materials, 104, 103616.

Holzapfel B M, Reichert J C, Schantz J T, Gbureck U, Rackwitz L, Nörth U, Jakob F, Rudert M, Groll J & Hutmacher D W (2013). How smart do biomaterials need to be? A translational science and clinical point of view. Advanced Drug Delivery Reviews, 65(4), 581-603.

Kang B H, Park M H & Lee K A (2017). Effect of strut thickness on room and high temperature compressive properties of block-type Ni-Cr-Al powder porous metals. Archives of Metallurgy and Materials, 62(2B), 1329-1334.

Khang G (2017) Handbook of Intelligent Scaffolds for Tissue Engineering and Regenerative Medicine 2nd Edition. Jenny Stanford Publishing. ISBN: 9789814745123.

Leong K F, Cheah C M & Chua C K (2003). Solid freeform fabrication of three-dimensional scaffolds for engineering replacement tissues and organs. Biomaterials, 24(13), 2363-2378.

Limmahakhun S, Oloyede A, Sitthiseripratip K, Xiao Y & Yan C (2017). 3d-printed cellular structures for bone biomimetic implants. Additive Manufacturing, 15, 93-101.

Monkova K, Monka P, Zetkova I, Hanzl P & Mandulak D (2017). Three approaches to the gyroid structure modelling as a base of lightweight component produced by additive technology. 2nd International Conference on Computational Modeling, Simulation and Applied Mathematics (CMSAM 2017), DEStech Transactions on Computer Science and Engineering, 124-129, China.

Naing M W, Chua C K, Leong K F & Wang Y. (2005). Fabrication of customized scaffolds using computer-aided design and rapid prototyping techniques. Rapid Prototyping Journal, 11(4), 249-259.

Nam J, Starly B, Darling A & Sun W (2004). Computer aided tissue engineering for modeling and design of novel tissue scaffolds. Computer-Aided Design and Applications, 1(1-4), 633-640.

Navarro M, Ginebra M P, Planell J A, Barrias C C & Barbosa M A (2005). In vitro degradation behavior of a novel bioresorbable composite material based on PLA and a soluble CaP glass. Acta Biomaterialia, 1, 411-419.

Ngo T D, Kashani A, Imbalzano G, Nguyen K T Q & Hui D (2018). Additive manufacturing (3D printing): A review of materials, methods, applications and challenges. Composites Part B: Engineering, 143, 172-196.

Papadimitropoulos A, Mastrogiacomo M, Peyrin F, Molinari E, Komlev V S, Rustichelli F & Cancedda R (2007). Kinetics of in vivo bone deposition by bone marrow stromal cells within a resorbable porous calcium phosphate scaffold: an x-ray computed microtomography study. Biotechnology and Bioengineering, 98(1), 271-281.

Ryan G E, Pandit A S & Apatsidis D P (2008). Porous titanium scaffolds fabricated using a rapid prototyping and powder metallurgy technique. Biomaterials, 29(27), 3625-3635.

Senatov F S, Niaza K V, Zadorozhnyy M Yu, Maksimkin A V, Kaloshkin S D & Estrin Y Z (2016). Mechanical properties and shape memory effect of 3D-printed PLA-based porous scaffolds. Journal of the Mechanical Behavior of Biomedical Materials, 57, 139-148.

Serra T, Mateos-Timoneda M A, Planell J A & Navarro M (2013). 3D printed PLA-based scaffolds: A versatile tool in regenerative medicine. Organogenesis, 9(4), 239-244.

Stener S, Ejerhed L, Sernert N, Laxdal G, Rostgard-Christensen L & Kartus J (2010). A long-term, prospective, randomized study comparing biodegradable and metal interference screws in anterior cruciate ligament reconstruction surgery: radiographic results and clinical outcome. The American Journal Sports Medicine, 38,1598-1605.

Sudarmadji N, Chua C K & Leong K F (2012). The development of computer-aided system for tissue scaffolds (CASTS) system for functionally graded tissue-engineering scaffolds. Methods in Molecular Biology, 868, 111-123.

Tarafder S, Balla V K, Davies N M, Bandyopadhyay A & Bose S (2013). Microwave sintered 3D printed tricalcium phosphate scaffolds for bone tissue engineering. Journal of Tissue Engineering and Regenerative Medicine, 7(8), 631-641.

Van Bael S, Kerckhofs G, Moesen M, Pyka G, Schrooten J & Kruth J P (2011). Micro-CT-based improvement of geometrical and mechanical controllability of selective laser melted Ti6Al4V porous structures. Materials Science and Engineering A, 528(24), 7423-7431.

Wally Z J, Van Grunsven W, Claeyssens F, Goodall R & Reilly G C (2015). Porous titanium for dental implant applications. Metals, 5(4), 902-1920.

Wang X, Xu S, Zhou S, Xu W, Leary M, Choong P, Qian M, Brandt M & Xie Y M (2016). Topological design and additive manufacturing of porous metals for bone scaffolds and orthopaedic implants: a review. Biomaterials, 83, 127-141.

Wang Y, Wang K, Li X, Wei Q, Chai W, Wang S, Che Y, Lu T & Zhang B (2017). 3D fabrication and characterization of phosphoric acid scaffold with a HA/β-TCP weight ratio of 60:40 for bone tissue engineering applications. PLoS One, 12(4), e0174870.

Wu D, Spanou A, Diez-Escudero A & Persson C (2020). 3D-printed PLA/HA composite structures as synthetic trabecular bone: A feasibility study using fused deposition modeling. Journal of the Mechanical Behavior of Biomedical Materials, 103, 103608.

3D Systems Cube 2nd generation 3d printer user manual (2014).

Turkish Journal of Engineering
https://dergipark.org.tr/en/pub/tuje
e-ISSN 2587-1366

Risk assessment with the fuzzy logic method for Ankara OIZ environmental waste water treatment plant

Fatma Erdem

Turkish Medicines and Medical Devices Agency, 06520, Sıhhıye, Ankara, Turkey

Keywords
Risk management
Modelling
Fuzzy logic
Waste water treatment plant

ABSTRACT

In this study, occupational safety risk assessment has been performed for Ankara Chamber of Industry 2nd and 3rd Organized Industrial Zone (OIZ) Regional Directorate - Environmental Waste Water Treatment Plant (WWTP) by fuzzy logic method. In the literature, there are lots of risk assessment methodologies. These methods for the risk level do not give accurate results in systems such as WWTPs with a lot of complexity and variability. Also, these methods include strict lines and are not reflecting the practical issues of the real-world applications. For this reason, these methods are to be adopted by the use of fuzzy logic. Fuzzy Logic Risk Analysis Model which gives more realistic results compared to traditional methods based on probability. For fuzzy safety risk assessment firstly membership functions for input and output are created and values risk assessment input data is blurred then Fuzzy Risk Priority Number (FRPN) is determined in the Matlab 2013a software program. In this study a risk matrix merged with Fuzzy Logic model is developed to enhance the risk assessment process which is dealing with uncertainties that arise in each phase of the risk assessment process. RPN values were investigated and compared by 5x5 matrix and fuzzy logic method.

1. INTRODUCTION

As a general definition, risk is a negative possibility that is not desired to be encountered (Łój-Pilch at al. 2018). As in every field, it becomes very important in the disruption of urban services that are carried out without risk and in situations that directly concern public health (Łój-Pilch and Zakrzewska 2020). Water and wastewater management is at the top of the list of urban services involving high risks. Disruption of the sustainability of these services, which are closely related to the environment and human health or any decrease in service quality, may have negative consequences. Environmental damage or health loss that may occur in case of risk is much more important than financial losses (Kudłak et al. 2016, Cossio et al. 2019).

The term "Risk Management" was first used in the United States of America in the late 1950s (Nicoleta et al. 2020). In the early days, it was dealt with insurance and took part in insurance. Thus, risk management can be defined as planning, organizing, managing and controlling the resources and activities required to control the unexpected losses that may occur in the organization at the lowest cost. Risk management includes the stages of identifying and evaluating risks, responding to risks, regularly reviewing and reporting risks (Emhan 2009).

Water resources in the world are decreasing rapidly. Among these resources, water resources of potable quality decreased and reached the point of depletion (Yılmaz 2015). On the other hand, waste water released to receiving environments without being treated in a way causes pollution of water resources whose amount is decreasing day by day and deserve more interest recently (Ozkan et al. 2013). For this reason, waste water should be treated in order not to contaminate existing water resources and to use water resources more efficiently (Edokpayi et al. 2017).

Necessary precautions should be taken in order to create a healthy and safe work environment in WWTPs

* **Corresponding Author**
*(fatmaduran82@gmail.com) ORCID ID 0000-0002-6014-6664

Cite this article
Erdem F (2022). Risk assessment with the fuzzy logic method for Ankara OIZ environmental waste water treatment plant. Turkish Journal of Engineering, 6(4), 268-275

Research Article / DOI: 10.31127/tuje.975623
Received: 28/07/2021; Accepted: 10/12/2021

and to prevent possible work accidents (Malakahmad et al. 2012).

In this context, safety measures to prevent accidents and dangers that may occur during the maintenance, repair and operation processes of WWTPs should be acted within the scope of occupational health and safety (OHS) (Güner 2018). WWTPs, which are classified as "very dangerous", contain many risks regarding occupational health and safety in terms of processes and working conditions. In determining the risks that may occur in WWTPs, in addition to the effects on occupational and worker health, it is necessary to determine the scope and size of their effects on the environment. Considering the negative environmental effects of the dangers in these facilities, it is important to re-evaluate and prioritize the risks. In occupational and worker safety, including environmental impacts as well as the activity and employee safety in the risk analysis will benefit both decision-makers and managers (El-Quliti et al. 2016).

Many neural network applications can used for, bioprocesses control and risk management systems (Özkan et al. 2010, Mete et al. 2012). Fuzzy logic is one of them and has proven to be very successful in a wide range of applications, with much commercial success. Risk analysis is a complex task that entails the consideration of many parameters which are, more often than not, very difficult to quantify. Fuzzy logic presents a natural way of modelling these vaguenesses, while also ensuring that human creativity and intuitivity, which is an essential ingredient for successful risk analysis. In literature, Bavani and Tabesh 2012, produced an algorithm by fuzzy for the risk management of the WWTP. Comprising probability of failure, intensity of probable damages and vulnerability of element were used for the calculation of operational risk and results showed that proposed algorithm is successful for risk management. Cabanillas et al. 2012, used fuzzy logic with a new methodology. Algorithm was based on 22 WWTP datas. Results showed that new method with fuzzy logic showed better and practical results than solid method. Alavipoor et al. 2016, used Fuzzy-WRASTIC new model for the risk management of Geographic Information System) environment. Surface water contamination risk in this area was divided into four ranges: low, medium, high and very high. High risk zones are much more than the others and the reasons discussed. Yel and Yalpir 2011, used fuzzy logic for municipal wastewater treatment plant (MWTP). A fuzzy-logic-based diagnosis system was developed to determine the primary treatment effluent quality in a MWTP. The measured data of variables were implemented into the Fuzzy Inference System (FIS) with Mamdani's method. The output approximations to real data remained in an acceptable range for a MWTP performance (89-96%). The averages and standard deviations of the model were also approximated closely as 93-98% and 89-97%, respectively. The resulting configuration proved a good modeling approach for MWTP effluent quality prediction15. Ghandi and Roozbahani 2020, used fuzzy Promthee V (Preference Ranking Organization Method for Enrichment Evaluation) technic for the selection of the most appropriate drinking water supply strategies in crisis conditions and applied for Tehran city. Model was solved through fuzzy and non-fuzzy method. Mirghafouri and Kousha 2015, used Fuzzy FMEA-AHP algorithm the risk of water transmission pipeline to Yazd. Results showed that failure of electromotor and electricity panels in pumping stations, reduction of height of river water level in water harvesting site and breakdown of main faucets in pipeline path are on high priority.

In this study risk management was investigated for Ankara Chamber of Industry 2nd and 3rd Organized Industrial Zone (OIZ) Regional Directorate WWTP by fuzzy logic method. The contribution of this paper to the literature is important due to the number of WWTPs operated in Turkey is increasing day by day. Each of the treatment plants are potential risk to safety. WWTPs contain many hazards from the operation, maintenance and repair in terms of both occupational health, safety and environment. Ankara OIZ Environmental WWTP is a new and big WWTP in Ankara and outlet stream is connected to Ankara Stream which joins with Sakarya river and pours into Sarıyer dam. With such risk analyzes carried out in this plant, it is aimed to reduce accidents and increase the working efficiency. Also, fuzzy 5x5 matrix type risk assessment method is never used for WWTP risk management studies before. For this first of all, the hazards were determined and then the risk value was calculated considering the probability of accidents and the effects of severity after they occur. The probability and severity values, which were the input data, were blurred and membership functions were created for the probability, severity and FRPN. Triangular membership functions were defined one by one for grading levels that are very low, low, medium, high and very high. A possible solution is proposed by modifying the risk matrix using a fuzzy logic model to deal with the uncertainties.

2. METHOD

2.1. Study Area: Waste Water Treatment Plant

The analyzed WWTP is located in Sincan. Domestic and industrial wastewater originating from factories and facilities in Ankara Chamber of Industry 2nd and 3rd Organized Industrial Zone is treated in a WWTP with a capacity of 2500 m^3/day by Advanced Biological Treatment process. The total industrial area in ASO (Ankara Chamber of Industry) 2nd and 3rd OIZ is approximately 400 ha, and there are 321 industrial parcels varying between 10000 m^2 and 200000 m^2 can be seen in Fig. 1. Currently, the number of active facilities is 90. The current amount of treated water is 1900 m^3/day. If the pollutant concentrations of the participant activities meet the discharge standards defined in the wastewater management system, they are connected to the sewerage system without any pre-treatment. The pollution values of the wastewater originating from the facilities that cannot meet this requirement are reduced to the discharge standard limits and released to the environment. Risk datas were defined with the expert about compressor, pump, electricity, lighting, wet floor etc. such as general risks for treatment plants.

Figure 1. WWTP plan

2.2. Hazard identification for WWTP

Hazards were grouped under 10 headings as electricity, chemical substances, compressor, pump, forklift, crane, stairs, natural gas, manual handling and general security as percentage distribution was shown in the Fig. 2. These categories were detailed and then the distribution of risk levels were analyzed. For ex: for electricity 14 hazards identified such as conducting electrical work by incompetent persons, not conducting electrical wiring and grounding control, not providing employees with training to work safely with electricity. For natural gas 2 hazard were identified such as, lack of emergency exit signs and directions and unsuitable emergency exits and doors. For manual handling the working area was not suitable for safe load transportation, the material being transported was not suitable for manual transportation, the maximum load limit per worker was exceeded, the employees did not have enough training, the articulation to take/drop the load, etc. 12 hazards were identified. For stairs, 11 hazards were identified such as not using ladders in accordance with the standards, not being able to reach the work area while on the ladder, using ladders in unsuitable weather conditions, not choosing ladders suitable for the electrical environment. General security was included some points about office, building and personnel.

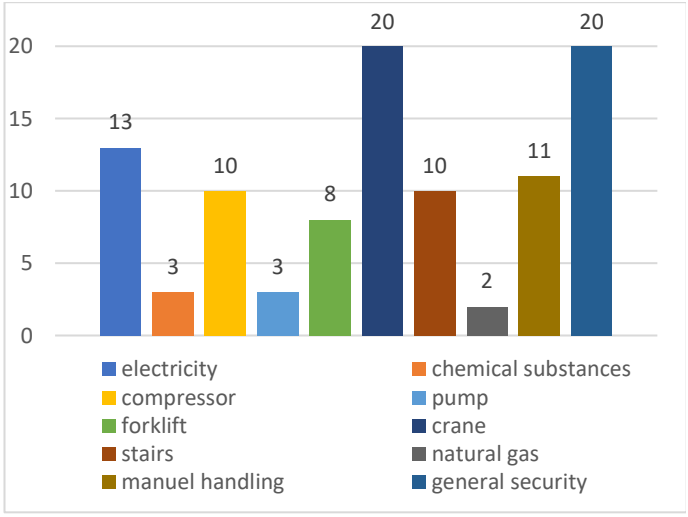

Figure 2. Distribution of hazards according to categories for WWTP

2.3. Analysis of Risks

Risk assessment is a process that includes the necessary studies to determine the dangers that exist in the workplace or that may come from outside, the factors that cause these hazards to turn into risks and the risks arising from the hazards by analyzing and rating them and determining the control measures (Falakh and Setiani 2018).

2.3.1. L Type(5x5 Matrix)

Risk matrices are a method of combining qualitative or semi-quantitative outcome/probability ratings for determining risk level or risk rating. 5x5 matrix is especially used to evaluate cause and effect relationships. The risk score is calculated on the basis of probability and severity parameters. The work should not be started until the identified risk is reduced to an acceptable level and should be stopped immediately if there is an ongoing activity. In the L matrix method, the probability and severity parameters are evaluated on a scale of 1 to 5 and the risk score is calculated by multiplying them by Eq.1 (Ak, 2020).

RPN = Severity x Probability (1)

RPN is a number indicating the level of criticality. RPN in the calculation of the value, verbal or defined as probability a certain number of risks factors. The values assigned in the range are retrieved. For each type of error with RPN risks are identified starting from the owner of RPN minimizing in the short term, in the long run removal, corrective to be taken for measures are determined (Kursun et al. 2016). Probability verses severity 5x5 matrix was given at Fig. 3.

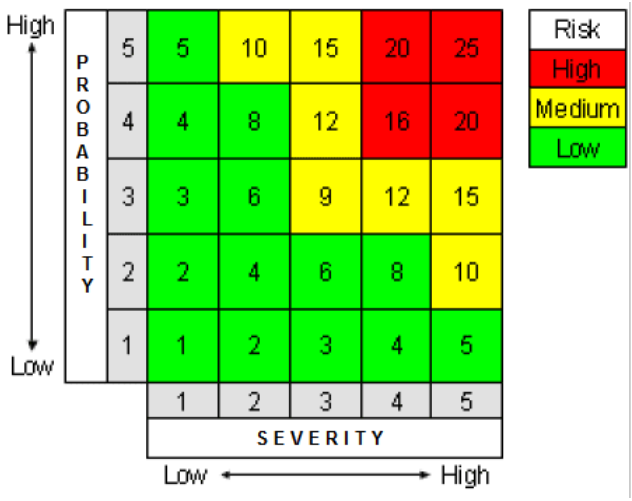

Figure 3. Probability verses severity 5x5 risk matrix

Limitations of risk matrix is that the data used in the risk matrix have different degrees of uncertainty. Some of the values are known with precision, others are wild guess. Generally, matrix use three colours (e.g., red, yellow and green) for representing the level of risk. Also, individual people have different risk tolerances. This can further distort how matrix can be used. People with low risk tolerance will over rate risks, while the people with

high risk tolerance will under rate risks. Fuzzy logic is a set of mathematical principles for knowledge representation based on degrees of membership. It deals with degrees of membership and degrees of truth. It reflects how people think and attempts to model our sense of words, our decision making and our common sense (Kumar and Shrihari, 2016).

2.3.2. Fuzzy Risk Analysis Methodology

The first step in preventing accidents is to make a suitable and adequate risk assessment. Risk assessment should be made taking into account all the dangers and risks of the employees, other people (visitors, anyone in the environment) (Abuzerr et al. 2020). In the analysis of risks; after the hazards are identified, the risk value is calculated by taking into account the probability value of the accidents and the effects of severity after they occur (Stamatis, 1995).

Probability: The occurrence of a hazard is based on likelihood. This possibility should be evaluated together with the conditions and factors that constitute this hazard. Rating steps for probability can be seen from Table 1.

Table 1. Rating steps for probability

	Meaning	Value
Expected	Will occur	5
Likely	Most likely	4
Often	Possibilities are happening or can occur	3
Unlikely	It is less likely to occur	2
Rare	Can be ignored	1

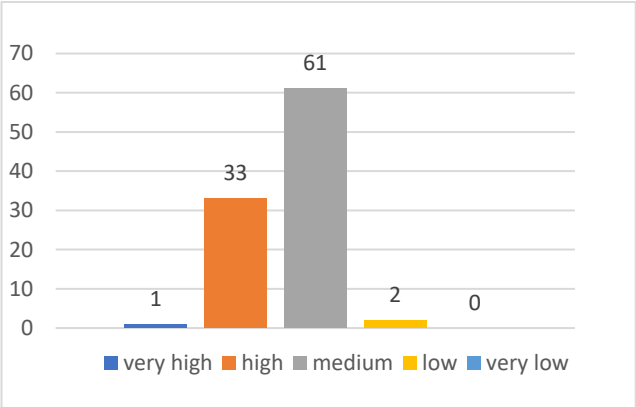

Figure 4. Distribution of accident probability values

Distribution of accident probability values was given at Fig. 4 for WWTP. From a total of 97 risks; one of them is shown as "Very High" with 5 likelihood values, 33 as "High" with 4 probability values, 61 as "Medium" with 3 li probability values, and 2 as "Low" with 2 probability values.

Severity: In case of occurrence of danger, it indicates the degree of damage to people exposed to danger and the environment. This weight is determined on the basis of experts' opinions, relevant scientific data, and published experiences. Rating Steps for severity is given Table 2.

Table 2. Rating steps for severity (Subriadi and Najwa 2020)

	Meaning	Value
Fatal	Meaningful inconvenience or anxiety	5
Major	Major injury	4
Moderate	Requiring inpatient treatment, but requiring clinical treatment accident without permanent marks	3
Minor	Minor injury	2
Insignificant	No impact	1

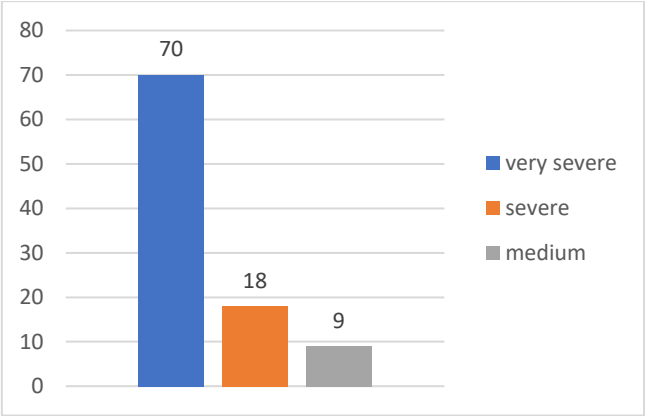

Figure 5. Distribution of severity values

Distribution of severity values was given at Fig. 5 for WWTP. From a total of 97 risks; 70 of them have a "very severe" level with 5 severity values, 18 of them have a "severe" level with 4 severity values, and 9 of them have a "medium" level with 3 severity values.

As it can be seen in Fig. 6, a suggested fuzzy model consists of different steps.

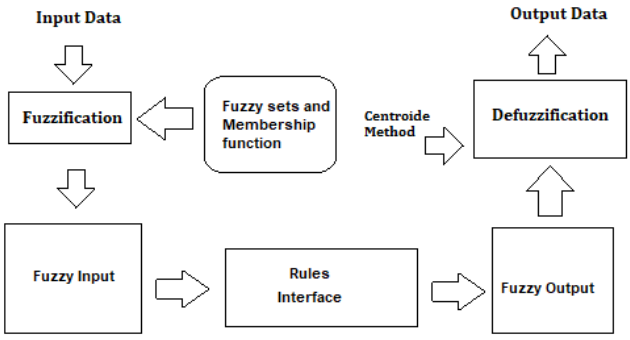

Figure 6. Representation of the fuzzy methodology (Radionovs and Rebrov, 2014).

1) Fuzzyfication, was a defining moment of membership functions and fuzzy sets of severity, probability and fuzzy RPN (FRPN).
2) Evaluation of fuzzy rule, using IF-THEN rule where IF was a variable of fuzzy input while THEN
was a variable of fuzzy output. All combinations must be grouped to produce fuzzy rules.

3) Defuzzyfication, with input defuzzyfication that was the fuzzy set obtained from the composition of fuzzy rules, while the output was the number in the fuzzy set. The technique used in this study was the Centre of Gravity (Centroid) (Suryoputro et al. 2019).

All these steps are carried out using the fuzzy toolbox that is present in Matlab (Shang and Hossen, 2013).

3. RESULTS and DISCUSSION

3.1. Analysis of Risk Assessment with Fuzzy Logic Method

Fuzzy Inference is the process of getting the equivalent of the input data in the rule base. Fuzzy inference system window "FIS Editor" was used in MATLAB for this process in the study. Fuzzy is designed in order to acquire the highest FRPN value which will be used as the focus of enhancements to reduce the probability of occurrence of some kind of failure for a second time (Balaraju et al, 2020). A model that was built in the techniques of fuzzy has 2 inputs (severity and occurence) and 1 output FRPN.

In this analysis, rule bases were created from the input data with Mamdani and the values in the risk analysis were calculated one by one. In practice, the input data probability and severity values, were blurred and membership functions were created for the probability, severity and FRPN. Triangular membership functions are defined for grading levels of very low, low, medium, high and very high.

In the triangle membership function for probability values; very low [0 1 2], low [1 2 3], medium [2 3 4], high [3 4 5] and very high probability value parameters [4 5 5] were assigned. MATLAB software blurring operation window of the probability value input data was shown at Fig. 7.

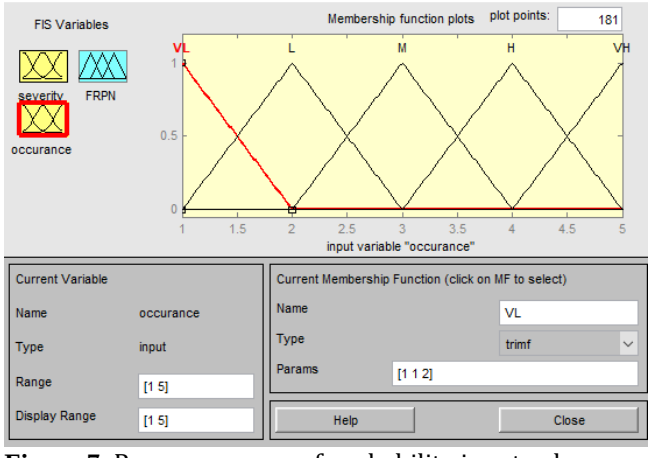

Figure 7. Program screen of probability input values

The severity values are in the triangle membership function; for negligible severity value [0 1 2], for mild severity value [1 2 3], for medium severity value [2 3 4], for high severity value [3 4 5] and very high severity value parameters [4 5 5] are assigned for. In Fig. 8, the blurring operation writing window of the MATLAB software program severity value input data was shown.

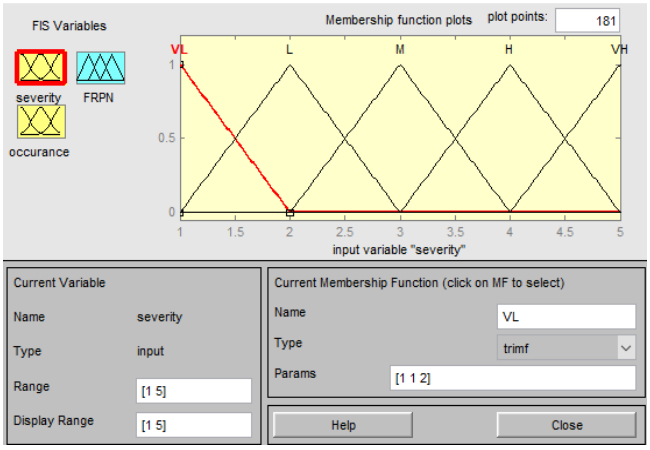

Figure 8. Program screen of severity input values

The assignment of FRPN is as follows: [0,1,2] range is very low, [1,2,3] range is low, [2,3,4] is medium, [3,4,5] is high, [4,5] is very high on the basis of definitions. After defining the parameters of the input values of probability, severity and risk priority number, in the triangle membership function and the verbal variables corresponding to these parameters, the possible situations were evaluated and 125 rules have been defined, program output was given at Fig. 9.

Firstly, the input values, which are severity and probability, are blurred using fuzzy expressions, membership degrees in the range of [0,1] are given to variables. Then, using operations, rule bases are determined. While creating rule bases and/or its connectors, the operator "and" is implemented (Fig.10).

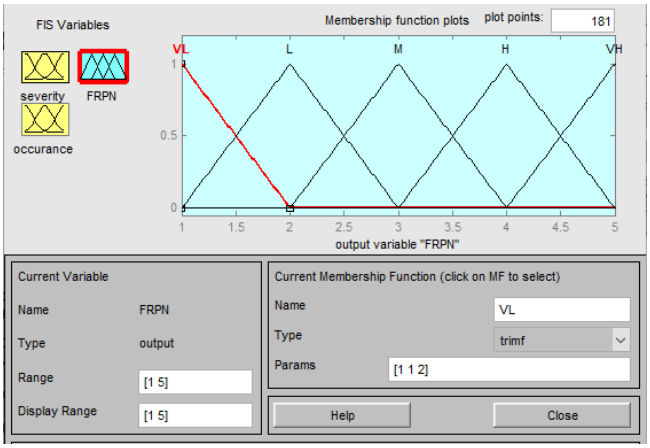

Figure 9. Program screen of FRPN Values

Estimated output with different input variables values can be observed from Fig. 12 for compressor. When maintenance and controls are disrupted and probability 4, severity 5; FRPN number was 4.68.

The thee-dimensional risk matrix formed as a result of the obtained results was given in Fig. 13. When the Fig. 13 was examined if If 1 <FRPN ≤ 2, the risk is medium. If 2 <FRPN ≤ 3, the risk is moderately high and necessary measures should be taken immediately and the risk should be tried to be reduced. If 3 <FRPN ≤ 4, it is high. The risk in this area is unacceptable. Low, medium, medium high and high levels are expressed in dark blue, blue, green and yellow colors, respectively. However, in accordance with fuzzy logic theory, transitions to different levels of risk are not sudden and using exact

color separations; It was made in a way to show the blur by opening the color tones.

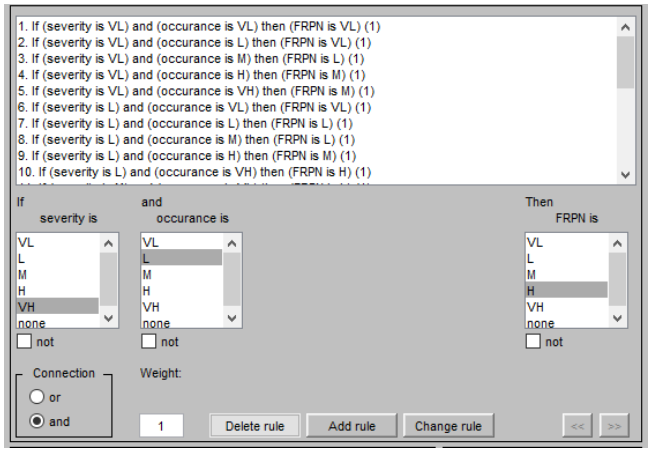

Figure 10. Fuzzy rule base window

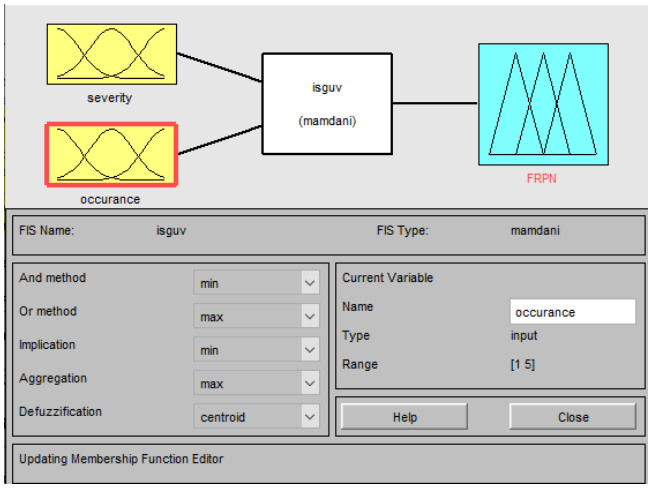

Figure 11. Program screen of FRPN Values by Mamdani fuzzy inference system

Figure 12. Inputs and output views of risk priority in matlab for compressor

The RPN values obtained is shown at Table 3. Although the risks have the same probability and severity values, different results are obtained when 5x5 matrix and fuzzy calculations are carried out in the determination of the risk magnitudes. When 5x5 matrix RPN results are evaluated, it is observed that the RPN values vary between 9 and 20 and for electricity RPN is 20, according to Figure 3 it is in high-risk category. FRPN is 4.68 and it has high risk category too. For pump, forklift and crane according to 5x5 matrix method they are in medium risk category but according to FRPN they are in high-risk category. Construction machines such as pumps, forklifts, cranes have an important share in the scope of occupational safety due to the accidents they can cause, and regular maintenance is very important for them in terms of both working and preventing accidents.

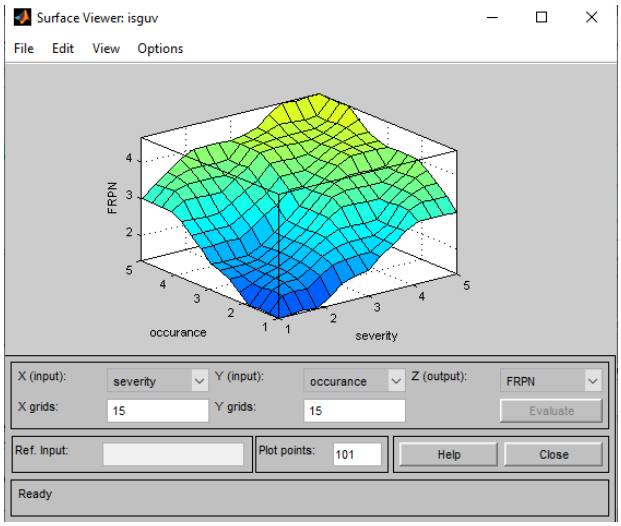

Figure 13. Result surface

Table 3. RPN values

Risk	FRPN	RPN
Electricity	4,68	20
Chemical Substances	4	15
Compressor	4,68	20
Pump	4	15
Forklift	4	15
Crane	4	15
Stairs	4	15
Natural Gas	4	10
Manuel Handling	3	9
General Security	4	12

When severity values are plotted against probability in risk structuring (Fig. 14), it is seen that most risks are at the boundary of categories. This creates lot of uncertainties in the overall risk assessment process. Risk matrix can be modified to avoid this problem. RPN calculation is only done by multiplying the severity and occurrence alone and irrespective of the degree of importance of each input. This method is based on human thinking and feeling, the project faces a vague imprecise concept and a quantitative value cannot be assigned to triple parameters; therefore, fuzzy theory is used as a valuable tool for calculations in uncertainty mode. Fuzzy logic was with the risks the measures needed to eliminate the risks are also blurred. Danger factor weights of the sources were taken into account.

In literature there is limited risk management study for WWTPs. Güner 2018, used 5x5 matrix method, Shinta et al. 2019, Asgarian et al. 2017, used traditional FMEA (Failure Mode and Effect Analiysis) method. In this study

fuzzy 5x5 matrix type risk assessment method is used which is never used for wastewater treatment risk management studies before. Fuzzy provides more accurate and better results than traditional methods.

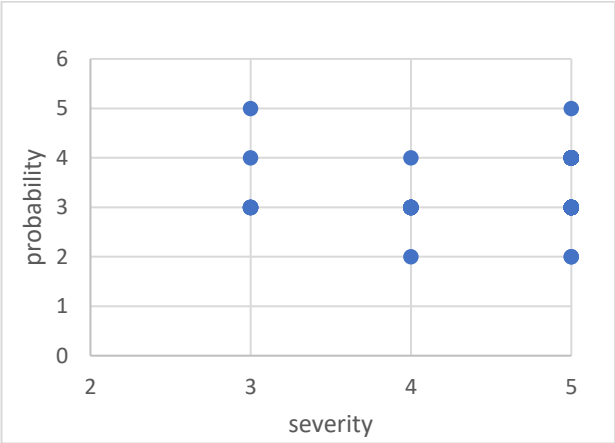

Figure 14. Risk matrix with different risks categories

4. CONCLUSION

The objective of this study is to develop a fuzzy logic system capable of analyzing and evaluating risks in WWTP. WWTPs are extremely important for general public health also necessary measures must be taken for safety and healty work conditions in WWTPs for employees and environment. This study is important because of the limited number of literature studies available. A fuzzy approach using linguistic variables has been proposed to eliminate the difficulties encountered in calculating a precise risk score and determining the measures to be taken, and to reduce the differences in expert opinion and combine them into a common denominator. RPN values investigated through Fuzzy logic and 5x5 matrix. RPN defines how the risk will affect the project objectives. The input data may also uncertainties and guesses. A false rating of a risk may have serious impact on the project. Hence the risk impact must be calculated by using mathematical models. The fuzzy logic is such a mathematical tool which can handle the uncertain data and provides solution reasonable manner which is similar to human thinking. Fuzzy logic brings a point of view where the boundaries are stretched by removing the exact boundaries. With this flexibility, the user can use the risk matrix more easily without any confusion.

An improved approach could be applied in future studies, such as artificial intelligence methods; fuzzy integrals, new fuzzy algorithms, genetic algorithm, artificial neural network. Especially, artificial neural network can help us in the field of risk management. When we have the correct data and we tuned the artificial neural network very well, the results of calculation can help us in the decision-making process.

ACKNOWLEDGEMENT

The author would like to thank Ankara Chamber of Industry 2nd and 3nd Organized Industrial Zone (OIZ) Regional Directorate WWTP, Environmental Management and Treatment Manager Enise Dilek ESEN and Occupational Health and Safety Specialist Meltem ATAGÜN for the provided data.

Conflicts of interest

The author declares no conflicts of interest.

REFERENCES

Abuzerr S, Hadi M, Zinszer K, Nasseri S, Yunesian M, Mahvi AH, Nabizadeh R, Hussien Mohammed S (2020). Comprehensive risk assessment of health-related hazardous events in the drinking water supply system from source to tap in Gaza Strip, Palestine. Journal of Environmental and Public Health, 1-10.

Ak M F (2020). Comparison of Risk Assessment Methods within the Scope of Occupational Safety in the Construction Sector. Avrupa Bilim ve Teknoloji Dergisi, (18), 272-282

Alavipoor F S, Ghorbaninia Z, Karimi S, Jafari H (2016). Surface water contamination risk assessment modeled by Fuzzy-WRASTIC. Water Environ. Res., 88, 589–601.

Asgarian M, Tabesh M, Roozbahani A, Bavani E B (2017) Risk Assessment and Management of Wastewater Collection and Treatment Systems Using FMADM Methods. Iran. J. Sci. Technol. Trans. Civ. Eng., 42, 55–71.

Balaraju J, Govinda Raj, M & Murthy C S N (2020). Prediction and Assessment of LHD Machine Breakdowns Using Failure Mode Effect Analysis (FMEA).

Bavani E B & Tabesh M (2012). Risk Assessment and Management of Wastewater Treatment Plants (WTPs) Using a Fuzzy Multi-Attribute Decision-Making (FMADM) Approach. 10th International Conference on Hydroinformatics.

Cabanillas J, Ginebreda A, Guillén D, Martínez E, Barceló D, Moragas L, Robusté J, Darbra R M (2012). Fuzzy logic based risk assessment of effluents from waste-water treatment plants. Science of the Total Environment, 439, 202–210.

Cossio C, Perez-Mercado L F, Norrman J, Dalahmeh S S Vinnerås B, Mercado A & McConville J (2019). Impact of treatment plant management on human health and ecological risks from wastewater irrigation indeveloping countries—Case studies from Cochabamba, Bolivia. International Journal of Environmental Health Research, 29, 1–19.

Edokpayi J, Odiyo J, Durowoju O (2017). Impact of wastewater on surface water quality in developcountries: A case study of South Africa. Environmental Science, 1.

El-Quliti S A, Basarwan R, Alzahrani H, Alzahrani S, Badr F (2016). Procedure for Hazard Identification and Risk Assessment in Wastewater Treatment Planting Saudi Arabia, International Journal of Scientific And Technical Research In Engineering (IJSTRE), 1, 1-10.

Emhan A (2009). Risk yönetim süreci ve risk yönetmekte kullanilan teknikler. Atatürk Üniversitesi İktisadi ve İdari Bilimler Dergisi, 23, 209-219.

Falakh F & Setiani O (2018). Hazard identification and risk assessment in water treatment plant considering environmental health and safety practice. E3S Web of Conferences.

Ghandi M & Roozbahani A (2020). Risk Management of Drinking Water Supply in Critical Conditions Using Fuzzy PROMETHEE V Technique. European Water Resources Association (EWRA), 34, 595-615.

Güner E D (2018). Environmental risk assessment for biological wastewater treatment plant. Pamukkale University Journal of Engineering Sciences, 24, 476-480.

Kudłak B, Wieczerzak M, Yotova G, Tsakovski S, Simeonov V & Namieśnik J (2016). Environmental risk assessment of Polish wastewater treatment plant activity. Chemosphere, 160, 181-188.

Kumar S S & Shrihari S (2016). Standardisation of Risk Assessment Process by Modifying The Risk Matrix, International Journal of Advance Research in Science and Engineering, 5(1), 148-158.

Kursun B, Kurt U, Guvercin S, Okten K, Akgul S & Yildiz A (2016). An application for the failure mode and effects analysis integrated with the grey relational analysis. Trakya University Journal of Engineering Sciences, 17, 35-44.

Łój-Pilch M & Zakrzewska A (2020). Analysis of risk assessment in a municipal wastewater treatment plant located in upper Silesia. Water, 100, 12-23.

Łój-Pilch M, Zakrzewska A & Zielewicz E (2018). Risk identification on the example of municipal sewage treatment plant. E3S Web of Conferences.

Malakahmad A, Downe A. G. Downe & Fadzil S D M (2012). Application of occupational health and safety management system at sewage treatment plants,IEEE Business, Engineering & Industrial Applications Colloquium (BEIAC), 2012, 347-350.

Mete T, Ozkan G & Ozkan G (2012). Control of dissolved oxygen concentration using neural network in a batch bioreactor. Computer Applications in Engineering Education, 20(4), 619–628.

Mirghafouri S H & Kousha A (2015). Risk Assessment of Water Transmission Pipelines with Fuzzy FMEA-AHP Approach (Case study: Yazd Water Transmission Pipeline). Journal of Applied Environmental and Biological Sciences, 5 (2015) 134-141.

Nicoleta U, Valentin V & Gheorghe V (2020). Water scarcity and wastewater reuse in crop irrigation. Sustainability, 12, 1-18.

Özkan G, Akin B A & Özkan G (2013). The prediction of chemical oxygen demand (COD) or suspended solid (SS) removal using statistical methods and the artifical neural network in the sugar industrial wastewaters. ARPN Journal of Engineering and Applied Sciences, 8(12), 978-983.

Özkan G, Uçan L & Özkan G (2010). The Prediction of SO2 Removal Using Statistical Methods and Artificial Neural Network. Neural Computing and Applications, 1-9.

Radionovs A & Rebrov O (2014). Application of fuzzy logic for risk assessment. Inf. Technol. Manage. Sci., 17(1):50–54.

Shang K & Zakir H (2013). Applying Fuzzy Logic to Risk Assessment and Decision-Making Sponsored by CAS/CIA/SOA Joint Risk Management Section.

Shinta F R, Karnaningroem N & Mardyanto A (2019). Risk Management of Wastewater Treatment in the Wastewater Treatment Plant of PT. X. The 1st International Conference on Business and Management of Technology (IConBMT), Institut Teknologi Sepuluh Nopember, Surabaya, Indonesia.

Stamatis D H (1995). Failure Mode and Effect Analysis: FMEA From Theory to Execution. ASQ, (Quality Press, Milwaukee), 1.

Subriadi A P & Najwa N F (2020). The consistency analysis of failure mode and effect analysis (FMEA) in information technology risk assessment. Heliyon 6.

Suryoputro M R, Khairizzahra L, Amarria D S & Nawang Wahyu W W (2019). Failure Mode and Effect Analysis (Fuzzy FMEA) Implementation for Forklift Risk Management in Manufacturing Company PT.XYZ IOP Conference Series: Materials Science and Engineering 528 (1).

Yel E & Yalpir S (2011). Prediction of primary treatment effluent parameters by Fuzzy Inference System (FIS) approach. Procedia Computer Science, 3, 659-665.

Yılmaz A (2015). Küresel ısınmanın dünya su rezervleri üzerindeki etkileri. Urban Academy Rewieved Journal of Urban Culture and Management, 8, 63-72.

Turkish Journal of Engineering
https://dergipark.org.tr/en/pub/tuje
e-ISSN 2587-1366

Slow-light effect in symmetry-reduced non-defect photonic crystals

Ibrahim Halil Giden*

ASELSAN Academy, Ankara, Turkey

Keywords
Integrated circuits
Photonic crystals
Slow light
Light-matter interaction
Mode-order conversion

ABSTRACT

In this study, a two-dimensional low-symmetric photonic crystal (PC) configuration with elliptical geometry is presented and its slow-light (SL) effect is investigated. Reducing the symmetry in the PC unit cell provides slow modes at the higher transverse electric bands. The calculated group index and the corresponding normalized bandwidth equal to {n_g, BW}={63.56, 0.0065}. That corresponds to a value of figure of merit (FOM)=0.4344 defined by the product of the average group index and the normalized bandwidth, FOM=$\langle n_g \rangle$BW, which is comparable to the values available in literature. Tracing the whole edges of the Brillouin zone, strongly excited SL modes are observed only along Γ-X but not along Γ-X' or Γ-M. That condition allows for the design of low-symmetric PC waveguides with finite thicknesses at the expense of lowering group index value. The SL effect is still obtained for the proposed low-symmetric PCs having finite thicknesses, which is numerically proved via finite-difference time-domain methods. It is important to note that non-dispersive SL Bloch modes exist through the non-zero *k*-vector components of Brillouin zone. Hence, such a defect-free (without either point- or line- defect) SL PC design may have a great potential for the use of compact photonic devices such as in optical switching and biochemical sensing applications.

1. INTRODUCTION AND DISPERSION RELATIONS OF PROPOSED ELLIPTIC PHOTONIC CRYSTALS

Photonic Crystals (PCs) are periodically modulated artificial materials that enable controlling the motion of light propagation as well as manipulating the photon velocity (Joannopoulos et al. 2008). Slowing down the flow of light enhances the light-matter interaction in a material. Photonic devices based on slow-light (SL) waveguides can be considered as key elements in optical communication systems to address bandwidth and switching power requests. Such devices also support enhanced nonlinearities, enabling the realization of compact low power all-optical switching devices (Khurgin & Tucker, 2018). Group velocity reduction is achieved near the band-gap edges and slow-light regimes exist at the flattened bands. However, slow modes near the band edges are observed to be highly dispersive and very lossy, which limits its use for efficient SL applications (Engelen et al. 2006). For that reason, different methods such as structural modifications of the photonics waveguide (Üstün & Kurt 2010; Üstün & Kurt 2012), variation of material type (Wu et al. 2013) or implementation of coupled waveguide systems (Mori and Baba, 2005) have been applied to engineer the dispersion curves of the defect modes. Nevertheless, such defect-based SL waveguides may expose to very high extrinsic losses (Krauss, 2007) due to the structural imperfections. Apart from these approaches, researchers have continued to perform studies that explore basic photonic crystal waveguide (PCW) structures. PCWs subject to various different modifications were studied to enhance slow wave performance of propagating light pulses (Moghaddam & Fleury, 2019; Hocini et al. 2018; Schulz et al. 2017; Han et al. 2015; Varmazyari et al. 2014; Khodamohammadi et al. 2015).

Slotted PCW configurations are suitable photonic structures to obtain slow light thanks to the availability for infiltration of slot region with low index material such as polymers and liquids/gases. As a result, slow light parameters can be externally tuned and such tuning capability could be implemented for efficient sensing applications (Kassa-Baghdouche & Cassan, 2018; Kassa-Baghdouche & Cassan, 2019; Zhao et al. 2014). Different optimization methods that target slow light studies considering group velocity dispersion, bandwidth,

* **Corresponding Author**
*(ihgiden@aselsan.com.tr) ORCID ID 0000-0002-3498-3151

Cite this article
Giden H I (2022). Slow-light effect in symmetry-reduced non-defect photonic crystals. Turkish Journal of Engineering, 6(4), 276-281

Research Article / DOI: 10.31127/tuje.985059
Received: 20/08/2021; Accepted: 06/12/2021

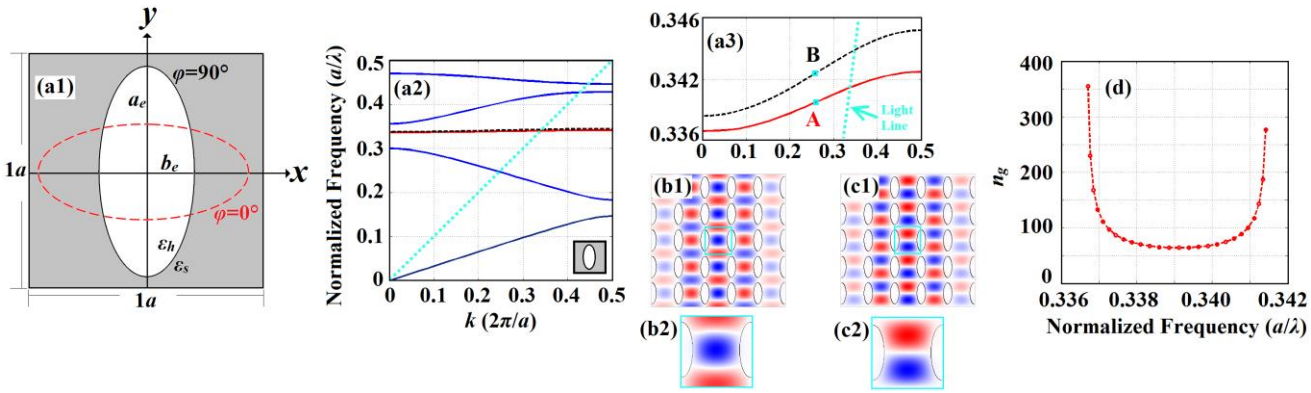

Figure 1. (a1) Schematic view of square lattice elliptic hole PC unit cell with its geometrical parameters. (a2) TE mode band structure of square-lattice elliptic PC holes with the dimensions of (a_e, b_e, φ)=(0.40a, 0.16a, 90°) and (a3) its close inspection at third TE band. The corresponding magnetic mode profiles of degenerate modes (b1) A and (c1) B, and their zoomed views at unit-cell scale: (b2) for the even mode, A, and (c2) for the odd mode, B. (d) The group index spectrum of the corresponding mode, A. Regarding mode profiles are calculated at the k-points signed with square markers in (a3).

normalized delay-bandwidth product and fabrication issues have been summarized in Zhao et al. (2015). It was indicated in Bagci & Akaoglu (2015) that performance of optical devices such as buffering and electro-optic modulation could be improved via slow light concept. An optimization algorithm was implemented in Mirjalili & Mirjalili (2014) and Mirjalili (2014) to obtain PCW with oval shaped holes and to enhance high normalized delay-bandwidth product parameter.

Symmetry reduction in PC unit cell, i.e., breaking the rotational symmetry of PCs, facilitates the realization of peculiar optical characteristics such as complete photonic band gaps (Giden & Kurt 2012), super collimation (Gumus et al. 2018) and graded refractive-index modulation (Giden et al. 2015). The present study deals with SL in a low-symmetric PC waveguide that does not include either line- or point defects, which is termed as "defect-free" in the rest of the study. A two-dimensional (2D) PC structure is considered, which is formed by square lattice elliptical holes and the PC unit-cell geometry is schematically shown in Fig. 1(a1). The holes are assumed to be hollow, ε_h=1 and the slab is made of Si-, ε_s= (3.45)^2. The rotation angle, the major and minor radii of vertically-oriented elliptic PC holes are set to be (a_e,b_e,φ)=(0.40a,0.16a,90°) so that the regarding eccentricity equals e=b_e/a_e=0.40. The lattice constant is fixed at 1.0a. It's well-known that reducing the symmetry of primitive PC cell influences the dispersion properties of the PC modes especially at high symmetry points (Trifonov et al. 2004; Giden et al. 2014). For that reason, two-fold (C2) rotationally symmetric PC unit cell with elliptical hole is chosen rather than regular one with circular hole in order to trigger the slow light effect.

Throughout the study, the polarization of light is transverse electric (TE), *i.e.,* the magnetic field is perpendicular to the plane of propagation. Dimensions of the PC waveguide are arranged based on the future applications such as SL and mode-order conversion. Band structure as well as group index calculations are carried out using plane wave expansion method (Johnson and Joannopoulos 2001). 2D finite-difference time-domain (FDTD) verifications are also performed (Oskooi et al. 2010). In all numerical calculations, only TE polarization is employed and the FDTD grid size is set to Δx=Δy=a/30. The computational domain is surrounded by perfectly-matched layers (PMLs) to remove undesired back reflections at the boundaries. Plane wave is incident to the designed medium for steady-state field calculations.

For information carrying optical pulse, the velocity of its envelope is measured as a group velocity, v_g. The term "slow light" (SL) implies the group velocity of the wave packet to be smaller than the speed of light in vacuum, c. Group index is, then, described by the following relation: $n_g = c \cdot \left(\frac{\partial \omega}{\partial k}\right)^{-1} = {}^{c}/_{v_g}$, where ω and k denote the radial frequency and wavevector, respectively. Figure 1(a2) represents the dispersion diagram of designed 2D square lattice PC unit cell with elliptic holes (given as an inset in the figure) for TE modes in Γ-X direction. Dashed lines in the figure imply the light-line. Degenerate modes occur at the third TE band, which is surrounded by a box in Fig. 1(a2), and close-up view of the degenerate modes is shown in Fig. 1(a3). The magnetic field distributions of degenerate modes A and B are represented in Figs. 1(b1) and 1(c1), respectively. Unlike SL Bloch modes existing at the high symmetry points of Brillouin zone as reported in Ferrier et al. (2008), SL modes of the proposed elliptic PCs occur through the non-zero k-vector components in even A mode. The close inspections of regarding magnetic field profiles (H_z) can be viewed from Fig. 1(b2) –for mode A- and Fig. 1(c2) – for mode B-. Note that the corresponding field distributions are calculated at a specific k-point signed with square markers in Fig. 1(a3). It can be inferred from the figures that the mode A is even whereas B is an odd mode so that they don't couple to each other. Furthermore, the existing SL modes partially lie under the light-line. Although some portion of the SL band is above the light line, the PC slab could be sandwiched between either photonic bandgap claddings or total-internal reflection layers to avoid out-of-plane losses within the slow-light regime (Bushel et al. 2017).

The group index spectrum of the interested mode, even mode A, is plotted in Fig. 1(d). The calculated minimum group index for the even mode A is n_g=63.56. In the case of 10% group index variation, a bandwidth

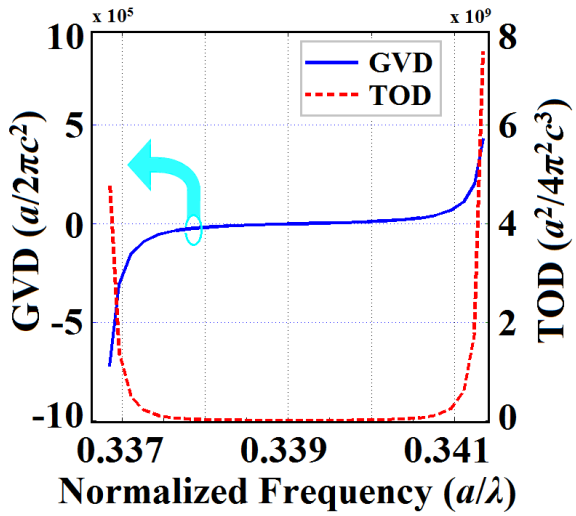

Figure 2. The calculated group velocity dispersion (GVD) and third-order dispersion (TOD) parameters for the even mode A as a function of operating frequencies.

that ranges from a/λ=0.3379 to a/λ=0.3401is obtained. Thus, the resultant normalized bandwidth (BW) becomes $BW = {}^{\Delta\omega}/_{\omega_c} = 0.0065$, where ω_c is the radial frequency centered at a specified bandwidth. To operate at telecom wavelengths, the lattice constant is set as a=525.45 nm so that the relative frequency bandwidth becomes BW = 1.26 THz (or 10 nm around 1550 nm wavelength). Another essential parameter to exploit SL effect is Figure of Merit (FOM), which is defined by the product of the average group index and the normalized bandwidth, $\text{FOM} = \langle n_g \rangle BW$. In this case, the relative FOM equals FOM=0.4334, which is reported to be FOM=0.554 in Üstün & Kurt (2012) and comparable to the delay-bandwidth product of FOM=0.48 reported in Elshahat et al. (2018). A recent study done by Ma et al. (2021) proposed a square lattice Si-based PCW configuration with extrinsic (InP) point-defects. The reported normalized delay bandwidth product in that paper is FOM=0.44, which is still close to the reported value in our study. All above calculated parameters imply that the even mode A has a non-dispersive SL effect with a moderate bandwidth and FOM.

Other critical parameters to be determined in SL systems are the group velocity dispersion (GVD) and third-order dispersion (TOD). GVD is defined as $\text{GVD}=\partial/\partial\omega(1/v_g)= \partial^2k/\partial\omega^2$, indicating the group velocity dependence of slow-light on operating frequencies. GVD should be as small as possible in SL applications to reduce optical pulse distortion (Khurgin, 2005). TOD is another important parameter for SL devices implying the deformation on the envelope of propagating signal. TOD is defined by the derivative of GVD with respect to the angular frequency and it should be at minimum to reduce higher order dispersion effects (Engelen et al. 2006). Figure 2 represents the corresponding GVD and TOD graphs for degenerate even mode A, in which SL effect exists. Around the operating SL frequency of a/λ=0.339, the proposed system has zero GVD and TOD = 1.072×10^7 ($a^2/4\pi^2c^3$).

TE mode photonic band structure of 2D elliptic PC holes having the dimensions of (a_e, b_e)=(0.40a, 0.16a) are traced along the edges of Brillouin zone, namely along X'-Γ-X-M-Γ path in order to observe the tendency of SL modes (see Fig. 3). The shaded regions along Γ-X' and Γ-M are inserted to determine the specified frequency interval where the SL effect is observed along Γ-X direction. It can be inferred from Fig. 3 that the degenerate modes of A and B along Γ-X tend to split towards other edges of Brillouin zone. Furthermore, available TE mode along Γ-X' is mode A whereas it is the odd mode along Γ-M in the SL frequency interval (shaded regions). Examining in detail the mode concerning mode profiles, an even mode cannot be excited along Γ-M direction since the existing mode in this SL interval is odd type. Considering the beam illumination along longitudinal Γ-X direction, coupling of orthogonal modes along Γ-X' could be achieved only by the existence of cavities/resonator systems in the proposed SL structure (Suh et al. 2004). In our case, even though an even mode (mode A) exists along Γ-X', it cannot be excited via beam incidence along longitudinal (Γ-X) direction since the PC structure does not include any disorders/defects. The calculated magnetic field profile along Γ-X' direction is given as an inset in Fig. 3. That situation brings to our mind that one can design a PC waveguide with finite thicknesses in order to obtain SL effect. That is because in the case of source incidence having even TE mode along Γ-X, no mode excitation occurs along Γ-M. That condition proves that strong SL excitation occurs only along longitudinal x- direction inside the defect-free PC waveguide with a finite thickness.

2. SLOW-LIGHT EFFECT OF DESIGNED PHOTONIC CRYSTAL WAVEGUIDE INVESTIGATED BY 2D TIME-DOMAIN ANALYSES

As mentioned previously, the PC waveguide having a finite thickness is formed by square lattice elliptical PC holes with the sizes of (a_e, b_e)=(0.40a, 0.16a) in order to support a fundamental even TE mode. 2D time-domain analyses are carried out to calculate the coupling efficiency as well as to observe SL effect of designed defect-free PC waveguide. As schematically demonstrated in Fig. 4(a), the length of slow wave structure is fixed as l=30a but its width, w_2, is adjusted based on desired applications such as mode-order conversion and SL effect. A TE-polarized Gaussian pulse

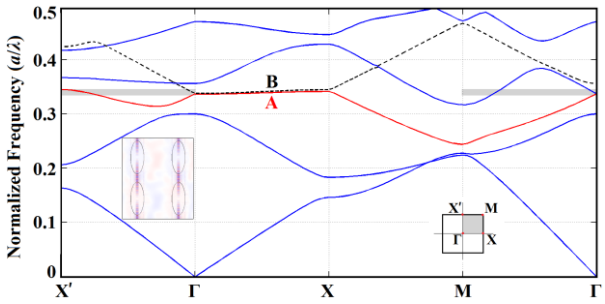

Figure 3. TE mode band structure of square-lattice elliptic PC holes with the dimensions of (a_e, b_e)=(0.40a, 0.16a) along the edges of Brillouin zone, which is given as an inset in the right part of the figure. Shaded regions indicate the frequency interval in which SL effect is observed through Γ- X direction.

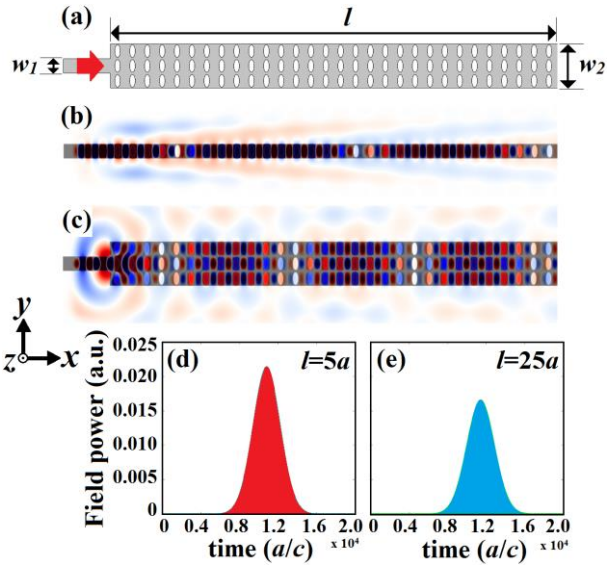

Figure 4. (a) Schematic view of 2D PC SL waveguide connected to an input dielectric waveguide with a width of w_1=1a. Regarding steady-state field distributions when the sizes of SL waveguide are set to (b) (l,w_2)=(30a,1a) and (c) (l,w_2)=(30a,3a) when incident frequency is a/λ=0.339. Time delay graphs of SL modes detected at distances (d) l=5a and (e) l=25a.

with a narrow bandwidth is injected from the input waveguide at a center frequency of a/λ=0.339, which has minimum GVD and TOD values. In this case, the slowed wave inside the SL structure becomes spatially localized, as can be noticed from Figs. 4(b) and 4(c). In these figures, only the input excitation port is shown and the waveguide is embedded into PMLs in order to suppress back reflections originating from the exit.

Remembering the magnetic field distribution of SL mode as in Fig. 1(b1), the SL mode, A, may also support higher order even modes. In this case, enlarging the width of SL waveguide enables a mode-order conversion of slowed light inside the system, as can be observed from Fig. 4(c). The coupling efficiency is calculated to be 41.4% for SL waveguide having a width of w_2=1a while this value decreases to 20.8% in the case of w_2=3a. Comparing both efficiencies, it is clear that due to mode mismatch between the incident wave and propagating SL as well as the width mismatch occurring in between the input and the PC waveguides causes the regarding insertion losses. We should note that the mentioned coupling efficiencies are calculated without any coupler or anti-reflection coating mechanisms. The corresponding group indices are determined by using delay information for slowly-propagating wave in the designed configuration. Optical pulses detected in time-domain at the positions of l=5a and l=25a are presented in Figs. 4(d) and 4(e), respectively. The FDTD simulation is terminated after monitoring the signal. Apparently from time delay graphs, the SL mode retains its shape and the propagating pulse is not exposed to temporal broadening, which is the sign of low GVD and TOD. Comparing both Figs. 4(d) and 4(e), field intensity reduction is observed while propagating through the designed low-symmetric PC waveguide due to the light leakages occurring along the vertical y- direction. Nevertheless, propagation losses due to light leakages along the vertical direction can be suppressed by surrounding the PC waveguide with photonic bandgap materials (Kurt et al. 2011). The corresponding group index is calculated from the relation $n_g = c(\Delta t/\Delta l)$ and it is found to be n_g=14.05.

The group index of the proposed elliptical PC waveguide is also determined via 3D FDTD analysis in order to provide actual device modeling. Regarding lattice constant is kept as a=520 nm in order to adjust the source incidence to operate at a wavelength of 1550 nm. In this case, the designed dielectric PC slab possesses a thickness at around 220 nm, which is a common value in SOI technology, and that SL waveguide having a width of w_2=520 nm is laid upon the Silica (SiO_2) substrate. The cladding is set to be air. The calculated group index from delay information via 3D time-domain analysis is obtained to be n_g=16.55, which matches well with the calculated value from 2D FDTD analysis. The reason of group index reduction compared to the value of n_g=63.56 calculated from the band structure can be the fact that since we need to choose a finite width of PC waveguide in order not to excite higher-order modes, there appear an index mismatch at air-PC waveguide interfaces. Since the propagating field inside SL waveguide also penetrates into air in the direction transverse to propagation, corresponding group index as well as the power of localized fields diminishes.

Precise fabrication of 2D PCs with elliptical geometry is another issue to tackle. Realization of elliptical PC holes could be achieved with good quality (with minimized structural disorders) via two-beam interference lithography (Quiñónez et al. 2006) as well as laser holography techniques (Hung et al. 2010).

3. CONCLUSION

In conclusion, a defect-free low symmetric PC waveguide that enables SL effect is proposed. Due to the C2 rotational symmetry in the primitive cell, degenerate slow modes exist at higher TE bands. The even slow wave mode and its group index spectrum are investigated in frequency domain and the desired SL effect is numerically proved by FDTD analyses. The corresponding group index and BW from the band structure are equal to n_g=63.56 and $BW = \Delta\omega/\omega_c$ = 0.0065, which in turn gives a satisfactory delay-bandwidth product value of FOM=0.4344 in 2D PC structure. The proposed SL configuration also possesses a tolerable coupling efficiency around 41.4% without the need of any coupling mechanisms. In the proposed PC configuration, the existence of non-dispersive SL Bloch modes is achieved through the non-zero k-components of Brillouin zone, *i.e.* away from the band-edges. Moreover, changing the widths of proposed elliptic PC structure supports to excite higher order TE modes. Such a defect-free SL structure can be implemented for compact optical switching, optical delay lines and sensing applications.

ACKNOWLEDGEMENT

The author thanks to Prof. Kurt for fruitful discussions and advices about the study.

Conflicts of interest

The author declares no conflicts of interest.

REFERENCES

Bagci F & Akaoglu B (2015). Enhancement of buffer capability in slow light photonic crystal waveguides with extended lattice constants. Optical and Quantum Electronics, 47(3), 791-806.

Elshahat S, Khan K, Yadav A, Bibbò L & Ouyang Z (2018). Slow-light transmission with high group index and large normalized delay bandwidth product through successive defect rods on intrinsic photonic crystal waveguide. Optics Communications, 418, 73-79.

Engelen R J P, Sugimoto Y, Watanabe Y, Korterik J P, Ikeda N, Van Hulst N F, ... & Kuipers L (2006). The effect of higher-order dispersion on slow light propagation in photonic crystal waveguides. Optics express, 14(4), 1658-1672.

Ferrier L, Rojo-Romeo P, Drouard E, Letartre X, & Viktorovitch P (2008). Slow Bloch mode confinement in 2D photonic crystals for surface operating devices. Optics express, 16(5), 3136-3145.

Giden I H & Kurt H (2012). Modified annular photonic crystals for enhanced band gap properties and iso-frequency contour engineering. Applied optics, 51(9), 1287-1296.

Giden I H, Turduev M & Kurt H (2014). Reduced symmetry and analogy to chirality in periodic dielectric media. Journal of the European Optical Society-Rapid publications, 9.

Giden I H, Rezaei B & Kurt H (2015). Method of implementing graded index media by symmetry-reduced helical photonic structures. JOSA B, 32(10), 2153-2157.

Gumus M, Giden I H & Kurt H (2018). Broadband self-collimation in C2 symmetric photonic crystals. Optics letters, 43(11), 2555-2558.

Han X, Wang T, Tang J, Liu B, Wang B, He Y, & Zhu Y (2015). Slow light with large group index–bandwidth product in ellipse-hole photonic crystal waveguides. Applied optics, 54(6), 1543-1547.

Hocini A, Maache M & Khedrouche D (2018). Wideband and low dispersion slow light by altering the geometry of a photonic crystal waveguide. Optics Communications, 427, 396-404.

Hung Y J, Lee S L, Pan Y T, Thibeault B J, & Coldren, L A (2010). Holographic realization of hexagonal two dimensional photonic crystal structures with elliptical geometry. Journal of Vacuum Science & Technology B, Nanotechnology and Microelectronics: Materials, Processing, Measurement, and Phenomena, 28(5), 1030-1038.

Joannopoulos J D, Johnson S G, Winn J N, & Meade R D (2008). Molding the flow of light. Princeton Univ. Press, Princeton, NJ. ISBN-10: 0691124566.

Johnson S G, & Joannopoulos J D (2001). Block-iterative frequency-domain methods for Maxwell's equations in a planewave basis. Optics express, 8(3), 173-190.

Kassa-Baghdouche L & Cassan E (2018). High efficiency slotted photonic crystal waveguides for the determination of gases using mid-infrared spectroscopy. Instrumentation Science & Technology, 46(5), 534-54.

Kassa-Baghdouche L & Cassan E (2019). Sensitivity analysis of ring-shaped slotted photonic crystal waveguides for mid-infrared refractive index sensing. Optical and Quantum Electronics, 51(10), 1-11.

Khodamohammadi A, Khoshsima H, Fallahi V & Sahrai M (2015). Wideband slab photonic crystal waveguides for slow light using differential optofluidic infiltration. Applied optics, 54(5), 1002-1009.

Khurgin J B (2005). Optical buffers based on slow light in electromagnetically induced transparent media and coupled resonator structures: comparative analysis. JOSA B, 22(5), 1062-1074.

Khurgin J B & Tucker R S (Eds.). (2018). Slow light: Science and applications. CRC press.

Krauss T F (2007). Slow light in photonic crystal waveguides. Journal of Physics D: Applied Physics, 40(9), 2666.

Kurt H, Giden, I H & Ustun, K (2011). Highly efficient and broadband light transmission in 90° nanophotonic wire waveguide bends. JOSA B, 28(3), 495-501.

Ma Y, Wu R & Li L (2021). Research on slow light transmission with wide bandwidth and large normalized delay bandwidth product. Optoelectronics Letters, 17(7), 407-411.

Mirjalili S M & Mirjalili S (2014). Oval-shaped-hole photonic crystal waveguide design by MoMIR framework. IEEE Photonics Technology Letters, 26(24), 2446-2449.

Mirjalili S M (2014). SoMIR framework for designing high-NDBP photonic crystal waveguides. Applied optics, 53(18), 3945-3953.

Moghaddam M K & Fleury R (2019). Slow light engineering in resonant photonic crystal line-defect waveguides. Optics express, 27(18), 26229-26238.

Mori D & Baba T (2005). Wideband and low dispersion slow light by chirped photonic crystal coupled waveguide. Optics express, 13(23), 9398-9408.

Oskooi A F, Roundy D, Ibanescu M, Bermel P, Joannopoulos J D & Johnson S G (2010). MEEP: A flexible free-software package for electromagnetic simulations by the FDTD method. Computer Physics Communications, 181(3), 687-702.

Quiñónez F, Menezes J W, Cescato L, Rodriguez-Esquerre V F, Hernandez-Figueroa H & Mansano R D (2006). Band gap of hexagonal 2D photonic crystals with elliptical holes recorded by interference lithography. Optics Express, 14(11), 4873-4879.

Schulz S A, Upham J, O'Faolain L & Boyd R W (2017). Photonic crystal slow light waveguides in a kagome lattice. Optics letters, 42(16), 3243-3246.

Suh W, Wang Z & Fan S (2004). Temporal coupled-mode theory and the presence of non-orthogonal modes in lossless multimode cavities. IEEE Journal of Quantum Electronics, 40(10), 1511-1518.

Üstün K & Kurt H (2010). Ultra-slow light achievement in photonic crystals by merging coupled cavities with waveguides. Optics express, 18(20), 21155-21161.

Üstün K & Kurt H (2012). Slow light structure with enhanced delay–bandwidth product. JOSA B, 29(9), 2403-2409.

Trifonov T, Marsal L F, Rodriguez A, Pallares J & Alcubilla R (2004). Effects of symmetry reduction in two-dimensional square and triangular lattices. Physical Review B, 69(23), 235112.

Varmazyari V, Habibiyan H & Ghafoorifard H (2014). Slow light in ellipse-hole photonic crystal line-defect waveguide with high normalized delay bandwidth product. JOSA B, 31(4), 771-779.

Wu H, Citrin D S, Jiang L Y & Li X Y (2013). Polarization-independent slow light in annular photonic crystals. Applied Physics Letters, 102(14), 141112.

Zhao Y, Zhang Y N & Wang Q (2014). Slow-light optimization of polymer-infiltrated slot photonic crystal waveguide. IEEE Transactions on Nanotechnology, 13(4), 687-694.

Zhao Y, Zhang Y N, Wang Q & Hu H (2015). Review on the optimization methods of slow light in photonic crystal waveguide. IEEE transactions on nanotechnology, 14(3), 407-426.

Turkish Journal of Engineering
https://dergipark.org.tr/en/pub/tuje
e-ISSN 2587-1366

Investigation of the impact of the implementation of the coastal aquifer management plan on nitrate pollution in Gaza Strip Aquifer using modeling techniques

Abdallah Jaroun [*1], **Ayşe Yeter Günal**[1]

[1]*Gaziantep University, Engineering Faculty, Civil Engineering Department, Gaziantep, Turkey*

Keywords
Coastal Aquifer
Gaza Strip
GMS MODFLOW
Groundwater Modeling
Nitrate Concentration

Abstract

Groundwater is the principal source of public water supply and for satisfying the daily water needs. The Gaza strip coastal aquifer is suffering from salinity and contamination due to human activities especially agriculture activities. Although, the nitrate is necessary for agriculture activities it can affect the groundwater quality if leached nitrate from the soil into freshwaters after some time. The main objective of this research is to evaluate the current situation of the Gaza strip coastal aquifer and to predict the nitrate concentrations resulting from agriculture activities over the next twenty years using modelling approach. 3D Numerical groundwater flow modeling was developed to simulate the impacts of transport of nitrate loading from agricultural land on groundwater system using finite difference method GMS 10.4 software (MODFLOW 2005 code and MT3DMS package). Five management scenarios were considered to study the effect of pumping and recharge parameters on the groundwater flow system and the impacts of transport of nitrate loading from agricultural areas on the aquifer. Ten different wells were selected to investigate the impact of management scenarios on the nitrate concentration. All management scenarios indicated that there is a relationship between the water level and nitrate concentration in aquifer therefore the rates of nitrate concentration in the southern regions of Gaza strip is more than the northern regions.

1. Introduction

Groundwater is the main source of freshwater that is essential for other human activities such as agriculture, industry, and domestic consumptions. Groundwater is contaminated when the concentration of contaminant exceeding the tolerable upper limit and limit its potential use. Agricultural land made up 157.50 km, equivalent to 43% of Gaza strip Area. Although, the nitrate is necessary for agriculture activities it can affect the groundwater quality if leached nitrate from the soil into freshwaters after some time. Therefore, high rates of nitrate concentration will be observed due to excessive use of N-fertilizers in agricultural activities. The issue of high nitrate levels in drinking water decreases the oxygen-carrying capacity of hemoglobin in human blood, which can threaten the health of human. Thus, the effective management of water resources is important to minimize the danger to human life.

Efforts were made by PWA for the development of plans like; CAMP and NWP plans to enhancement of water quality in Gaza strip despite the political and financial difficulties. A model is conceptual descriptions created towards representation for physicals system through mathematical equations.

Modeling of groundwater flow focuses primarily on determining of flow rate, groundwater heads and flow direction through aquifers. These determinations are indicating to as simulation. Moreover, the transport models have become an essential application to study groundwater quality issue. The movement of contaminants and chemical variation of pollutants in the groundwater can be simulated by solute transport models. Solute transport model requires the preparation of a groundwater flow model (Zheng and Bennett 1995) Solute transport models can be used to compute and predict the concentration of a dissolved chemical species in an aquifer at any time (Fryberg 1988).

* **Corresponding Author**

*(abdallah.jaroun@gmail.com) ORCID ID 0000-0001-9851-4293
(agunal@gantep.edu.tr) ORCID ID 0000-0002-4866-2914

Cite this article

Jaroun A & Günal A Y (2022). Investigation of the impact of the implementation of the coastal aquifer management plan on nitrate pollution in Gaza Strip Aquifer using modeling techniques. Turkish Journal of Engineering, 6(4), 282-292

Research Article / DOI: 10.31127/tuje.988034

Received: 28/08/2021; Accepted: 22/01/2022

2. METHOD

The research methodology was divided into three basic phases. The research objective and data collecting and analysis are the first phase of the model. The quantity and quality of data involved in the modelling of groundwater system plays a fundamental role in the accuracy of numerical model results. Therefore, data collection is considered as a critical step in preparation of the model. Collected data are processed by using Geographic Information Systems GIS and Excel spreadsheets. Initially, the research started by collecting the available updated and recorded data from several sources and by different personal interaction with local professionals. Data include (Digital Elevation Model (DEM) of Gaza Strip, Groundwater level from 2000 to 2018, Groundwater quality parameters measurements for 2014-2020, Pumping rate records for 3600 wells, Rainfall measurements and other relevant climate data from 1980 to 2019, Geological data for Gaza Coastal Aquifer, Drilling completion records of wells and topographic data for Gaza Strip.

The second phase of the model consists of code selection and designing the numerical model. A new version of MODFLOW, called MODFLOW-2005 was used for the realization of the 3D numerical flow model.

The model calibration is completed in last phase of the model. The main objective of calibration is to check the reliability of the model by adjusting independent variables (parameters and fluxes) until reaching results within sensible ranges that represent the actual situation. The approach followed in groundwater modeling of this paper is summarized in Fig 1.

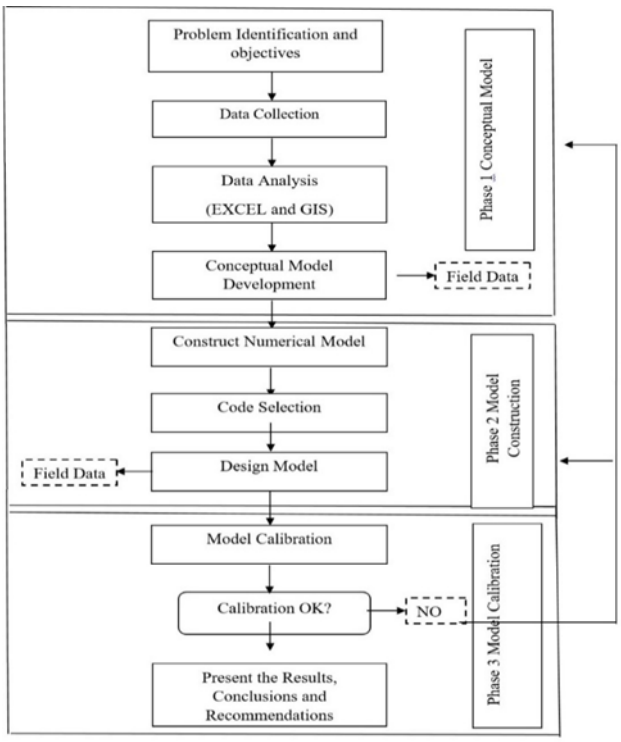

Figure 1. Flow chart illustrating the approach followed in groundwater modeling

3. STUDY AREA

Gaza strip situated on the Palestinian coast of the Mediterranean Sea with a length of 40 km, ranges from 6 to 12 km in width and has a total land area of 365 km^2. The region is bordered on the south by the Negev Desert and Egyptian Sinai Peninsula, the Mediterranean Sea to the west and occupied Palestine in 1948 to the east (Fig 2).

Gaza strip has an arid semi-humid due to its location in the transitional zone between desert of the Sinai Peninsula in Egypt and the Mediterranean Sea along the coast (Hallaq 2008). As result of Gaza strip location close to the sea, there is a gradual variation in Gaza Strip temperatures throughout the year, the mean monthly temperature ranges from about 17.6 C° in January to 29.4 C° in August.

The humidity rate in Gaza Strip is vary throughout the day in both season where the proportion of humidity in summer during the daytime is about 65% and 85% at night time while in winters the humidity rate is about 60% during the day and night times. The average annual potential evaporation is slightly elevated. The potential evaporation rate is estimated at about 1200 to 1400 mm/yr.

Figure 2. Location of Gaza strip (Abd Rabou 2019)

The average rainfall in the northern regions is different from southern regions, reaching 522 mm/yr in the northern areas and 225 mm/yr in the southern areas (Authority 2012). Gaza Strip has several types of soil that are loess, dark brown/silty clay, sandy, loessal sandy. The Gaza strip aquifer has a different width where the width ranging from 15 km northbound to around 20km southbound, while the groundwater depth ranging from 20 m in the southeast to 180 in the northwest (Fig 3).

The Gaza strip coastal aquifer composed of two different ages, the Pleistocene Kurkar and recent (Holocene age) sand dunes. The fundamental ingredient of Kurkar Group are Aeolian calcareous sandstone, marl, marine, reddish silty sandstone, clays, and conglomerates.

The Kurkar Group is dispersed in parallel to the coastline, from north to south of the Gaza Strip. It is stretch about 15-20 km inward and divide the aquifer into four-separated sub-aquifer, refer to as A, B1, B2, C, where it un-conformably topped with Eocene age chalks and limestone, or the Miocene-Pliocene age Saqiye Group, and clay stones.

Israeli studies proposes that the Kurkar Group becomes more clastic towards the east. The distinct 'layering' of sedimentary cycles becomes less clear, and the presence of red silty-clayey sandstone becoming more dominant. In addition, along the courses of main drainage, alluvial clays and soils become more obvious such as Wadi Gaza Clay layers were created as a result of the melting of glaciers and snow cover, which in turn lead to an increase in the sea level, this resulted in marine sediments led to formation of clay layers.

Clay formations are of two types: marine and fluvial. Marine clays are existed along the shore, at various depths within the formation. They pinch out about 5 km from present shoreline, and on the basis of existing data, appear to become more important towards the base of the Kurkar Group (Jamal and Yaqubi 2001).

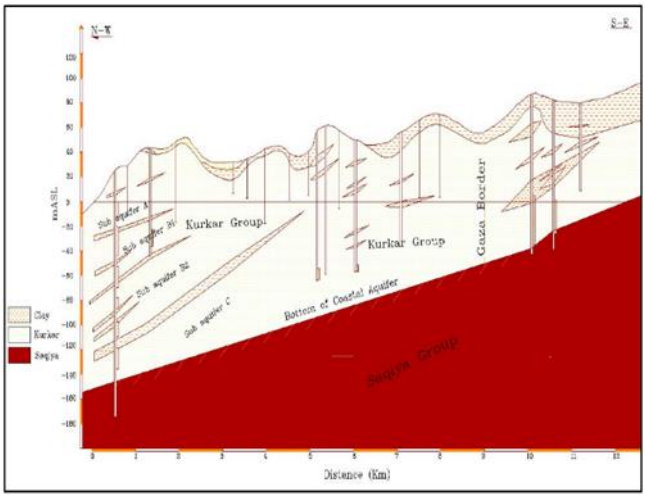

Figure 3. Geological cross section of Gaza strip coastal aquifer (Greitzer and Dan 1967)

4. DEVELOPMENT OF GROUNDWATER MODEL

4.1. Groundwater Flow Model

Conceptual groundwater flow model has been developed using three-dimensional finite difference method through GMS 10.4 software, MODFLOW 2005 code. Actually, after years of over pumping there are no significant changes in the hydraulic head, these would indicate that groundwater system reached to steady state. Consequently, year 2018 was stablished as steady state.

4.2. Model Building in GMS

The Gaza strip groundwater model is constructed based on a 200x200 m finite difference grid. The model domain covers an area of 365 km^2 and divided into 260 columns and 105 rows, vertically, the model thickness was divided into seven layers. Model cells that fall outside the study area and/or depth of interest have been inactivated. The Gaza strip groundwater flow model consisting of 191,100 cells (62,980 active cells and 128,120 inactive cells) (Fig 4).

4.3. Model Boundary Conditions

The Gaza strip groundwater flow model have been assigned boundary conditions as shown in Fig 4.

In Gaza strip groundwater model, the shoreline is represented as Specified Head boundary CHD with constant head zero m while the eastern border represents the borderline between Gaza strip and occupied territories, this border is represented as general head boundary GHB. Groundwater levels at the general head boundaries were estimated based on the average groundwater level measured by monitoring wells bores in proximity to the model boundary.

The GHBs were setup in the numerical groundwater model to represent amount of groundwater entering and leaving the model. The northern and southern border were assigned as a no flow boundary. In general, a no-flow boundary condition implies that the component of flux in the direction normal to the boundary is zero. The direction of groundwater flow is perpendicular to the shoreline, from east to west. That means the discharge across northern and southern boundaries equal zero.

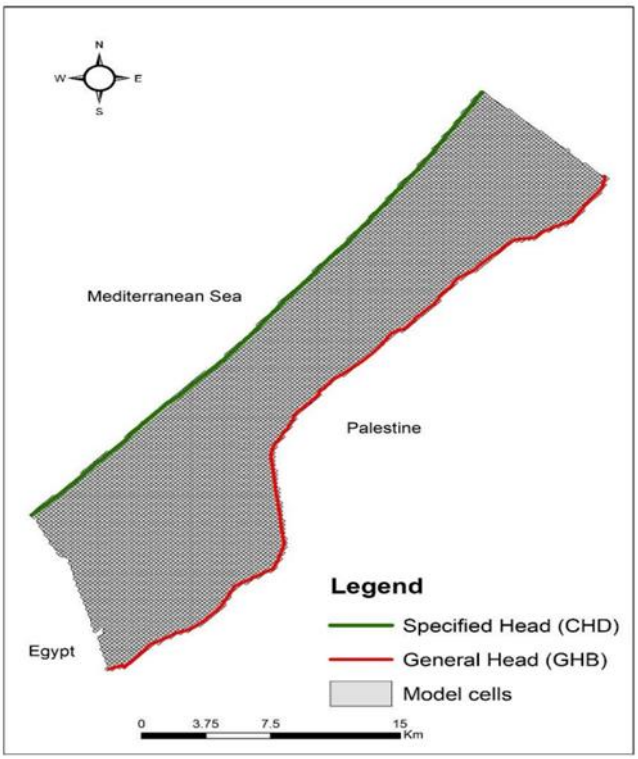

Figure 4. Boundary conditions and grid of Gaza strip Groundwater flow model

4.4. Freshwater Abstraction

Freshwater is extracted from the pumping wells thus information about abstraction rate of freshwater and well's location is required to the groundwater flow model. There are about 6000 wells in the Gaza strip classified into agriculture and municipal wells, about 72% of these wells are used for agriculture purpose, and about 1700 wells classified as and municipal wells. Allowed pumping rate to agriculture wells shall not exceed 50 m^3/d. pumping wells have been incorporated in the Gaza strip groundwater flow model using the MODFLOW 2005 'WELL1- Well' package and screen extent data.

4.5. Hydraulic Conductivity

The hydraulic conductivity is a basic parameters of groundwater flow model it plays a significant role in the measurement of hydraulic head.

The initial measurements of hydraulic conductivity have been obtained based on the previous researches and reports of pumping test carried out in Gaza strip. The horizontal hydraulic conductivity for aquifer ranging from 20 – 60 m/d with an average of 30 m/d and the aquitard the horizontal hydraulic conductivity is varied from 0.004 – 0.80 with an average of 0.2 m/d.

The vertical hydraulic conductivity was identified 8-10% of horizontal hydraulic conductivity. The other properties were set 0.3 for aquifer and 0.45 for aquitard and the specific storage rate was established 0.0001 m^{-1}.

The initial values of hydraulic properties used in the model development is shown in Table 1.

Table 1. Initial values of hydraulic properties used in the model development

Layer type	HK, VK (m/d)	Specific Storage (m^{-1})	Porosity
Aquifer (L1, L3, L5, L7)	HK: 30, VK: 3	10^{-4}	0.3
Aquitard (L2, L4, L6)	HK:0.2, VK: 0.02	10^{-4}	0.45

4.6. Recharge

The groundwater recharge for Gaza aquifer was estimated using coefficient values of recharge (Table 2) based on the type of soil (Fig 5) and the annual average rainfall for the past 10 years for each rain station. For representing the territorial distribution of regional average rainfall, Thiessen method was used. In Thiessen method, the rainfall is calculated as the nearest neighbor value (Viessman and Gary 2002; Wilson 1998). The concept of Thiessen method is that the area is subdivided into Thiessen polygons based on the rainfall station. The recharge polygons used in the model was obtained through the intersection between soil type map and the measurements of rain station in Gaza Strip for the rainfall for the past 10 years.

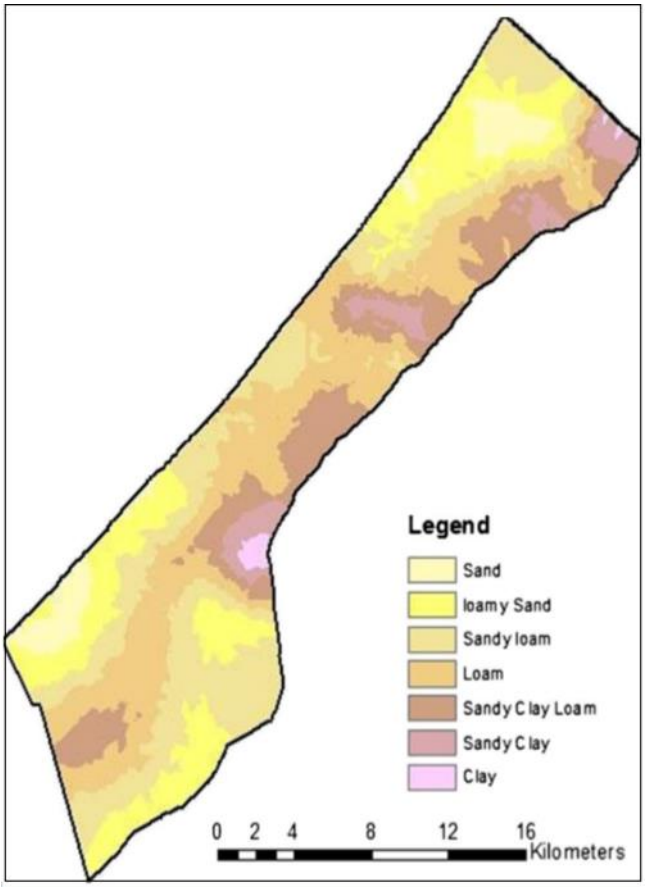

Figure 5. Soil map of Gaza strip (Abu Samra 2014)

Table 2. Recharge coefficient values (Semli, 2013)

Soil Types	RCH Ceof
Dark Brown/ Silty Clay	0.03
Sandy Regosols	0.7
Losses Soil	0.15
Lossal Sandy Soil	0.25
Sandy Lossal Soil	0.3
Sandy Lossal Soil over Loess	0.35

4.7. Groundwater Flow Model Calibration

The Gaza strip groundwater flow model was calibrated under steady state conditions using 41 observation wells (Fig 6). The initial values of hydraulic conductivity were obtained based on previous studies and the initial values of recharge package have been modified based on section 4.5. Three methods of calibration have been used to calibrate the model. The first method is manually calibrated. For this method, the parameters of steady state conditions have been modified manually. The manually calibrated model produced unreasonable results therefore, zone calibration with ranges (method 2) was used to optimize the initial parameter estimates. Actually, zone calibration produced unacceptable results. The manual and zone calibration have been followed by automated parameter estimation using PEST (method 3). The results of PEST produced high level of heterogeneity in aquifer layers. Consequently, pilot point technique has been used to mathematically enhance the initial parameter estimates of hydraulic properties. The scatter plot of the fit between computed and observed heads shown in Fig 7. The calibrated groundwater level for the first layer is

presented in Fig 8. The steady state calibration has shown statistics parameters for calibrated head, these parameters shown in Table 3. The results showed variations of horizontal hydraulic conductivity in the first and last layers, the values ranged between 35 m/d north and 23 m/d south of the Gaza strip.

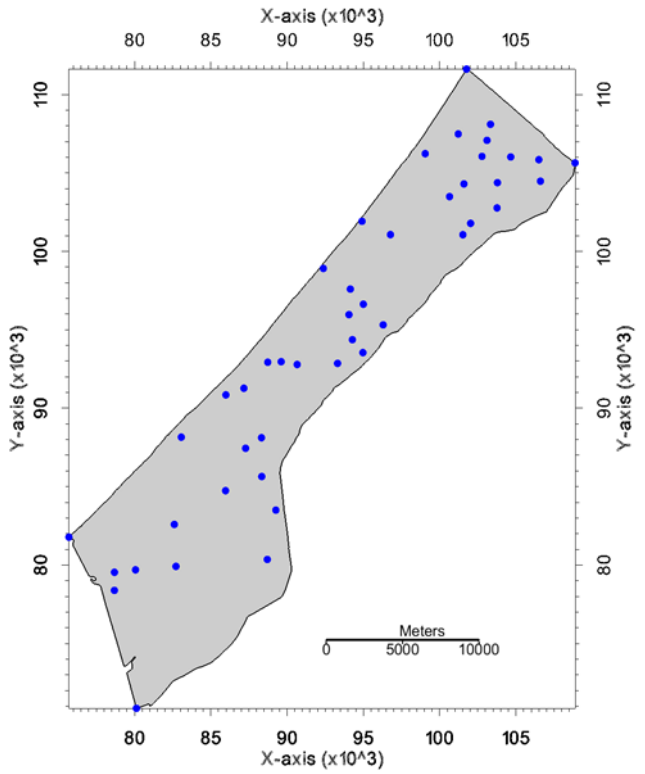

Figure 6. Observation wells used to calibrate the model

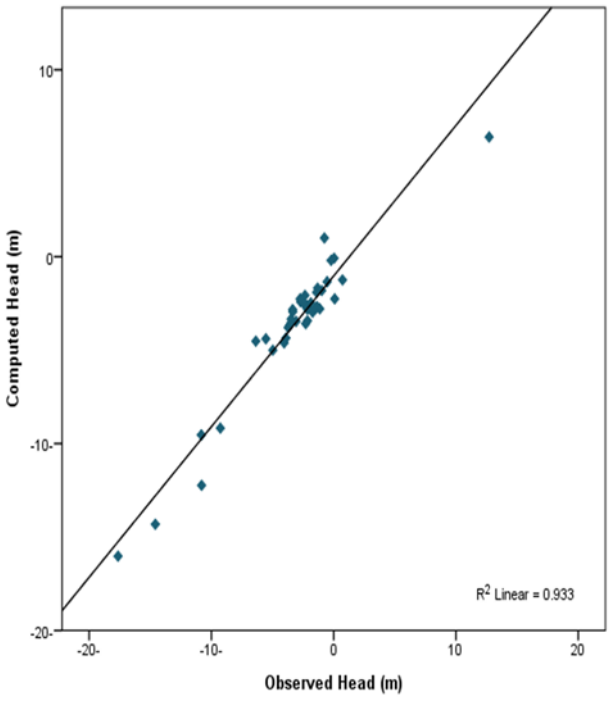

Figure 7. Scatter plot of computed and observed heads

Table 3. Statistical parameters of the model

Parameter	Value (m)
Mean Residual Head	0.40
Mean Absolute Residual Head	0.90
Root Mean Square Residual Head	1.39

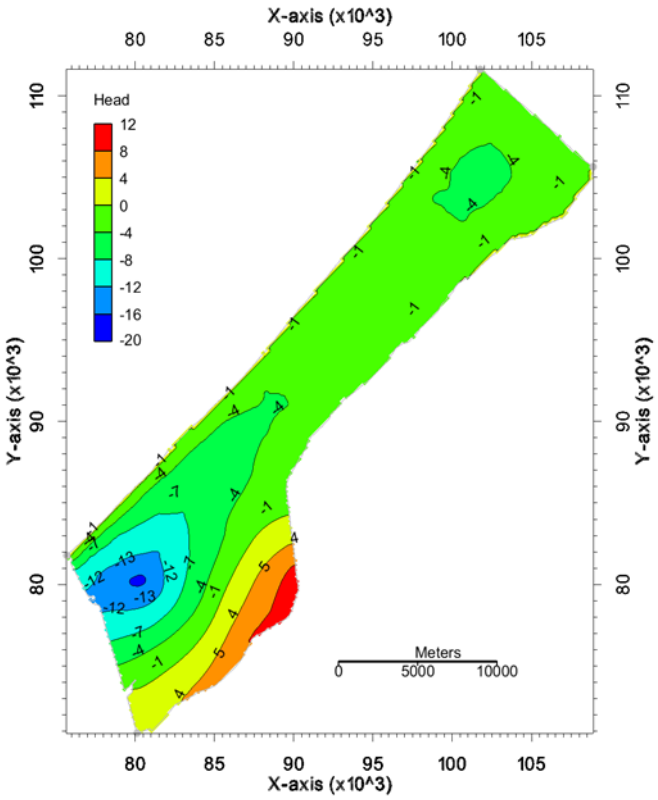

Figure 8. Calibrated groundwater head for year 2018

5. TRANSPORT MODEL

The Gaza strip groundwater flow model has been calibrated under steady state condition. The model has been converted to transient model (2019-2020) and developed based on the calibrated steady state results.

5.1. Initial Conditions

The initial head is a basic parameter used for solving the advection-dispersion equations of transport model. Initial conditions of the transport model indicate to the spatial distribution of starting concentration simulation. Using reasonable initial concentration conditions assist in a model convergence. The measurements of nitrate concentration of the year 2020 which obtained from laboratory readings according to PWA have been used as initial concentration.

5.2. Transient Transport Model Calibration

The calibration process requires improvement of model parameters. In transport model, the mass loading rates and soil properties parameters like longitudinal dispersivity are the most common parameters that impact on the output in MT3DMS. Those parameters were calibrated using trails and error process. The calibration value of longitudinal dispersivity was estimated 15 m and horizontal dispersivity was valued 1.5 m while vertical dispersivity equals 0.15 m. The computed and observed concentration are shown in Fig 9 and Fig 10 at the years 2019 and 2020 respectively. Simulated NO_3 concentration for the initial year 2020 shown in Fig 11.

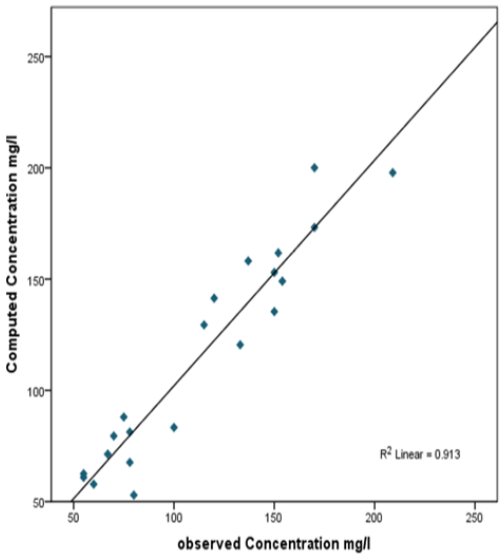

Figure 9. Scatter plot of computed and observed NO_3^- concentration in 2019

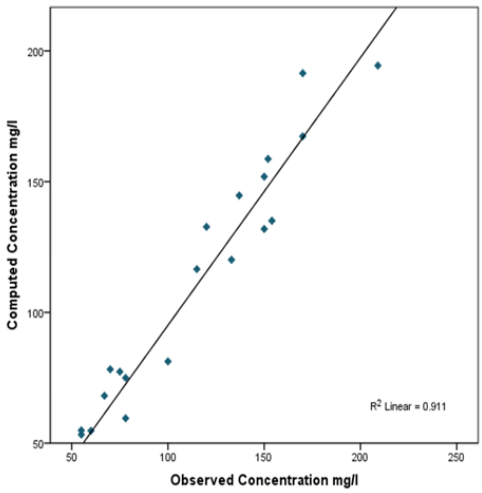

Figure 10. Scatter plot of computed and observed NO_3^- concentration in 2020

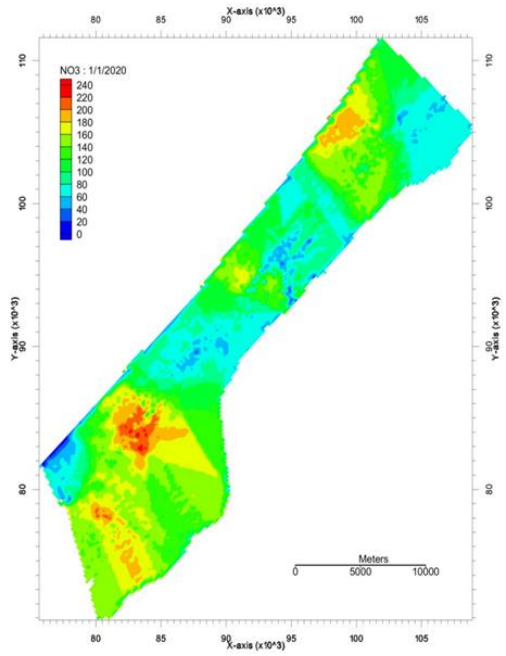

Figure 11. Simulated NO_3^- concentration for the year 2020

6. MODEL SCENARIOS MANAGEMENT

Calibration of groundwater flow model is a fundamental phase for prediction the nitrate concentration in the future. The calibration results were reasonable by numerical model used three-dimensional finite difference method by GMS MODFLOW for groundwater flow model and MT3DMS code for transport model.

The model management scenarios are important in order to find the best solutions to manage the abstraction and to creating the best available techniques to protect the groundwater from contamination.

Five management scenarios were considered to study the effect of pumping and recharge parameters on the groundwater flow system and the impacts of transport of nitrate loading from agricultural areas on the aquifer. These management scenarios developed based on plan adopted by Palestinian Water Authority for the management of water resources. Ten different wells were selected to investigate the impact of management scenarios on the nitrate concentration.

The scenarios properties can be described as the following points:

1. Current Situation (Sc.1).
   - Study the aquifer without any change neither in groundwater flow properties nor transport parameters over the simulation period.
2. Pumping management based on CAMP (Sc.2).
   - Production of the wells for after 2020 have been reduced on average 45-50% compared to 2015. Where the total production of Agricultural wells and municipal wells in 2015 were 95 and 86 MCM respectively.
3. Increasing the recharge (Sc.3).
   - Increasing the recharge rate using treated wastewater in the nitrate concentrations.
   - Injection wells have been used to add the treated wastewater in the depression regions.
   - The total treated wastewater used to increase the recharge rate increased gradually from 40 MCM in 2010 to 60 MCM in 2020. Over the simulation period the recharge rates was fixed at 60 MCM/year.
4. N-Fertilizers Management (Sc.4).
   - Reduction of the nitrogen used in fertilizers that loading in agricultural zones by 50% where the total amount of NO_3^- loaded in the model is 22,942.3 kg/d
5. Bringing all the previous scenarios together (Sc.5).

7. RESULTS AND DISCUSSIONS

In this study, two various purpose wells from each governorate with total ten wells were selected to investigate the impact of different management scenarios on the nitrate concentration over the next 20 years. The location of studied wells is presented in Fig 11.

Scenario 1

The first scenario simulates the work as usual without any change neither in groundwater flow properties nor

transport parameters over the simulation period from initial year 2020 to 2040. Simulation results show that there is an increase in NO_3^- concentration in the wells located in cultivate areas. The average nitrate concentrations after 20 years reached 551 mg/l.

Obviously, this high rate of concentration is due to the excessive pumping and indiscriminate use of N-fertilizers during agriculture activities and this is clear evidence of the deterioration in the groundwater quality.

Table 4 shows the initial and predictive of nitrate concentration according to the first scenario (Sc.1) for the studied wells.

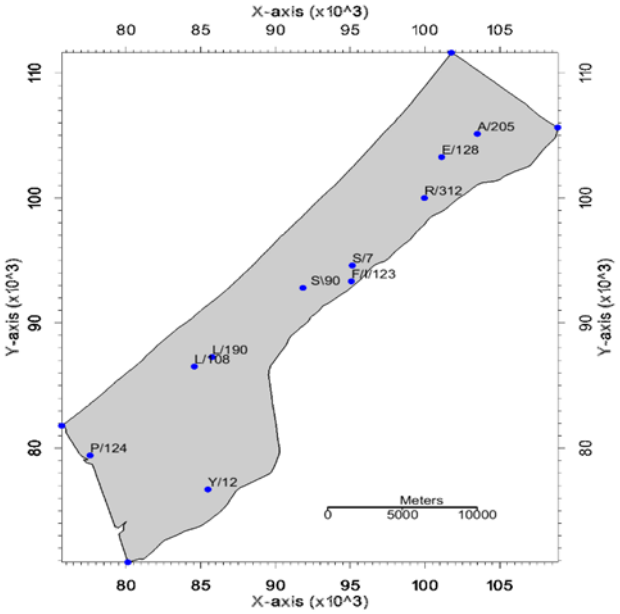

Figure 12. Spatial distribution map of studied wells

Table 4. Initial and predictive of nitrate concentration according to the first scenario (Sc.1)

Well ID	Governorate	Well Type	NO_3^- Concentration mg/l	
			2020	2040
A/205	North	Domestic	64.41	29.76
R/312	Gaza	Domestic	136.37	179.83
S/90	Middle	Domestic	53.48	31.95
L/190	Khanyounis	Domestic	105.83	250.08
P/124	Rafah	Domestic	50.47	41.41
E/128	North	Agriculture	150.45	80.46
S/7	Gaza	Agriculture	85.57	200.95
F/I/123	Middle	Agriculture	75.82	208.52
L/108	Khanyounis	Agriculture	168.73	551.87
Y/12	Rafah	Agriculture	150.57	350.24
Average			104.1	192.5

Scenario 2

The second scenario studied the nitrate concentration in the study area under the implementation of CAMP plane that aim to improve the groundwater level by decreasing the pumping rate from the aquifer by 50%.

Reduction of pumping rate is one of important options that can be used to improve the groundwater level and to manage the water resources in the future.

Simulation results indicated that the reduction of pumping rate would improve the water level slightly thus, the NO_3^- concentration decrease slightly where the average nitrate concentrations after 20 years decreased by 21.53 mg/l compared to current situation sc1.

Table 5 shows the nitrate concentrations for studied wells under the influence of the second scenario.

Table 5. Initial and predictive of nitrate concentration according to the Second scenario (Sc.2)

Well ID	Governorate	Well Type	NO3- Concentration mg/l	
			2020	2040
A/205	North	Domestic	64.41	38.01
R/312	Gaza	Domestic	136.37	150.60
S/90	Middle	Domestic	53.48	31.75
L/190	Khanyounis	Domestic	105.83	278.59
P/124	Rafah	Domestic	50.47	41.21
E/128	North	Agriculture	150.45	93.88
S/7	Gaza	Agriculture	85.57	194.67
F/I/123	Middle	Agriculture	75.82	178.79
L/108	Khanyounis	Agriculture	168.73	441.83
Y/12	Rafah	Agriculture	150.57	260.34
Average			104.1	170.97

Scenario 3

The third scenario proposed to simulate the impact of increasing the recharge rate using treated wastewater in the nitrate concentrations. Injection wells have been used to add the treated wastewater in the depression regions. Increasing the recharge is the best option to improve the groundwater level and to manage the groundwater in the future.

The simulation results indicated that the nitrate concentration has further improved over the next 20 years where the average nitrate concentrations after 20 years decreased by 47.72 mg/l compared to current situation sc1.

Table 6 shows the nitrate concentrations for studied wells under the increased the recharge.

Table 6. Initial and predictive of nitrate concentration according to the third scenario (Sc.3)

Well ID	Governorate	Well Type	NO_3^- Concentration mg/l	
			2020	2040
A/205	North	Domestic	64.41	20.84
R/312	Gaza	Domestic	136.37	120.66
S/90	Middle	Domestic	53.48	30.46
L/190	Khanyounis	Domestic	105.83	45.46
P/124	Rafah	Domestic	50.47	13.07
E/128	North	Agriculture	150.45	79.80
S/7	Gaza	Agriculture	85.57	192.33
F/I/123	Middle	Agriculture	75.82	192.33
L/108	Khanyounis	Agriculture	168.73	449.21
Y/12	Rafah	Agriculture	150.57	304.38
Average			104.1	144.78

Scenario 4

This scenario investigated the impact of reduction of the mass of N-fertilizers loading at cultivate areas by 50%. The cultivate areas used in the model is shown in Fig13. The total area of the cultivate zones in the study area is 48,490,959 m^2.

The simulation results show that the readings of nitrate concentration have significantly decreased, where the average nitrate concentrations after 20 years are estimated at 104.71 that means the average nitrate concentrations after 20 years decreased by 87.79 mg/l compared with work as usual scenario (sc.1).

Table 7 shows the nitrate concentrations for studied wells under N-Fertilizers Management (sc.4).

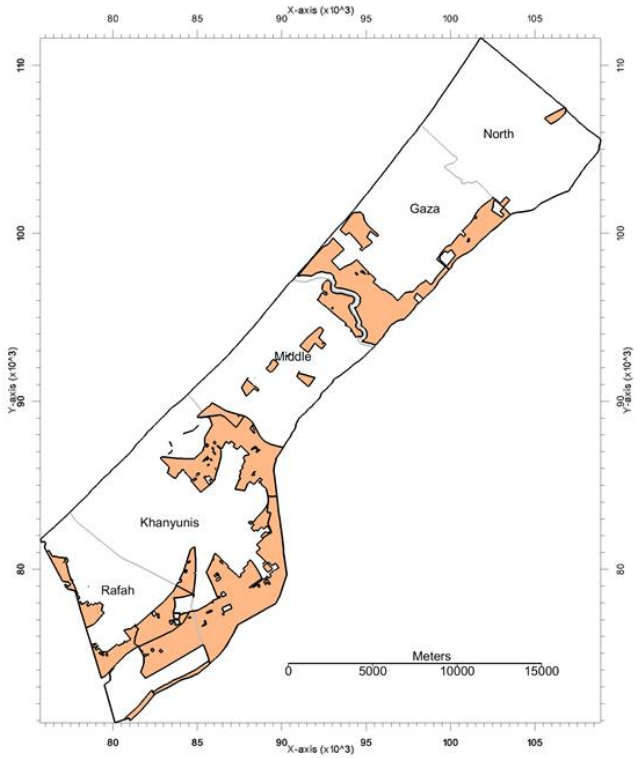

Figure 13. Agricultural areas of Gaza strip used in the model

Table 7. Initial and Predictive of Nitrate Concentration According to the Fourth Scenario (Sc.4)

Well ID	Governorate	Well Type	NO_3^- Concentration mg/l	
			2020	2040
A/205	North	Domestic	64.41	26.37
R/312	Gaza	Domestic	136.37	136.50
S/90	Middle	Domestic	53.48	31.51
L/190	Khanyounis	Domestic	105.83	144.59
P/124	Rafah	Domestic	50.47	35.79
E/128	North	Agriculture	150.45	80.64
S/7	Gaza	Agriculture	85.57	108.73
F/I/123	Middle	Agriculture	75.82	88.51
L/108	Khanyounis	Agriculture	168.73	252.48
Y/12	Rafah	Agriculture	150.57	142.31
Average			104.1	104.71

Scenario 5

This scenario studied the nitrate concentration in the study area when bringing all the previous scenario together. The simulation results show a significantly decreased in the nitrate concentrations. This means decreasing the abstraction from aquifer, increasing the recharge rate using treated wastewater and decreasing the mass loading of N-fertilizers by 50% are the main options that could be used to management the groundwater and protect the groundwater from nitrate contamination.

Table 8 shows the average nitrate concentration of the studied wells where the average concentration after 20 years is estimated at 58.17 mg/l.

Table 8. Initial and predictive of nitrate concentration according to the fifth scenario (Sc.5)

Well ID	Governorate	Well Type	NO_3^- Concentration mg/l	
			2020	2040
A/205	North	Domestic	64.41	2.70
R/312	Gaza	Domestic	136.37	44.21
S/90	Middle	Domestic	53.48	25.95
L/190	Khanyounis	Domestic	105.83	13.89
P/124	Rafah	Domestic	50.47	3.53
E/128	North	Agriculture	150.45	52.30
S/7	Gaza	Agriculture	85.57	77.37
F/I/123	Middle	Agriculture	75.82	73.79
L/108	Khanyounis	Agriculture	168.73	138.17
Y/12	Rafah	Agriculture	150.57	149.82
Average			104.1	58.17

Overall discussion

This section describes the General results for the five scenarios regrading to nitrate concentration by the end of simulation period (2040). Simulation of current situation has shown that there is a decline in the water level and deterioration in water quality. However, the highest nitrate concentrations are founded in the southern regions of the Gaza strip, where the concentration in khanyounis city reached to about 300 mg/l in the initail year 2020 while the concentration after 20 years reached nearly 550 mg/l in the same city. The concentration rates in the northern regions were below 200mg/l. This due to the low proportion of the agricultural area in the northern regions of the Gaza strip. However, the management scenarios showed improvements in the water level and improvements in the readings of NO_3^- concentration.

Two various purpose wells were selected from studied wells to study the impact of the implementation of CAMP plan on the nitrate concentration. These wells are L/108 for agricultural well and R/312 for domestic well. Fig 14 shows the optimal scenario for domestic well is increasing the aquifer recharge through treated wastewater using injection wells in the depression regions. While Fig 15 shows the best scenario for agricultural well is decreasing the mass loading of N-fertilizers this due to its location in the agricultural zones.

Overall, the current situation will increase the average nitrate concentration by 4.42 mg/l annually while management pumping scenario will decrease the annual rising in the concentration by 1.08 mg/l compared to work as usual scenario (sc.1). Increasing the recharge using injection wells in the depression regions and reduction of mass loading of N-fertilizers by 50% have also been implemented. The simulation results of Sc.3 and Sc.4 showed an increased in the average nitrate concentration by (2.03 and 0.03 mg/l) respectively.

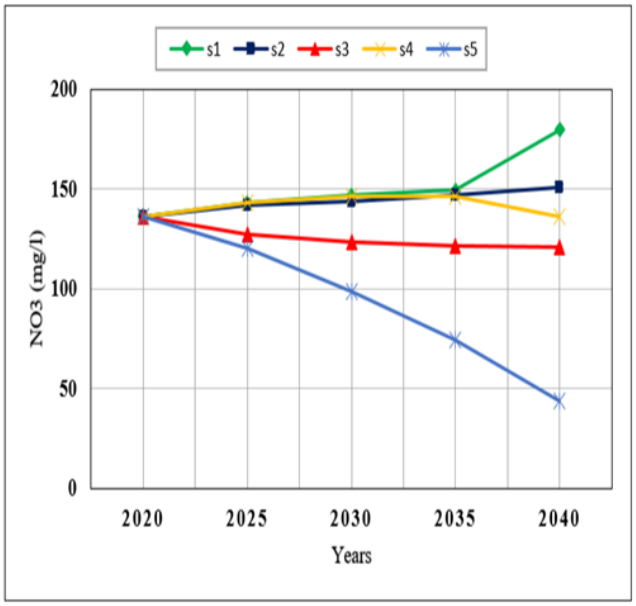

Figure 14. NO_3 concentrations for domestic well R/312 under implementation of CAMP plan

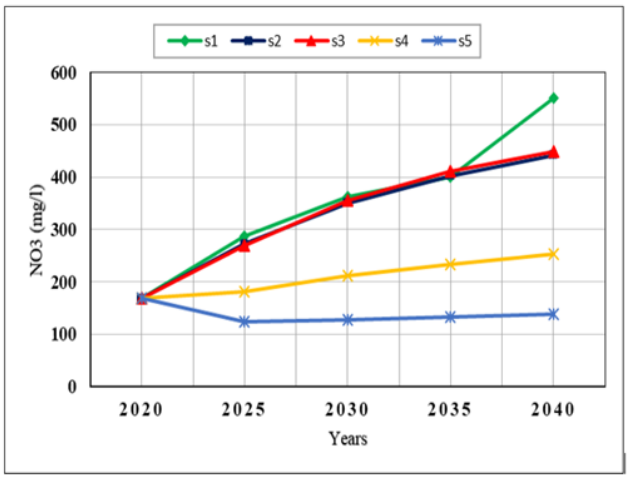

Figure 15. NO3 concentrations for agricultural well L/108 under implementation of CAMP plan

The simulation results also indicated that the average nitrate concentration will be decreased by 2.30 mg/l annually when implementing all scenario together (sc.5) as shown in Fig 16 and Table 9.

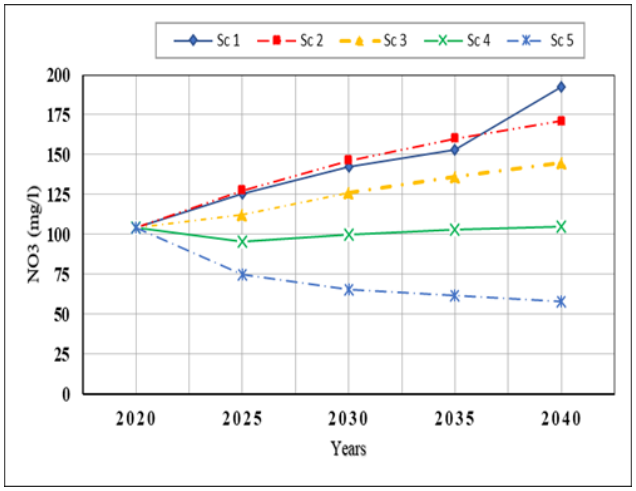

Figure 16. Average simulated Nitrate concentrations for all management scenarios

Table 9. Average simulated Nitrate concentrations for all management scenarios

No	Scenario	Initial Concrnt-ration (mg/l) 2020	Average Predicted Conc. After 20 Years (mg/l)	Average Annual Change (mg/l)
1	Current Situation	104.17	192.51	4.42
2	Decrease Abstraction	104.17	170.97	3.34
3	Increase Recharge	104.17	144.78	2.03
4	Reduction of Mass Loading of N- fertilizers	104.17	104.71	0.03
5	Bring all Scenario togother	104.17	58.17	-2.3

8. CONCLUSION

Development of the Gaza groundwater conceptual model was applied using the data on geology, soil, climate, land use, information about wells and abstraction actually; there was a lack of information such as recharge estimation of the aquifer and poor distribution of some data. However, the numerical groundwater flow model was developed to simulate the Gaza groundwater system and nitrate transport using a finite difference method through GMS 10.4 MODFLOW code and MT3DMS package.

Based on the water level over previous years indicates that the Gaza aquifer has reached to steady state. Consequently, year 2018 was established as a steady state. The model was calibrated using three methods are manual, zonal with ranges and pilot point technique.

The developed numerical model was applied to investigate the overall regional effect of pumping and recharge parameters on the groundwater system and the impacts of transport of nitrate loading from agricultural land on groundwater system for five future management scenarios. Therefore, transient transport model has been developed and the transport parameters (i.e., dispersivity) were calibrated.

Reduction of N-fertilizers loading at cultivate areas by 50% (scenario 4) showed improved in nitrate concentration where the annual change in the concentration was reduced to 0.03 compared to current situation Sc.1. Bringing all scenarios together (scenario 5) is the optimal scenario where the annual average change in nitrate concentration decreased by 2.30 mg/l after 20 years.

Generally, the nitrate concentration in the northern regions of the Gaza strip is lower than in the southern regions. Moreover, excessive pumping effects on the rates of nitrate concentration but the effects are not considerably as compared with reduction of N – fertilizers loading at cultivate areas. The NO3 concentration over the simulation period under the implementation of the CAMP plans are presented in Fig 17 – Fig 20.

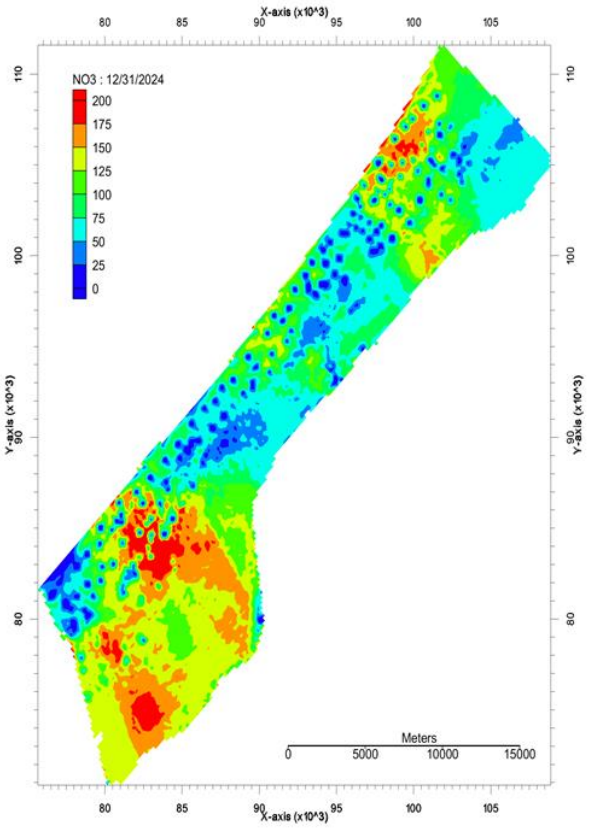

Figure 17. NO_3^- concentrations under Sc.5 for year 2025

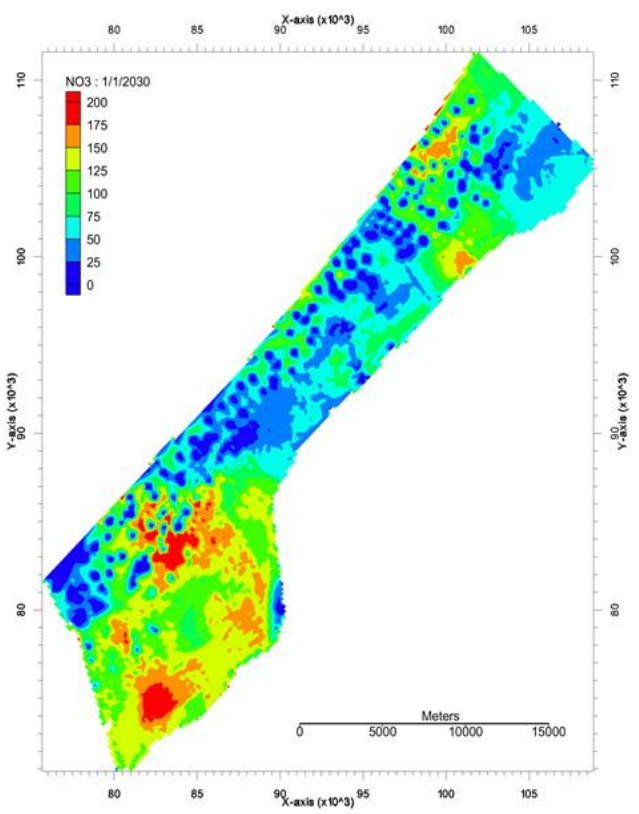

Figure 18. NO_3^- concentrations under Sc.5 for year 2030

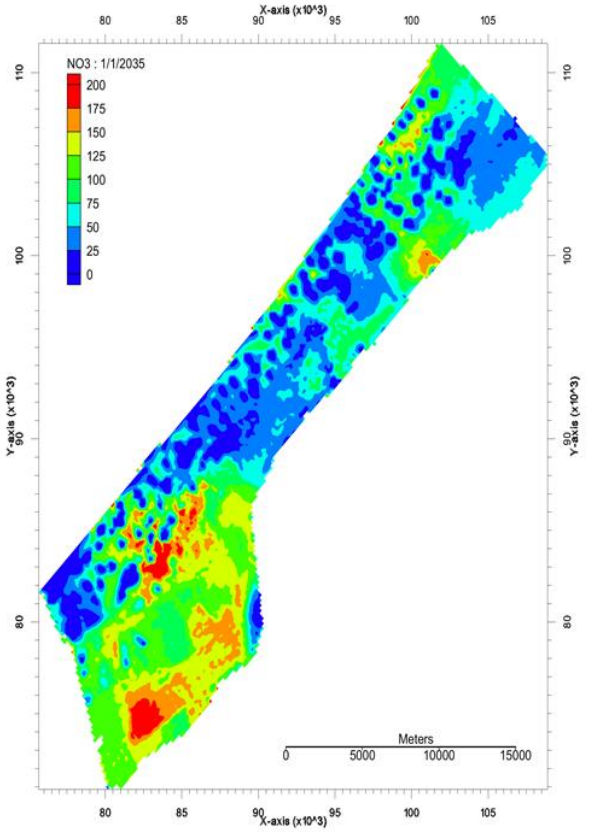

Figure 19. NO_3^- concentrations under Sc.5 for year 2035

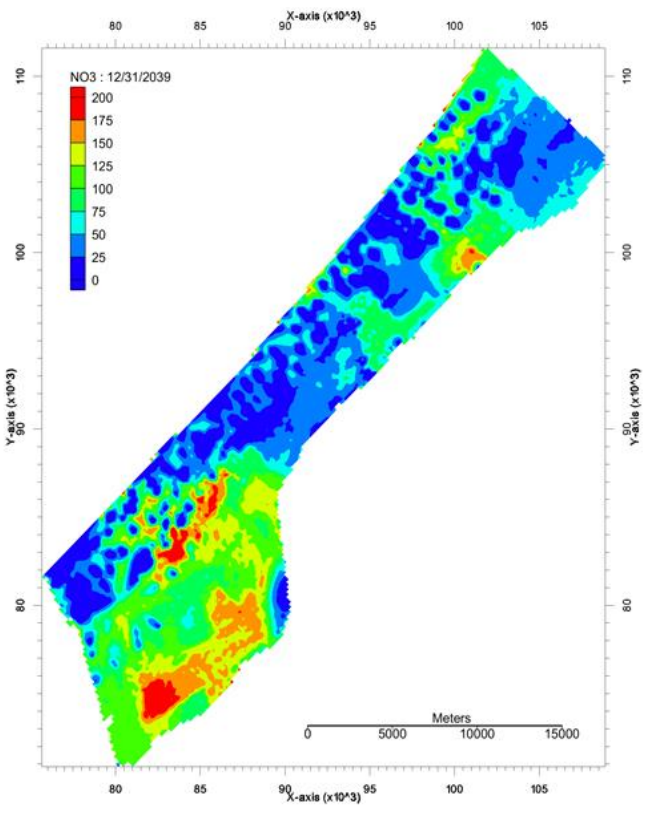

Figure 20. NO_3^- concentrations under Sc.5 for year 2040

Author contributions

Abdallah Jaroun: Investigation, Software, Validation, Writing-Original draft preparation **Ayşe Yeter Günal:** Methodology, Visualization, Writing-Reviewing and Editing

Conflicts of interest

The authors declare no conflicts of interest.

References

Abd Rabou A N (2019) Ornithofauna Prevailing at Al-Mawasi Ecosystem of the Gaza Strip, Palestine. Open Journal of Ecology, 9, 360-400

Abu Samra S (2014). Determination of Physico-chemical Properties of Top Soil in Gaza Strip for Agricultural Purposes. (Unpublished Master Thesis), Islamic University of Gaza.

Authority P W (2012). Rainfall Data in Gaza Strip.

Fryberg D L (1988). An Exercise in Ground-Water Model Calibration and Prediction, Ground Water, 26(3), 350-360.

Greitzer Y & Dan J (1967). The effect of soil landscape and Quaternary geology on the distribution of saline and fresh water aquifers in the Coastal Plain of Israel. Tahal Water Planning for Israel, Ltd.: Tel Aviv, Israel.

Hallaq E (2008) Determination of Mean Annual Rainfall in Gaza Strip Using GIS. Technique University of Sharjah, Journal of Pure & Applied Sciences 5(2).

Jamal K & Yaqubi A (2001). Water Resources and Management Issues, Unpublished report, Palestinian Water Authority, Gaza.

Selmi A (2013). Water management and modeling of a coastal aquifer case study (Gaza strip). PhD in Earth Sciences, University of Milan Bicocca, Faculty of Mathematics, Physics and Natural Sciences, Department of Earth and Environmental Sciences

Viessman W Jr & Gary L L (2002) Introduction to Hydrology, 5th ed, New York: HarperCollins College.

Wilson E M (1998). Engineering Hydrology, 4th ed, University of Salford.

Zheng C & Bennett G D (1995). Applied Contaminant Transport Modeling. Van Nostrand Reinhold, New York, 440 p.

Turkish Journal of Engineering
https://dergipark.org.tr/en/pub/tuje
e-ISSN 2587-1366

Effect of silica fume on the undrained strength parameters of dispersive soils

Ogan Öztürk*[1], Murat Türköz[1]

[1]*Eskisehir Osmangazi University, Engineering and Architecture Faculty, Department of Civil Engineering, Eskişehir, Turkey*

Keywords
Dipersive soil
Silica fume
Treatment
Strength

ABSTRACT

Dispersive soils are one of the problematic soils such as swelling and collapsible soils and they are common in many countries of the world. Due to dispersive soils, significant problems arise in road embankments and earth dams. Therefore, the use of such soils is possible with treatment. Silica fume (SF) as a waste material has been used in concrete production instead of partially cement, in the stabilization of expansive soils and in many civil engineering applications for different purposes. Within the scope of this study, to determine the dispersibility behavior of the soil sample, crumb test was performed. SF additive was used to improve the soil sample, which was determined to have high dispersibility. The compaction properties of the soil specimens mixed with SF in different proportions (0, 5, 10, 15, 20, 25 and 30%) were determined by the standard Proctor test. Crumb tests were performed to assess the dispersibility potential of the prepared specimens, and also unconsolidated and undrained (UU) triaxial tests were carried out to evaluate the strength parameters. UU experiments were performed under 20 kPa, 40 kPa and 60 kPa effective cell pressures on specimens cured for 1, 7 and 28 days because stabilization occurred at shallow depths in field applications. As a result, it was determined that the dispersibility feature of the soil sample was treated and the strength properties were improved depending on the SF content.

1. INTRODUCTION

Dispersive soils, which are not structurally stable, can be easily dispersed and eroded in the presence of water. When dispersive clay soils are used as building material in hydraulic structures, embankment dams and road embankments, they can cause serious problems and structural damage. Treatment of dispersive soils is usually done with chemical additives having different properties. This process eliminates the costs of transportation and material procurement that would occur when replacing problematic soil with quality material. Extensive studies have been carried out for many years to improve dispersive clay soils. Bhuvaneshwari et al. (2007) stated that dispersive soils can be improved by 5% lime or 2% lime and 15% fly ash additive. Savaş et al. (2018) showed that the use of 10% C class fly ash is sufficient for the improvement of dispersive soils. Using waste materials for the treatment of problematic soils can result in less pollution of nature and provide economic benefits. Many researches have been conducted on the use of silica fume (SF), which is an industrial waste material, as a substitute for cement in concrete production, especially in civil engineering applications. Liu et al. (2019) showed that the strength and freeze-thaw resistance of a pervious concrete lining material containing different amounts of SF (3%, 6%, 9% and 12%) instead of cement significantly increased. The positive effects of SF on concrete properties have been reported by many researchers (Zivica 2000; Wu et al. 2018; Sezer 2012). From the literature studies on the use of SF for soil stabilization, it is understood that the SF is used as an additive either alone or in combination with different additives such as lime and cement to improve the engineering properties of swelling soils (Kalkan and Akbulut 2004; Goodarzi et al. 2016; Türköz et al. 2018. For instance, Fattah et al. (2015) found that the bearing capacity of the square foundation built on a

* **Corresponding Author**

*(oganozturk@gmail.com) ORCID ID 0000-0003-4145-4175
(mturkoz@ogu.edu.tr) ORCID ID 0000-0003-0241-113X

Cite this article

Öztürk O & Türköz M (2022). Effect of silica fume on the undrained strength parameters of dispersive soils. Turkish Journal of Engineering, 6(4), 293-299

Research Article / DOI: 10.31127/tuje.1001413

Received: 27/09/2021; Accepted: 24/11/2021

soft clay soil mixed with lime-silica fume increased, Al-Soudany (2017) stated that the expansive soil treated with SF showed low plasticity and low swelling pressure, Goodarzi et al. (2016) found that the additive of cement and SF caused a significant effect in the treatment of swelling soils., and Kalkan (2009) determined that SF admixture effectively reduced desiccation cracks of expansive clays. In the study conducted by Kalkan (2011), the effect of wetting-drying cycles on the swelling behavior of a clay soil modified with different percentages of SF (10%, 20%, 25%, and 30%) was investigated. The positive effect on the swelling percentage and swelling pressure of modified soil was observed in the samples prepared at 25% to 30% SF additive level. Topçu and Kaval (2001) also conducted a study on the economic analysis of the use of silica fume in concrete.

The use of industrial wastes as an engineering material for the improvement of problematic soils can lead to less pollution of the nature and also provides economic benefits. Although SF is used in many industries, there is not enough study about its potential effect on the treatment of dispersive soils. It is obvious that the performance of the silica fume additive used for shallow stabilization in engineering applications should also be addressed in dispersible soils.

2. MATERIAL and METHOD

Soil samples used in the tests were excavated from a depth close to the surface from Afyon province in Turkey. ASTM's (2007) standard methods were followed in sampling and sample preparation stages. Atterberg limits, sieve analysis, hydrometer, and specific gravity tests were carried out for the identification of the soil. From the results of the sieve analysis, it was determined that the soil contains 0% gravel, 23% sand, 46% silt and 31% clay. The soil sample having 51% liquid limit and 24% plasticity index values was classified as high plasticity clay (CH) according to the Unified Soil Classification System.

Silica fume was obtained from Antalya Electrometallurgy Corporation. The specific gravity of SF used in the study is 2.32. The chemical properties of the soil sample and silica fume used in the study are presented in Table 1. Chemical analyses presented within the scope of the study were performed at Eskişehir Osmangazi University Central Research Laboratory.

Table 1. Chemical properties of the soil and silica fume

Property	Silica Fume (%)	Soil (%)
SiO_2	66.92	52.27
MgO	9.52	1.68
K_2O	4.66	3.42
Na_2O	4.52	1.61
Cr_2O_3	3.48	-
Fe_2O_3	1.27	6.47
Al_2O_3	1.22	16.58
CaO	0.98	5.13
Loss of ignition	4.77	11.76

2.1. Preparation of Soil Specimens

The soil sample, which was taken from the field and brought to the laboratory, was dried in an oven at 105 ° C for 24 hours since it was in lump form due to its natural water content. Oven drying was preferred because air drying would take a long time due to the high fines content of the samples and because it was easy to represent the same initial state in the ongoing experiments. In order to obtain a uniform distribution of the samples coming out of the oven drying, the samples were crushed with a plastic mallet and passed through sieve no 4. The sieved samples were blended in a large container and transferred to sacks. Due to the humidity of the laboratory environment, they were kept in sacks for about 2 weeks to maintain constant water content. Samples with fixed initial water content were homogeneously mixed separately in 6 different SF contents at the rate of 0, 5, 10, 15, 20, 25, and 30 % of their dry weight.

Compaction characteristics of the soil samples mixed with different silica fume (SF) additive percentages were determined by Standard Proctor test.

2.2. Crumb Test

The crumb test was developed to determine the behavior of dispersive clays in the field. Later, this experiment became used in laboratories as well. For the test, either cube samples with 15 mm side lengths are prepared in the natural water content or samples prepared by compression with compaction characteristics are used. The sample is carefully placed in a 250 ml porcelain bowl filled with distilled water. With the reaction of the soil with water, the particles of colloidal size begin to separate and turn into suspension in the water. Classification is made by observations at certain time intervals. Crumb test was carried out by considering the US Corps of Water Affairs standard methods USBR 5400 (1989).

No reaction – The soil sample may melt and move towards the bottom of the porcelain bowl. However, the turbidity caused by the colloids in the suspension is not seen.

Low-Moderate reaction – There are obvious clues to the presence of colloids in the suspension. The colloids may be on the very surface of the sample or may be found as a very thin imprint on the bottom of the porcelain bowl.

Strong reaction - The colloidal cloud covers the bottom of the bowl, usually in a thin layer. In extreme cases, the water in the porcelain bowl becomes completely cloudy.

2.3. Unconsolidated-Undranied (UU) Triaxial Test

In general, UU test results are used for rapid loading on clay soils or post-construction stability analyzes of embankment dams. Theoretically, it is accepted that the shear strength (c) value found as a result of the unconfined compression test performed on saturated soils is the same as the shear strength found as a result of the UU test. Although the unconfined compression test is widely used to determine the

cohesion resistance of soils, it gives lower values due to the cracks in the sample and the absence of lateral stress. For these reasons, the UU test, which reflects the land stress state, was preferred in the evaluation of the strength parameters.

The specimens used in the experiments were prepared by compressing the ratio of height to diameter of 2 (H = 14 cm and D = 7 cm) in stainless steel tubes in the compaction characteristics. The samples taken out of the tubes were placed in plastic bags and exposed to the cure in the desiccator under suitable conditions for 1, 7, and 28 days. Thus, the effect of both silica fume additive and curing time on the strength was evaluated. The UU experiments were performed at low effective cell pressures (20, 40 and 60 kPa) because stabilization occurred at shallow depths in field applications.

3. RESULTS and DISCUSSION

In this section, each test result is divided into sub-headings and evaluated separately and the results are discussed based on the obtained results.

3.1. Compaction Test Results

The compaction characteristics obtained from the standard Proctor test on different percentages of silica fume-soil mixtures are presented in Fig. 1.

As seen in Fig. 1, there was a decrease in maximum dry density (MDD) values and an increase in optimum water content (OWC) values with increasing SF percentage. While the decrease in MDD value was significantly effective up to 15% SF content, the decrease was limited in increasing SF contents. The MDD value, which was 1.584 Mg/m^3 at 0% SF, decreased to 1.559 Mg/m^3 and 1.553 Mg/m^3 at 15% SF and 20% SF contents, respectively.

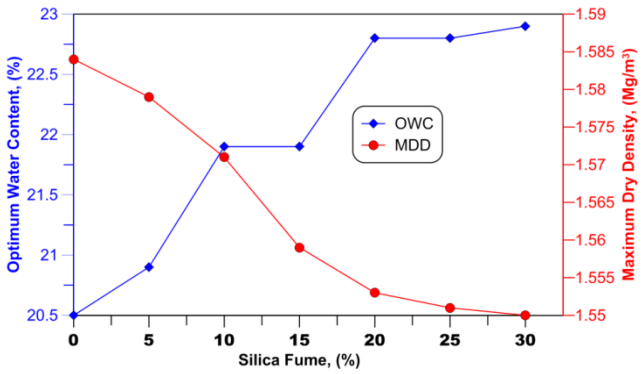

Figure 1. Variation of compaction characteristics with silica fume additive

OWC values showed a gradual increase up to 20% SF level and the increase in increasing SF percentages was limited. The increase in optimum water content (OWC) was relatively limited after 20% SF content. This is due to the lower specific gravity of the silica fume compared to soil and therefore the additional void volume due to the low specific gravity (Gs) and particle sizes of the SF additive samples. As stated in the study by Al-Azzawi et al. (2012), as a result of the replacement of sodium cations in dispersed soil with silicon cations in silica fume, the double layer thickness decreased, resulting in agglomeration of the grains.

3.2. Crumb Test Results

In this study, crumb tests were carried out to show the effect of silica fume on dispersibility. For the experiment, samples were prepared at the maximum dry density and optimum water content determined at each additive ratio. According to the degree of turbidity formed in the dispersion test, the samples were defined as “K1: non-dispersive”, “K2: intermediate”, “K3 and K4: dispersive”.

Fig. 2 is presented in order to show the effect of a one-day curing period on the dispersive soil used in this study. As it can be seen at the end of the crumb tests, SF has been quite effective on the stabilization of the dispersive soil in one-day curing condition. Colloidal clouding, indicative of the dispersive behavior in the soil sample, made the water in the porcelain bowl completely cloudy. At 5% and 10% SF contents, the colloidal cloud covered the porcelain bowl bottom in a thin layer. Colloidal turbidity is relatively reduced in 5% and 10% silica fume additives and the dispersion class is determined as K2. At 15% SF, the soil sample melted and moved towards the bottom of the porcelain bowl, but no turbidity caused by the colloids in suspension. Therefore, the dispersion class at 15% SF was evaluated as K1. The dispersion test class did not change with increasing additive percentages.

3.3. UU Triaxial Test Results

UU experiments were performed on samples prepared by compression in compaction characteristics at 20 kPa, 40 kPa and 60 kPa confining pressures. In order to evaluate the effect of the curing time, the prepared samples were cured for 1, 7 and 28 days.

An example of the deviator stress-strain relationship is presented in Fig. 3 to illustrate the effect of the 15% SF additive on the UU test results. Similar relationships were obtained for all other SF percentages, and the deviator stress and strain values at the moment of failure from the peak point of the curves were determined.

All the results found are presented in Table 2. It can be seen from Table 2 that the greatest deviator stress is obtained at 15% SF content after 1 day of curing. Depending on the increasing curing time, the increase in deviator stress was found at lower unit deformation values. In other words, while there was no significant difference in deviator stresses at SF contents greater than 15% SF content, there was a decrease in failure unit deformations.

The failure envelopes drawn using the strength parameters determined on the basis of the Mohr-Coulomb failure criterion are presented in Figs. 4-9.

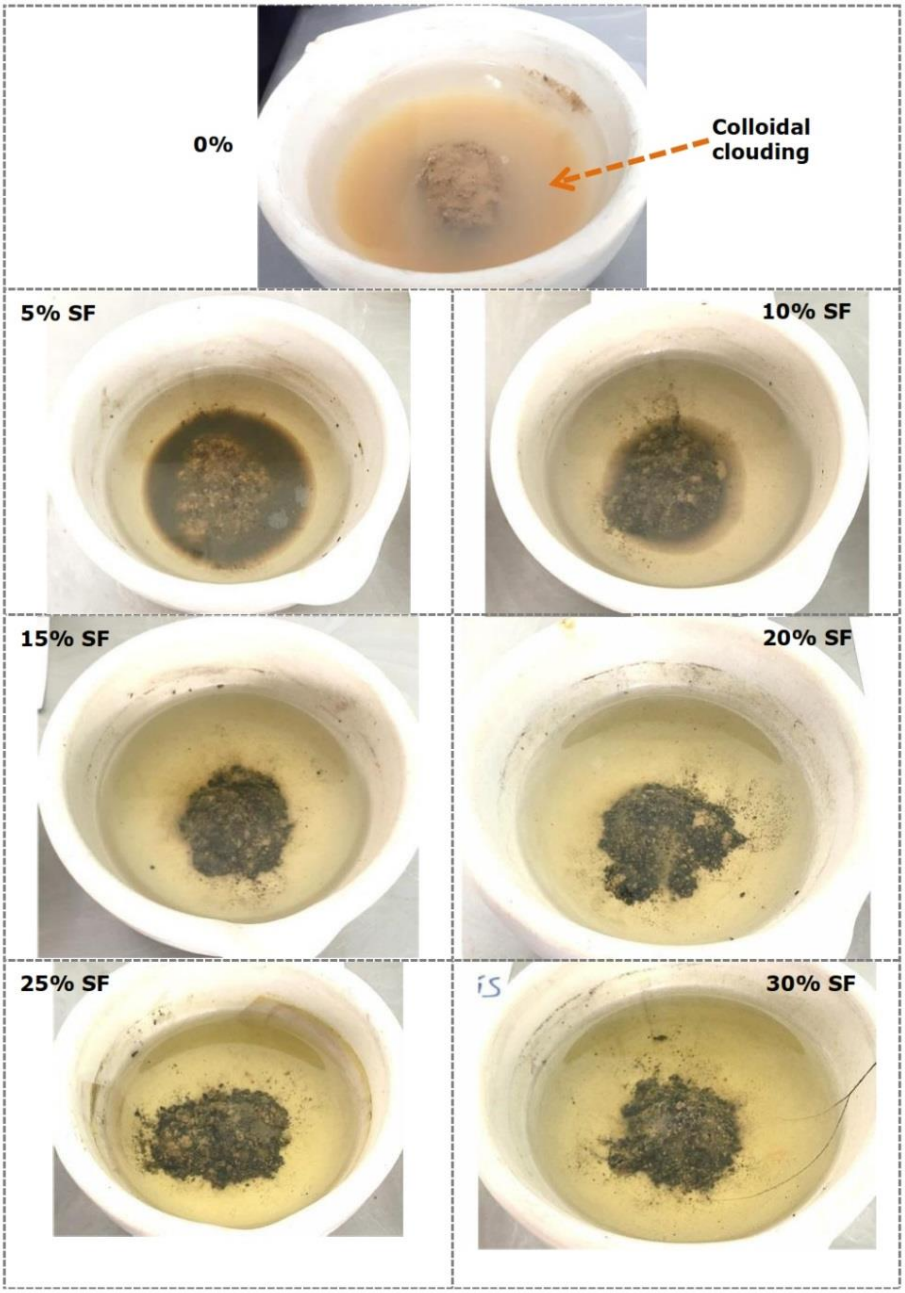

Figure 2. Images of the crumb test results

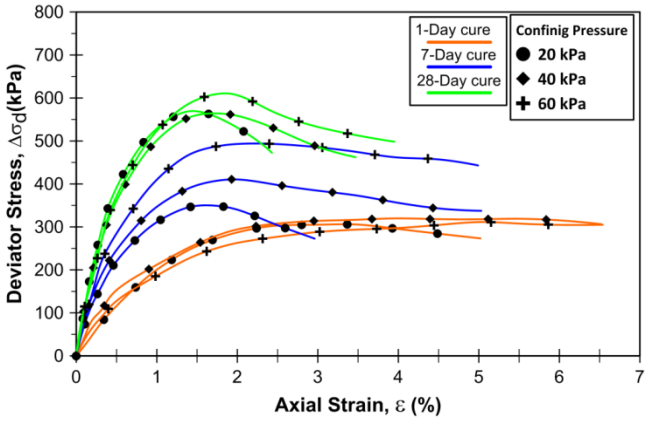

Figure 3. Stress-strain relationship for soil with 15% SF additive content

Samples did not have full saturation since the experiments were performed on samples prepared by compression at their compaction characteristics. For this reason, the envelopes of failure have been inclined. As a result of the UU tests, both cohesion and internal friction angles were determined as shear strength parameters. Especially in clay soils, the cohesion of the soils on the strength is important and has priority in the evaluations. The curing time is also important on the strength in order for the necessary chemical reactions to take place, especially in studies using additives. As seen in Figures 4-9, there was an increase in cohesion values depending on the increasing curing time. Especially after 28 days of cure, the increase in cohesion values was more pronounced.

The final results of the shear strength parameters obtained in the failure envelopes are presented in Table 3.

Table 2. Influence of SF additive contents and curing time on the UU test results

SF (%)	1-Day cure			7-Day cure			28-Day cure		
	σ_3 (kPa)	$\Delta\sigma_d$ (kPa)	ε_u (%)	σ_3 (kPa)	$\Delta\sigma_d$ (kPa)	ε_u (%)	σ_3 (kPa)	$\Delta\sigma_d$ (kPa)	ε_u (%)
0	20	281.9	5.01						
	40	301.7	5.02						
	60	310.2	5.00						
5	20	235.0	5.52	20	335.0	1.80	20	460.0	1.80
	40	286.8	5.53	40	372.0	2.30	40	474.0	2.10
	60	341.5	6.00	60	435.0	2.10	60	493.0	2.35
10	20	268.5	3.46	20	345.0	1.70	20	527.0	1.55
	40	300.6	3.99	40	415.0	2.20	40	545.0	1.67
	60	325.1	4.99	60	450.5	2.94	60	565.0	2.00
15	20	305.7	3.48	20	350.0	1.57	20	570.0	1.42
	40	319.9	3.97	40	410.6	1.96	40	585.0	1.63
	60	348.0	5.03	60	492.2	1.94	60	602.0	1.72
20	20	250.9	3.95	20	380.0	2.20	20	574.0	1.80
	40	288.7	5.51	40	425.0	2.23	40	587.0	1.84
	60	324.4	6.55	60	485.0	2.50	60	602.0	1.90
25	20	231.0	2.99	20	410.5	1.99	20	650.0	1.65
	40	258.0	3.52	40	480.0	2.00	40	680.0	1.85
	60	303.7	5.47	60	519.0	2.30	60	690.0	1.60
30	20	253.5	3.02	20	390.0	2.30	20	654.0	1.80
	40	297.5	5.00	40	454.0	2.10	40	680.0	1.95
	60	310.0	6.53	60	562.0	2.00	60	710.0	1.92

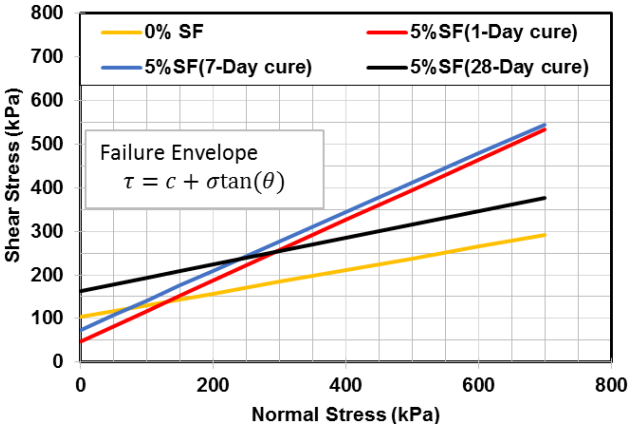

Figure 4. Effect of curing and 5% SF on failure envelope

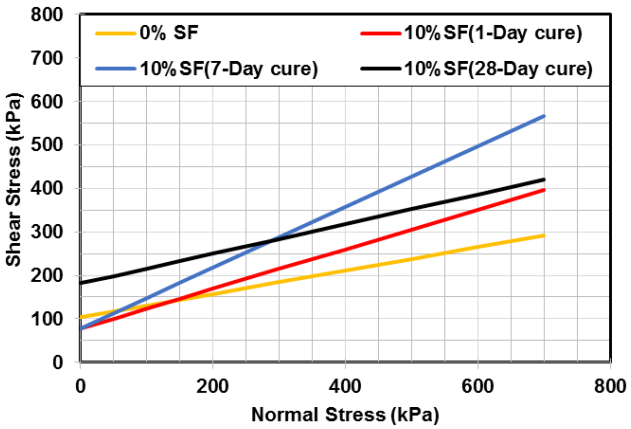

Figure 5. Effect of curing and 10% SF on failure envelope

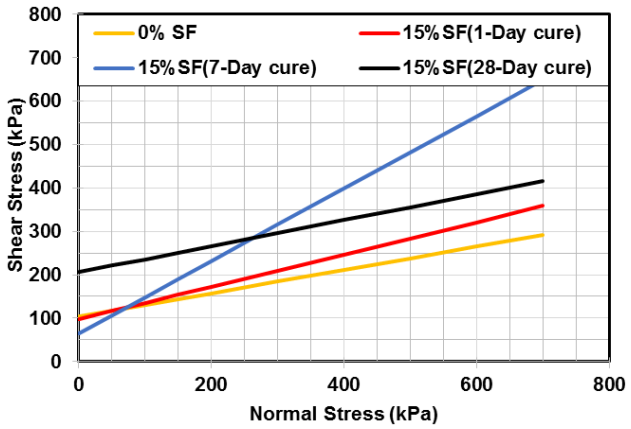

Figure 6. Effect of curing and 15%SF on failure envelope

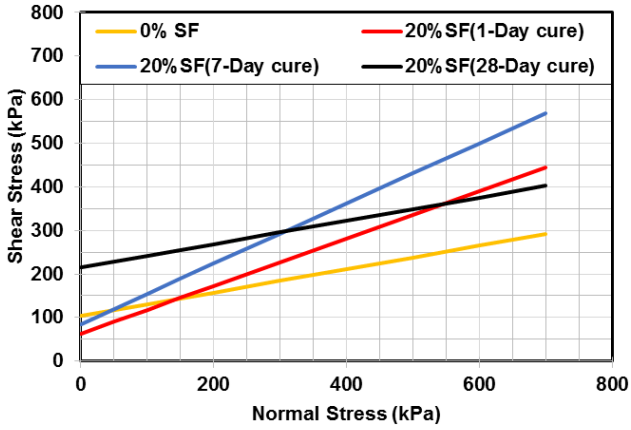

Figure 7. Effect of curing and 20% SF on failure envelope

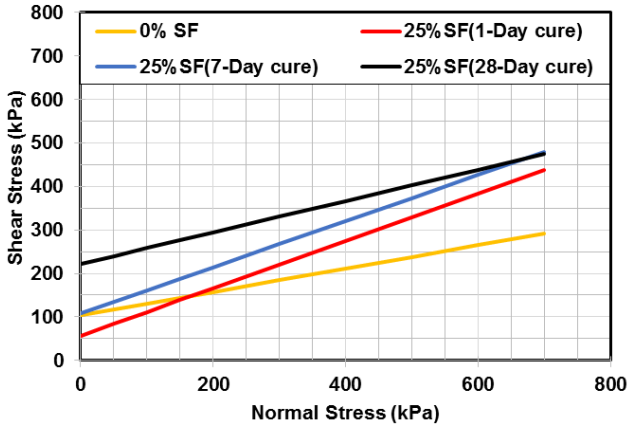

Figure 8. Effect of curing and 25% SF on failure envelope

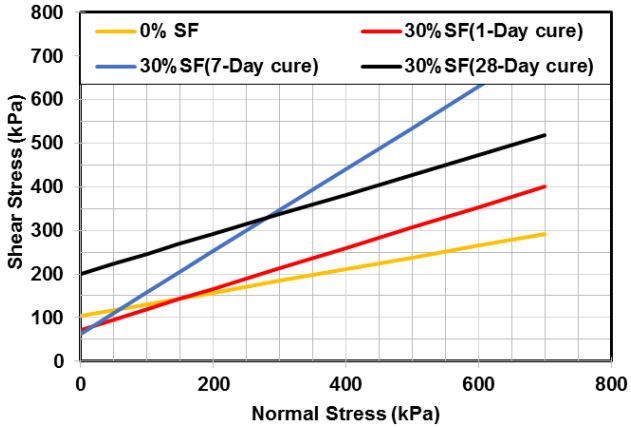

Figure 9. Effect of curing and 30% SF on failure envelope

Table 3. Effect of curing time and SF on shear strength parameters obtained UU tests

SF (%)	1-Day cure		7-Day cure		28-Day cure	
	c (kPa)	Φ (˚)	c (kPa)	Φ (˚)	c (kPa)	Φ (˚)
0	103.29	15.11	103.29	15.11	103.29	15.11
5	47.35	34.83	74.34	33.96	163.73	17.01
10	77.59	24.52	77.00	35.01	181.76	18.79
15	97.88	20.41	64.27	39.87	206.31	16.61
20	63.66	28.61	85.12	34.65	214.60	15.03
25	56.63	28.60	108.03	27.95	221.99	19.84
30	72.52	25.10	63.49	43.29	201.23	24.33

When Table 3 is evaluated in general, an increase in cohesion values and a decrease in internal friction angle values were obtained depending on the increased curing time and SF additive. It has been observed that at 15% SF content, cohesion of the soil increases from 97.88 kPa to 206.31 kPa at 28 days of curing period.

4. CONCLUSION

In this study, the stabilization of the dispersive soil with silica fume, which is a waste material, and its effect on the strength properties of the soil were investigated. As a result of this experimental study, it was seen that silica fume could be used in the stabilization of dispersive soil. In addition, significant increases in strength were observed depending on the curing time, thanks to the silica fume with high silica content. Although performed under low confining pressures, the UU test results showed a significant improvement in failure envelopes, especially at 15-20% SF content. In future studies, it is recommended to evaluate the effect of SF on strength by performing UU tests under higher confining pressures.

ACKNOWLEDGEMENT

This study includes the initial results of Ogan Öztürk's doctoral study, the corresponding author, and was supported by the Scientific Research Project of Eskisehir Osmangazi University (Project No: 201915037).

Author contributions

Ogan Öztürk: Investigation, Experimental, Writing. **Murat Türköz:** Conceptualization, Design, Reviewing and Editing.

Conflicts of interest

The authors declare no conflicts of interest.

REFERENCES

Al-Soudany Y K (2017). Improvement of expansive soil by using silica fume. Kufa Journal of Engineering, 9(1), 222–239.

ASTM E (2007). 8/E 8M Annual book of ASTM standards. ASTM.

Al-Azzawi A A, Daud K A & Sattar M A A (2012). Effect of silica fume addition on the behavior of silty-clayey soils. Journal of Engineering and Development, 16(1), 92-105.

Bhuvaneshwari S, Soundr B, Robinson R G & Gandhi S R (2007). Stabilization and microstructural modification of dispersive clayey soils. Proceedings of First Sri Lankan Geotechnical Society (SLGS) International Conference on Soil and Rock Engineering, August 6-11, Colombo.

Fattah M Y, Al-Saidi A A & Jaber M M (2015). Improvement of bearing capacity of footing on soft clay grouted with lime-silica fume mix. Geomechanics and Engineering, 8(1), 113-132.

Goodarzi R, Akbari H R & Salimi M (2016). Enhanced stabilization of highly expansive clays by mixing cement and silica fume. Applied Clay Science, 132-133, 675–684.

Kalkan E & Akbulut S (2004). The positive effects of silica fume on the permeability, swelling pressure and compressive strength of natural clay liners. Engineering Geology, 73(1-2), 145-156.

Kalkan E (2009). Influence of silica fume on the desiccation cracks of compacted clayey soils. Applied Clay Science, 43(3-4), 296–302.

Kalkan E (2011). Impact of wetting–drying cycles on swelling behavior of clayey soils modified by silica fume. Applied Clay Science, 52(4), 345-352.

Liu H, Luo G, Wang L, Wang W, Li W & Gong Y (2019). Laboratory evaluation of eco-friendly pervious

concrete pavement material containing silica fume. Applied Sciences, 9, 73.
Savaş H, Türköz M, Seyrek E & Ünver E (2018). Comparison of the effect of using class c and f fly ash on the stabilization of dispersive soils. Arabian Journal of Geosciences, 11(20), 1-13.
Sezer G İ (2012). Compressive strength and sulfate resistance of limestone and/or silica fume mortars. Construction and Building Materials, 26(1), 613–618.
Topçu İ B & Kaval M (2001). Economical analysis of use of silica fume in concrete. Journal of Eng.&Arch.Fac.Osmangazi University, 14(1), 18-31.
Türköz M, Savaş H & Tasci G (2018). The effect of silica fume and lime on geotechnical properties of a clay soil showing both swelling and dispersive features. Arabian Journal of Geosciences, 11(23), 1-14.
USBR 5400 (1989). Determining Dispersibility of Clayey Soils by the Crumb Test Method, Earth Manual II, United States Department of the Interior Bureau of Reclamation, 414-418.
Zivica V (2000). Sulfate resistance of the cement materials based on the modified silica fume. Construction and Building Materials, 14(1), 17–23,
Wu W J, Wang R, Zhu C Q, & Meng Q S (2018). The effect of fly ash and silica fume on mechanical properties and durability of coral aggregate concrete. Construction and Building Materials, 185, 69–78.

Turkish Journal of Engineering
https://dergipark.org.tr/en/pub/tuje
e-ISSN 2587-1366

Ship tonnages determined by the world economic growth with game theory

Devran Yazır*[1], Bekir Şahin [2], Tsz Leung Yip[3]

[1]*Karadeniz Technical University, Faculty of Marine Sciences, Maritime Transportation and Management Engineering, Trabzon, Turkey*
[2]*International Maritime College Oman, Suhar P.C. 111, Oman*
[3]*Hong Kong Polytechnic University, Department of Logistics and Maritime Studies, Hong Kong*

Keywords
Decision Making
Competition Environment
Game Theory
Maritime Companies
Mathematical Model

Abstract

Game theory is a discipline that examines subjects such as negotiation, conflict and cooperation between individuals, organizations, and companies by using mathematical models. Game theory is interested in understanding interaction between companies each other companies and individuals, particular decisions made by individuals and their effects on other individuals. The aim of the study is to investigate the maritime companies in a competitive environment where economic imbalances take place. For this purpose, the economic data reached through the International Monetary Fund (IMF) have been used. In this study, the effect of the increase in the economy over the increase in the tonnage of maritime transport and the effects of the tonnage over the excess or shortage in the market are calculated by using the game theory technique. In this respect, the issue of how long the overall tonnage increase should continue in the economy is taken into consideration. At the same time, moving economically with forward-looking estimates has also made the decision-making process more difficult.

1. INTRODUCTION

The economy is growing day by day in the developing world. This growth is due to the factors of profit and loss in the economy. The growth of the economy is generally achieved through the hand-over of products. As the products change hands, the value they receive increases or decreases. This is part of the transportation industry wherein the transport distance of a product, the amount of transport, the costs of the product formation increase the cost of that product (Sahin and Soylu, 2020). An increase in cost will also increase the selling price of the product. The sale price will be added at a certain level. Increases in cost are derived from products. Profit is one of the biggest factors for economic growth (Yazir and Sahin, 2017). Products often need to be replaced to change hands. The displacement is provided by transport. The greatest part of the world's transport is done through maritime transport. This mode of transport is specialized in transporting large quantities of products at long distances with minimal cost. Therefore, the share of ocean transportation is great in the continuity of the economy that has been going on for centuries. Maritime transport contributes to the economy. But the impact on the economy is reciprocal. The higher the rate of economic development, the more transportation activities increase in proportion. The number of vessels or tonnages must increase for the transport activities that tends to increase (Sahin and Yip, 2017). The more the products need to be transported, the transport tonnage gets greater. In that case, newbuilding ships are built so that the transportation tonnage is increased (Sahin et al, 2020). The carrying capacity, i.e., tonnage, increases so that the economy improves. Then, maritime companies tend to build more ships. For more vessels, the production capacity in the shipyards increases (Yazir et al, 2021). As it can be seen, there are trade-offs during this process and game theory can be utilized to decide on the tonnage of transportation which can change maritime companies making forward-looking plans to be strong in the economy. They need to make decisions with

* **Corresponding Author**
*(dyazir@ktu.edu.tr) ORCID ID 0000-0002-6825-8142
(bekirs66@gmail.com) ORCID ID 0000-0003-2687-3419
(t.l.yip@polyu.edu.hk) ORCID ID 0000-0002-7277-7666

Cite this article
Yazır D, Şahin B & Yip T L (2022). Ship tonnages determined by the world economic growth with game theory. Turkish Journal of Engineering, 6(4), 300-305

Research Article / DOI: 10.31127/tuje.1001664
Received: 27/09/2021; Accepted: 24/10/2021

the stability they follow. The use of the decision-making structure comes into front here. Decision making can be defined as selecting the most appropriate one from two or more options. The choices to be taken here are whether or not shipbuilding will be done. Certain factors which are controlled and uncontrolled are involved in this decision-making process. The amount of production of variable new vessels that can be controlled in the subject matter in question. Uncontrollable is the irregular growth and shrinkage of the economy. These two variables and the person who makes the decision finally arrive. The result is the final decision. Decision-making process is an inevitable influence in game theory. Because there is not a single sea company in the world. The number of players in the marine transportation industry is very high. Apart from being too many players, the standards and categories are too high. In terms of freight they carry, maritime transport has a diversity of players. In this case, the interests of all the players who are going to be able to collectively make a load of goods are affected. The new tonnage at a maritime company is linked to the increase and decrease in tonnage that other companies will create.

2. LITERATURE REVIEW

The economy is greatly influencing the world order. However, it is very difficult to make a comment on the future while the history of the economy can be recorded literally. However, game theory is a big help when making economic decisions. The game theory which known as Nash theory, earned the Nobel Prize in 1994 for the mathematician John Nash. Nash calculated that there might be a balance on a game and changed the way of looking at the economic structure going on until that time. This simple concept helps economists learn how to set prices for competing firms, how governments should design their auctions to get the most from bidders, and how groups will sometimes explain self-fulfilling decisions. Stanford University's Business Institute publishes an essay on Nash equilibrium. In this study, it was written that optimizing Nash equilibrium would be especially dynamic games. Accordingly, the player must change his tactics so that the balance remains constant and not distorted. A player decides and implements it absolutely. Because the best-case strategy is in the middle. In Nash game theorem, it is assumed that the players always fit into their initial plans (Govindan and Wilson, 2005). In a study conducted at the University of Chicago Economics department, it was mentioned that Nash completely changed the price theory. Prior to theorem, pricing was a more analytical methodology in the economy. This analytical analysis has become a valuable guide for economists as well as being easy and practical. That's why he did not think it could be another approach to anyone. But the system was very narrow. It was very difficult to intervene in these price theories. Firms have different information and different negotiation situations. This has not been applied to their standard price theory. The wider analytical perspective of gaming theory has freed practical economic analysis from these methodological constraints. Methodological limitations cannot prevent us from evaluating market and non-market systems on an equal footing and accepting basic links between economic, social and political institutions in economic development (Myerson, 1999).

The Economist magazine handled the Nash equilibrium by taking the darkest example in a number in 2016. A good example is that there are two suspects of a murder. Two suspects are cross-examined. And if they confess to this question, they will be given information about how much punishment they will receive. The two suspects have to decide each other unaware. Depending on the situation, the penalties may fall, they may not be punished at all, or both may be punished. This is reflected in the economy in the decision-making process. The game theory is that everyone in a group makes the best decision for themselves (according to what others expect to do). And nobody can do better by changing the strategy. Each member of the group makes the best of it. Economists who apply this theory to the real-world use Nash equilibrium to predict how companies will respond to the prices of their competitors (URL-1, 2016). The subject of mathematics is often uncontrolled variables. In other words, changes in the system considered by our own decision are the undetermined variables. In mathematical problems, it is revised in game theory. If there are two persons in the game, the parties must play in accordance with the rules and make the strategy fit numerically. In a game played in this way, each player tries to maximize his winnings or points and tries to minimize his opponent's. Whether or not the game has any optimum or fixed result depends on whether a player is taken as a target to the min-max situation, depending on that of the other player. For this reason, game theory has to do with economic problems. Thus, game theory can be formulated with mathematical terms or expressions. Mathematical game theory, which is defined as the technical relations network, helps the economic problems in a particular group (Alien, 1956).

In a study written by Meca et al. (2004), collaborating companies have distributed their collaborative game theory model and inventory costs with the help of proportional rules, together with their specific inventory costs information. In case of cooperation, they have reduced their own inventory costs and total stock costs. They examined the economic production model with a collaborative game theory model. In the case of stockless and in the case of firms producing, they proposed an alternative distribution rule similar to the proportional rule in reducing and distributing costs (Meca et al., 2004).

In order for an enterprise to operate effectively and efficiently, the items and materials used in the production or sold must be supplied on time and in the required amount. According to each business activity area, it is necessary to have some items or materials available in order to perform the production or to respond to the requests of the customers. These items and materials that are held by the company are generally referred to as stocks (Chase et al., 1981; Sulak, 2008).

He et al. (2020) has mentioned the future prospects and challenges for the application of game theory in integrated energy systems. New game models were introduced to the integrated energy system and a mixed

game model was considered to solve the related problems (He et al., 2020).

Lin et al. (2021), noted that environmental sustainability is playing an increasingly important role in the maritime industry. Green strategies such as speed reduction, fuel switching, alternative fuels can reduce harmful emissions from ships and increase environmental sustainability. An evolutionary game theory framework embedded in the pricing model in shipping has been proposed (Lin et al., 2021).

In this study, the effect of the increase in the economy over the increase in the tonnage of maritime transport is investigated by using the game theory technique.

3. METHOD

Game theory is an interdisciplinary approach that has its own characteristics that examine human behavior (Aktan and Bahçe, 2013). John Nash writes in his "Unclear Games" article about n-person ending games and defining the balance point of these games. This article initially tells us that Nash is the most important part of the theory of equilibrium and adds: "This idea allows us to generalize the solution concept of our two-person zero-sum games. As a result, the set of equilibrium points of two-person zero-sum games is simply a set of counter-good strategies". In other words, a balance point is a strategy profile, where each player's strategy is the best response, they can give to other players' strategies. This equilibrium point is called Nash equilibrium (URL-1, 2016; Alparslan, 2018). At the core of the Nash equilibrium concept is the best response approach. According to Nash, the strategy of each of the players forming the strategy pair, which is the candidate for a solution of a two-player game, should be the best answer to the other strategy, which is anticipated to be played by the opponent player. In other words, Nash equilibrium; is a set of strategies for each player making the best they can, while his opponent is figuring out his strategies. In this balance, which is one of the bases of the uncooperative game theory, no player wants to change his choice when the action of the opponent player is fixed. In other words, no player can increase his profits by changing his own action when his opponent's strategy is fixed. To say that the Nash equilibrium puts forward self-conflicting and strategic stability characteristics are the best response that no player can express on the basis of a deviation from his stated strategy. Regardless of whether the opponent player chooses which strategy to dominate, there is a process in which players try to find out the best they can do themselves. The resulting dominant strategy balance is the only Nash equilibrium in its rank.

In the static game model, assuming that each player chooses the strategy that the other player will create the best answer to the selection of the actual strategy, the strategy pairs with this feature will be the game solution. This argument contains two elements.

1. Each player must choose a strategy, which will create the best response to the opponent's anticipated strategy selection.
2. In the event of equilibrium, the beliefs of the players, of their opponents about strategy choices, should be rational in the sense that these expectations have been fulfilled.

While assuming that these requirements will try to predict the strategy that a player will choose from his opponent, the second requires that the same player's expectations of his opponent's game are consistent with the strategies actually played by his opponent.

The elements of a decision problem can be considered as follows:

1. Decision maker: Responsible and decision-making.
2. Controllable variables: There are two or more strategies for making decisions. Strategies are part of the system and are under the control of the decision maker. The chosen strategy will be able to fulfill the desired goal as best as possible.
3. Uncontrollable variables (events): These variables are variables that affect the achievement of the goal and are outside the control of the decision maker. These variables are outside the system, and it is not known exactly which one is going to happen. For example, economic, political, social, cultural and ideological factors, climatic conditions, technological developments, competitions and laws.
4. Conclusion: The result of any strategy being chosen by the decision maker and a certain uncontrolled variable taking place.

It is possible to determine the method to be followed when considering the issue of decision making and all the elements of the process.

1. A decision criterion is selected first.
2. The possible outcomes of the decision process and possible decisions are defined.
3. It is determined what kind of probability distribution is to be applied in the decision process and the possible probability values are given to the inputs of the decision matrix.
4. A function to measure the benefit is determined.
5. An experiment is made for decision options.
6. The possibilities given to the inputs are reviewed and corrected if necessary, according to the test results.
7. For each possible decision, the risk of process entry is calculated.
8. Using the probabilities given to the inputs, the expected risk of each possible decision is calculated.
9. The minimum expected risky decision is optimal.

Thinking about events in all possible ways and anticipating what might be the result, then choosing the best can be made contradictory. For this reason, game theory is based on maximizing the winnings of the decision-maker or the elector and minimizing the losses. Decision matrix is used to select the best strategy in the decision process. The decision matrix is as follows (Rençber, 2012).

Table 1. Decision Matrix (Rençber, 2012)

STRATEGİES	EVENTS N1N2…… …… …… Nn
S1	X11……X1n
S2	X21……X2n
Sm	Xm1……Xmn

In the decision matrix;

S1, S2, ..., Sm: Strategies (m variables that can be controlled).
N1, N2, ..., Nn: Events (n uncontrollable variables).
Xij: The choice of the intellectual strategy by the decision maker.

Conclusion
(i = 1, 2, ..., m): Index of strategy.
(j = 1, 2, ... n): Index of events.

4. APPLICATION

The research material is the changes in information from the IMF for world economic growth between 2015, 2016 and 2017. During this time, the same increases in freight rates and transport capacities of all the vessels worldwide have been adapted to the situation in the last 3 years as deadweight. In the meantime, UNCTAD's reports on the yearly maritime sector are taken as references. In this case, the growth of world economic growth and transport is described as interconnected strategies. Freight rates affecting the world economy and its first impact freight and the amount of freight that can be carried will change accordingly (UNCTAD, 2015; UNCTAD, 2016; UNCTAD, 2017). Analysis of the studied progeny was carried out using the Lindo pre-packaged program. The matrix method was used in the analysis. Maximin in the game matrix of the subject; as seen in Table 2 is equal to 3,5 and Minimax = 3,5. So Maximin = Minimax, there is the balance point of the game. The best strategy for this situation is the solution of the project. The formulas to be applied by the competitors in the matrix method are as follows (Rençber, 2012).

Table 2. The Matrix Method (URL-2: IMF)

Year	Real gross world product growth (Annual percent change)	Transport and insurance costs of international trade (Percentage share of the value of imports)	World fleet by principal vessel type (Thousands of dead-weight tons and percentage share)
2015	3,5	14,2	3,5
2016	3,2	15,4	3,48
2017	3,8	16,2	3,15

$$[\,X1, X2\,, X3\,] = \frac{\text{IadjA}}{\text{IadjAI}'} \tag{1}$$

$$\begin{bmatrix} Y_1 \\ Y_2 \\ Y_3 \end{bmatrix} = \frac{\text{adjAI}'}{\text{IadjAI}'} \tag{2}$$

$$g = \frac{|A|}{\text{IadjAI}'} \tag{3}$$

Meanings of symbols:

[X1, X2 , X3]: The positive and negative effects of years on the selection of strategies.
$[Y_1, Y_2, Y_3]$: The probability of choosing strategies.
A: Coefficient matrix.
adjA: The additional matrix of a matrix.
| A |: Determinant of a matrix.
I: A row vector whose elements are one (1) and equal to the size of matrix A.
I': Transposition of row vector I.
g: Game value

It is found that the coefficients of the project are in the matrix;

The coefficient matrix for the project is given below:

$$A = \begin{bmatrix} 3{,}5 & 14{,}2 & 3{,}5 \\ 3{,}2 & 15{,}4 & 3{,}48 \\ 3{,}8 & 16{,}2 & 3{,}15 \end{bmatrix} \tag{4}$$

If we denote the transpose of the matrix A by the symbol A':

$$A' = \begin{bmatrix} 3{,}5 & 3{,}2 & 3{,}8 \\ 14{,}2 & 15{,}4 & 16{,}2 \\ 3{,}5 & 3{,}48 & 3{,}15 \end{bmatrix} \tag{5}$$

The additional matrix of A is also:

$$\text{Adj A} = \begin{bmatrix} -7{,}866 & 11{,}97 & -4{,}484 \\ 3{,}144 & -2{,}275 & -0{,}98 \\ -6{,}68 & -2{,}74 & 8{,}46 \end{bmatrix} \tag{6}$$

Row and column vectors are;

$$I = \begin{bmatrix} 1 \\ 1 \\ 1 \end{bmatrix} \tag{7}$$

$$I' = [1 \quad 1 \quad 1] \tag{8}$$

The changes and developments in the market have been calculated as follows with the change of the strategies. The rise in tonnage in transportation has been calculated as the rise in freight rates resulting from economic growth.

$$[\,X1, X2, X3\,] = \frac{[1 \quad 1 \quad 1] \begin{bmatrix} -7{,}866 & 11{,}97 & -4{,}484 \\ 3{,}144 & -2{,}275 & -0{,}98 \\ -6{,}68 & -2{,}74 & 8{,}46 \end{bmatrix}}{[1 \quad 1 \quad 1] \begin{bmatrix} -7{,}866 & 11{,}97 & -4{,}484 \\ 3{,}144 & -2{,}275 & -0{,}98 \\ -6{,}68 & -2{,}74 & 8{,}46 \end{bmatrix} \begin{bmatrix} 1 \\ 1 \\ 1 \end{bmatrix}} \tag{9}$$

$$\frac{[-11{,}402 \quad 6{,}955 \quad 2{,}996]}{-1{,}451} = \frac{-11{,}402}{-1{,}451}, \frac{6{,}955}{-1{,}451}, \frac{2{,}996}{-1{,}451} \tag{10}$$

Here is the result:

$$\begin{aligned} X_1 &= 7{,}858028946 \\ X_2 &= -4{,}7932466037 \\ X_3 &= -2{,}06478 \end{aligned} \quad (11)$$

values are found.

According to years, we can reach the comments that can be made about the exchange and the progress of the data by the results of Y values. If the above is applied while Y values are found, the results are as follows.

$$\begin{bmatrix} Y_1 \\ Y_2 \\ Y_3 \end{bmatrix} = \frac{\begin{bmatrix} -7{,}866 & 11{,}97 & -4{,}484 \\ 3{,}144 & -2{,}275 & -0{,}98 \\ -6{,}68 & -2{,}74 & 8{,}46 \end{bmatrix} \begin{bmatrix} 1 \\ 1 \\ 1 \end{bmatrix}}{\begin{bmatrix} 1 & 1 & 1 \end{bmatrix} \begin{bmatrix} -7{,}866 & 11{,}97 & -4{,}484 \\ 3{,}144 & -2{,}275 & -0{,}98 \\ -6{,}68 & -2{,}74 & 8{,}46 \end{bmatrix} \begin{bmatrix} 1 \\ 1 \\ 1 \end{bmatrix}} = \frac{\begin{bmatrix} -0{,}38 \\ -0{,}111 \\ -0{,}96 \end{bmatrix}}{-1{,}451} \quad (12)$$

The Y values obtained after the operations are as follows:

$$\begin{aligned} Y_1 &= 0{,}261888353 \\ Y_2 &= 0{,}07649996 \\ Y_3 &= 0{,}661612681 \end{aligned} \quad (13)$$

Accordingly, the overall rating for equilibrium is Nash's equilibrium economic market and the rate that can be used is equal to the value of the game in the new year.

Game value:
As the determinant of matrix A is

$$|A| = -6{,}2662 \quad (14)$$

$$g = \frac{-6{,}2662}{-1{,}451} = 4{,}318538939 \quad (15)$$

Game value:

g = 4,318538939

According to the analysis, the economic growth rate is increased by about 0,26 and the freight rates are having a value of 0,07. Against this value, the carrying capacity should also increase by 0,66 which in both cases can achieve optimum gain. In this case, according to game theory, depending on the world economic structure, the balance point between freight and transport capacity should develop in this way. In this development, the parties have reached the economic equilibrium and achieved the most favorable earnings. In this case, both the economy will grow, and the freight price will increase with the change in freight price. The maximum increase in the freight price is determined by the game value, according to the growth rate of the economy and the increase in the carrying capacity.

3. CONCLUSION

According to game theory, depending on the economic structure of the world, the freight rate between the load and the carrying capacity is 0,07 while the carrying capacity should increase by 0,66 so that optimum gain can be achieved. Under these circumstances, the parties reach economic equilibrium and achieved the most favorable gain. In this case, both economies will grow, and freight prices will increase with the change in freight price. This study searched, how to transport, which is an economic activity, if it could develop within the transport sector, depending on the result of the Nash Equilibrium and the outcome given to us by the equilibrium. During this research, it is shown how freight rates change overall, as well as the impact of economic growth and the balance of transportation. The development in the world economy and the change in freight rates can be proportionally balanced over the world combined with the transport tonnage. If the growth in the future periods is in this situation, the growth in the sector will be reflected in the freight rate, which will cause the tonnage to increase. The study can provide forecasts on the market by providing different equilibrium ratios when estimated values of future years are put in place. This manuscript will help increase tonnage to future decision-making and the market and at the same time, this study will be the source of new studies on similar issues.

ACKNOWLEDGEMENT

Acknowledgements of support for the project/paper/author are welcome.

Author contributions

Devran YAZIR: Investigation, Methodology, Writing-Original draft preparation. **Bekir ŞAHİN:** Writing-Reviewing, Validation, and Editing. **Tsz Leung Yip:** Investigation, Writing-Reviewing, and Editing.

Conflicts of interest

The authors declare no conflicts of interest.

REFERENCES

Aktan C C & Bahçe A B (2013). Kamu Tercihi Perspektifinden Oyun Teorisi. Hukuk ve İktisat Araştırmaları Dergisi, 5(2), 93-117.

Alien R G D (1956). Mathematical Economics. London. Macmillan and co LTD New York. St martin's press. p. 494.

Alparslan F (2018). Oyun Teorisi. İktisat ve Toplum Dergisi 90. Sayı, p 65.

Chase R B & Aquilano N J (1981). Production and Operations Management: A life Cycle Approach. Third Edition, Irwin, USA.

Govindan S & Wilson R (2005). Refinements of Nash Equilibrium. Working Paper No. 1897, Economics.

He J, Li Y, Li H, Tong H, Yuan Z, Yang X & Huang W (2020). Application of Game Theory in Integrated Energy System Systems: A Review. IEEE Access, 8, 93380-93397.

Lin D Y, Juan C J & Ng M (2021). Evaluation of Green Strategies in Maritime Liner Shipping Using Evolutionary Game Theory. Journal of Cleaner Production, 279, 123268.

Meca A, Timmer J, Garcia-Jurado I & Borm P E M (2004). Inventory games. European Journal of Operations Research, 156, 127–139.

Myerson R B (1999). Nash Equilibrium and The History of Economic Theory. Journal of Economic Literature, 36, 1067-1082.

Rençber B A (2012). Karar Vermede Oyun Teorisi Tekniği ve Bir Uygulama. Uşak Üniversitesi Sosyal Bilimler Dergisi, 5(3), 97-108.

Sahin B & Soylu A (2020). Intuitionistic fuzzy analytical network process models for maritime supply chain. Applied Soft Computing, 96, 106614.

Sahin B & Yip T L (2017). Shipping technology selection for dynamic capability based on improved Gaussian fuzzy AHP model. Ocean Engineering, 136, 233-242.

Sahin B, Yip T L, Tseng P H, Kabak M & Soylu A (2020). An application of a fuzzy TOPSIS multi-criteria decision analysis algorithm for dry bulk carrier selection. Information, 11(5), 251.

Sulak H (2008). Stok kontrolü ve ekonomik sipariş miktarı modellerinde yeni açılımlar: ödemelerde gecikmeye izin verilmesi durumu ve bir model önerisi, Doktora Tezi, Süleyman Demirel Üniversitesi, Sosyal Bilimler Enstitüsü, Isparta.

United Nations Conference on Trade and Development. (2015). Review of Maritime Transport United Nations Conference on Trade and Development.

United Nations Conference on Trade and Development. (2016). Review of Maritime Transport United Nations Conference on Trade and Development.

United Nations Conference on Trade and Development. (2017). Review of Maritime Transport United Nations Conference on Trade and Development.

URL-1: what is the nash-equilibrium and why does it matter. (2016). https://www.economist.com/the-economist-explains (ET:12.03.2019).

URL-2: International Monetary Fund. http://www.imf.org/external/datamapper/(ET:10.03.2019).

Yazır D, Şahin B & Yip T L (2021). Selection of new design gas carriers by using fuzzy EVAMIX method. The Asian Journal of Shipping and Logistics, 37(1), 91-104.

Yazır D & Şahin B (2017). Linear Regression Approach for the Financial Risks of Shipping Industry. TransNav, the International Journal on Marine Navigation and Safety of Sea Transportation, 11(4).

Turkish Journal of Engineering
https://dergipark.org.tr/en/pub/tuje
e-ISSN 2587-1366

Comparison of experimental and numerical analysis of Quasi-Static punch shear test for stainless steel sheet material

Mehmet Şahbaz[*1]

[1]*Karamanoğlu Mehmetbey University, Faculty of Engineering, Mechanical Engineering Department, Karaman, Turkey*

Keywords
Sheet Metal
Finite Element Analysis
Punch Test

ABSTRACT

In this study, Quasi-Static Punch Shear Test (QS-PST) for AISI-304 stainless steel sheet material with 0.5 mm thickness was performed experimentally and numerically, then the results were compared. QS-PST was designed non-standard according to the need and is especially used to determine the puncture resistance of composite plate materials against low-speed loading. Since the results obtained from QS-PST are similar to those from ballistic tests, this has attracted the attention of researchers. The experimental study was carried out by integrating the die and punch which were specially produced for this test, into an electromechanical tensile-compression test device with a capacity of 100 kN. In order to define the material properties correctly in numerical analysis, the tensile tests of the relevant material were also carried out with the same device. Then, the CAD model of the experimental system was generated and Finite Element Analysis (FEA) was performed. In FEA, the mesh structure was determined as tetrahedral, since it gave closer results in such tests and the analyzes were performed by increasing the number of mesh from 16700 to 151800 elements. Finally, the experimentally and numerically obtained results were compared and it was observed that the result were very close depending on increasing the number of mesh.

1. INTRODUCTION

Sheet metal materials are most widely used material type in almost all industrial fields, from automotive to aeronautics, from food to agriculture (Aydın and Karaağaç 2019). These materials are exposed to external factors that negatively affect their lifetime, depending on the environment and conditions in which they are used. Or, they may lose their integrity by being subject to deformation in the face of uncalculated loadings, or they may lose their function by being deformed. In order to prevent such situations, manufacturers develop material production processes and apply different methods to make sheet materials more resistant to such undesirable situations. For example, galvanization or alloying processes applied for providing corrosion resistance in areas where corrosion is not desired. Similarly, types of stainless steel made with chromium-nickel reinforcement are widely used in mechanical engineering due to their high mechanical properties, chemical resistance to corrosion, and low costs. (Kaoumi and Liu 2018).

Along with technological developments, stainless steels are used in many sectors such as chemical and automotive industries, electronic devices, medical applications. Stainless steels are used as components in many applications due to their high tensile strength and ability to work at high temperatures. (Al-Bakri et al. 2016). Moreover, stainless steels are frequently preferred in food industry because of their high corrosion resistance properties (Çeliker et al., 2021).

Stainless steels are categorized according to their crystal phase and microstructure. According to this classification, they are named as; austenitic stainless steels (300 series), ferritic stainless steels (430, 442 etc.), martensitic stainless steels (403,410,420 etc.), and duplex (Ferritic-Austenitic) stainless steels (1.4362, 1.4507 etc.) (Türkoğlu and Ay 2021). After giving brief

* **Corresponding Author**
*(mehmetsahbaz@kmu.edu.tr) 0000-0001-6379-8345

Cite this article
Şahbaz M (2022). Comparison of experimental and numerical analysis of Quasi-Static punch shear test for stainless steel sheet material. Turkish Journal of Engineering, 6(4), 306-312

Research Article / DOI: 10.31127/tuje.1002507
Received: 30/09/2021; Accepted: 20/01/2022

information about sheet metals, especially stainless steels, some of the scientific studies in this field are briefly summarized. Köleoğlu et al., investigated the effects of plasticity models in their study, which model the plastic behavior of materials in sheet metal forming processes on finite element estimation. For this purpose, they examined different plasticity models in terms of both deformation and tearing (Köleoğlu et al. 2019). In a similar study, Vatansever and Esener analyzed the effects of calculation parameters on simulation precision and solution time with FEA of sheet metal forming. In particular, they determined the parameters that minimize the solution time and improved the solution time (Vatansever and Esener 2019).

Karajibani et al., on the other hand, presented a simulation-based approach for the determination of the forming layer curve (FLC) in bilayer metal sheets. In this study, they obtained the FLC of aluminum-1100 / copper-C10100 two-layer plate through numerical analysis and experimental research (Karajibani et al. 2017). In another study, Çağdaş and Taşkın, 2020. developed a modified analytical expression to determine the quasi-static pre-indentation loads of foam core sandwich beams with thin laminated galvanized steel surfaces, which may be valuable in the preliminary design phase. This analytical statement was confirmed by the indentation tests, and they also examined the effects of the surface layer lamination parameters on the indentation (Çağdaş and Taşkın 2020).

When the studies were examined, it was observed that there were intensive and different studies on sheet materials, and it was observed that both experimental and numerical studies were carried out. The produced sheet materials are tested, especially for chemical and mechanical resistance and whether they are suitable for the area of use during the production phase. Most frequently preferred mechanical tests for sheet materials are: tensile, three-point bending and hardness tests. However, tests for measuring the shear resistance of the material against puncture are not widely used on the surface of highly loaded impacts concentrated in small areas that can be considered as points. One of the most popular tests in this field is QS-PST, which is used to determine the puncture resistance of sheet materials due to its similarity with ballistic results (Kawano et al. 1988; Longère and Dragon 2015). In addition, in recent years, experimental and numerical applications of QS-PST have been increasing in composite materials, which have replaced metals due to their light weight and high strength properties. (Ayten et al. 2020; Salman et al. 2018). Although the QS-PST looks similar to punching, which is a mechanical forming method, it is a different test method as it tests material resistance using different pitch-to-punch ratios (SPR) and different punch tip geometries (flat, conical, and pyramidal). In addition, this test gives a preview of how sheet metal materials will behave during the press-forming process. Sheet materials are commonly converted into products by printing-forming methods (Karajibani et al. 2017; Şener et al. 2020; Vatansever & Esener 2019). It is thought that the experimental and numerical application of QS-PST to the material will be beneficial in overcoming the production problems encountered in this process.

When the literature is examined, although there are similar studies, however neither numerical nor experimental application of QS-PST for stainless steels has been found. For this reason, even though this study is new in this field, it is thought that it will contribute to the literature. Thus, it was aimed to apply this method, which is frequently used in the testing of composite materials, to metal materials.

In this study, a non-standard QS-PST was applied to stainless steel sheet material experimentally and numerically, and the results were compared. Thus, the generated CAD model and system were verified. In order to determine the most accurate model, FEAs were repeated by reducing the mesh size and increasing the number of elements. It has been observed that when the number of elements is increased, the results of the FEAs approached to the experimental study results. Consequently, the importance of mesh size and number in numerical analysis has been demonstrated. This method is frequently used in the literature for the validation of numerical analysis models (Uçtu et al. 2017; Seyedzavvar et al. 2022). In addition, the same material was subjected to tensile tests with two different strain rates to identify the material in the library of the numerical analysis software.

2. METHOD

AISI-304 stainless steel (304 SS) sheet metal with a thickness of 0.5 mm was chosen as the test material. This material was cut with a liquid-cooled cutting device in suitable sizes for QS-PST with edge lengths of 100 x 100 mm thus, the workpiece was made ready for the test. 304 SS has 8.00 g/cm^{3}density, 193 GPa modulus of elasticity, 540 – 750 MPa tensile strength, and elongation 45 %. It also includes nearly 18 % chromium and 8 % nickel elements.

The QS-PST die consists of three parts, the lower die consists of two parts, and the punch is included as the third part. (Fig. 1). In this study, the punch tip geometry was selected as straight cylinder for both experimental and numerical investigations, and the span-to-punch ratio (SPR) ratio was specified as 2. Moreover, while the punch diameter is 13 mm, the gap diameter corresponds to 26 mm. This die was specially designed for the electromechanical tensile-compression tester, and is made of special hardened steel. Thus, it can resist to deflection and deformation.

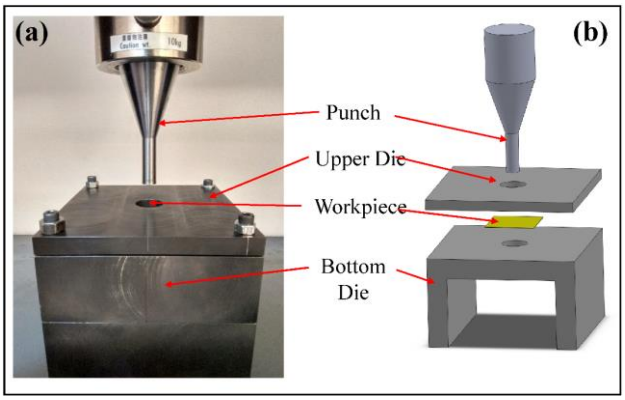

Figure 1. QS-PST system (a) experimental setup, (b) CAD model

In Fig. 1, the experimental setup and the CAD model of this setup can be seen. In order to shorten the solution time of FEA by reducing the number of meshes in the CAD model, the dimensions of the workpiece were reduced by 50% (to 50 x 50 mm).

As a method, first of all, the experimental setup was prepared and the QS-PST application was made. The prepared workpiece was firstly subjected to punch tests in the experimental setup. The feed rate of the punch was kept constant as 2 mm/d in all experiments

Later on, the CAD model of the material was prepared and made ready for numerical analysis. In order to investigate the plastic deformation three-dimensional FEAs were performed by using Deform 3D software. This software is widely preferred for numerical modeling of machining methods (Hasçelik and Aslantaş 2021). Also this software is frequently preferred in severe plastic deformation studies with its realistic results (Öğüt et al. 2021; Şahbaz et al. 2019). For this reason, it was chosen in this study as well. In all analyzes, the temperature was selected as 20 °C and the coefficient of friction was specified as 0.08 in shear mode. In addition, in order to make the behavior of the material more accurate and reliable in numerical analysis, the tensile tests were performed on the same material and it was identified as a new material in the material library of the FEA software.

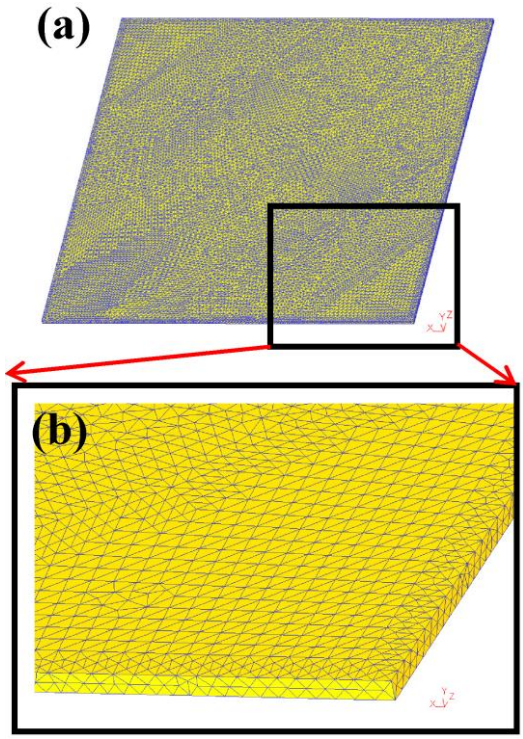

Figure 2. (a) Fine-mesh representation of the workpiece (b) detailed representation of the double-layer mesh

The mentioned tensile tests were repetitive, and tensile rates were adjusted to correspond to material strain rates of 0.25 sec^{-1} and 8 sec^{-1}. In the tensile tests, the length of the tensile specimen was at least 5 times larger than the width, taking into account the ASTM-E8 standards. The tensile tests applied to specimens with 70 mm gauge length, 12.5mm width, and 0,5mm thickness. Then, the prepared CAD model was defined to the FEA software and the finite element mesh structure of the workpiece was prepared. It is very important to determine the number of mesh as accurately as possible so that the results of the analysis give absolute accuracy and similarity with the experimental results. For this reason, without changing the geometry of the workpiece and other parameters, the number of mesh was gradually increased from 16700 to 151800, and 7 analyzes were performed. Finally, since the result of the analysis with the mesh number of 151800 is closest to the experimental result, it was decided that it would be more accurate to examine the outputs of this analysis in numerical results. Before the numerical analysis, the workpiece consists of a very fine finite element mesh as shown in Fig. 2 and consists of 151800 tetrahedral elements and 39433 nodes. In this type of deformation analysis, the tetrahedral mesh structure is preferred because it requires the least user interaction and supports adaptive mesh thinning, and accordingly gives more accurate results. The union of these small regions, called finite elements, is called a finite element mesh. Elements that make up the finite element network are connected to each other by nodes located on the edges of the elements (Emirler et al. 2019; Şahbaz et al. 2013; Şahbaz et al. 2016). In the numerical analysis, the punch speed was applied as 2 mm/d, same as the experiments.

3. RESULTS and DISCUSSION

As a result of this experimental study, it was observed how the sheet material was deformed by the QS-PST effect. In this process, the changes in the force according to the punch progress were recorded thanks to the software of the test device.

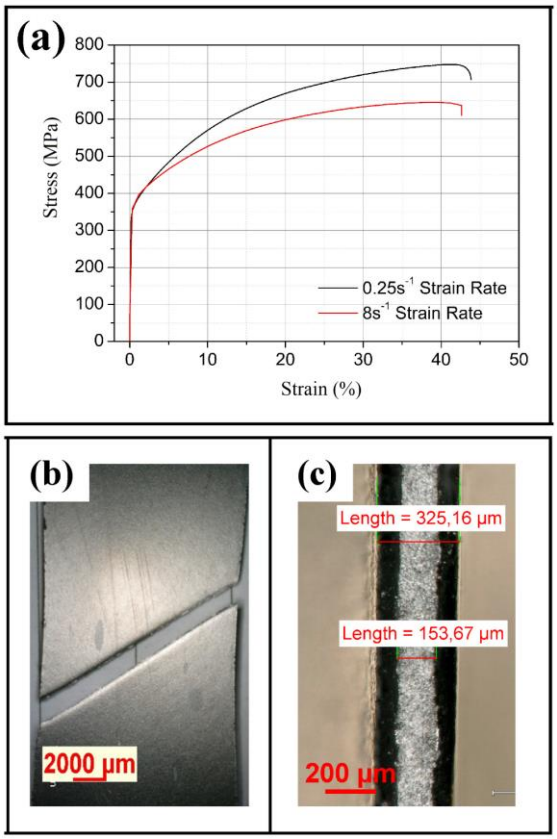

Figure 3. Tensile results at different speeds (a) Stress-Strain graph, (b) angular tensile fracture, (c) fracture surface

The shear stress was calculated by using the simple shear equation (τ=F/A) with the data obtained from this software. Here, 'τ' is the shear stress, its unit is MPa, 'F' is the total force on the punch, its unit is Newton, and 'A' is the area subjected to shear, which is the product of the circumference of the circle that the punch contacts with the material thickness, its unit is mm^2. For this study, since the punch circle circumference (πd) is 40.84 mm and the material thickness is 0.5 mm, the cutting area 'A' corresponds to 20.42mm^2.

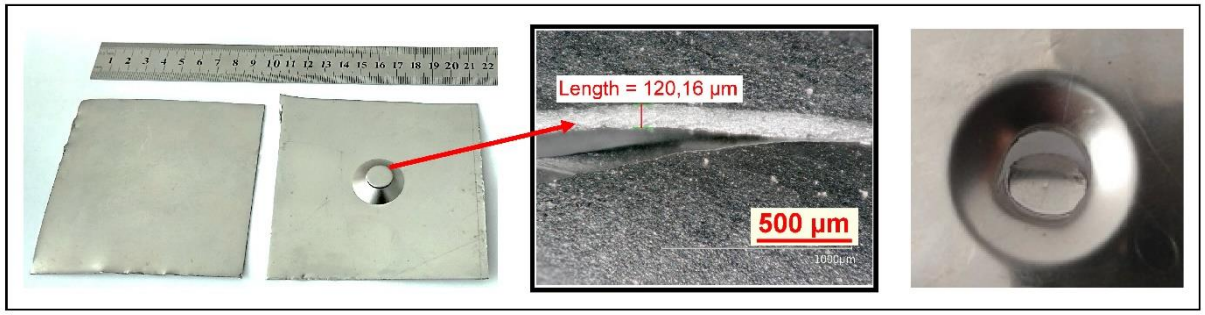

Figure 4. Material view before and after QS-PST

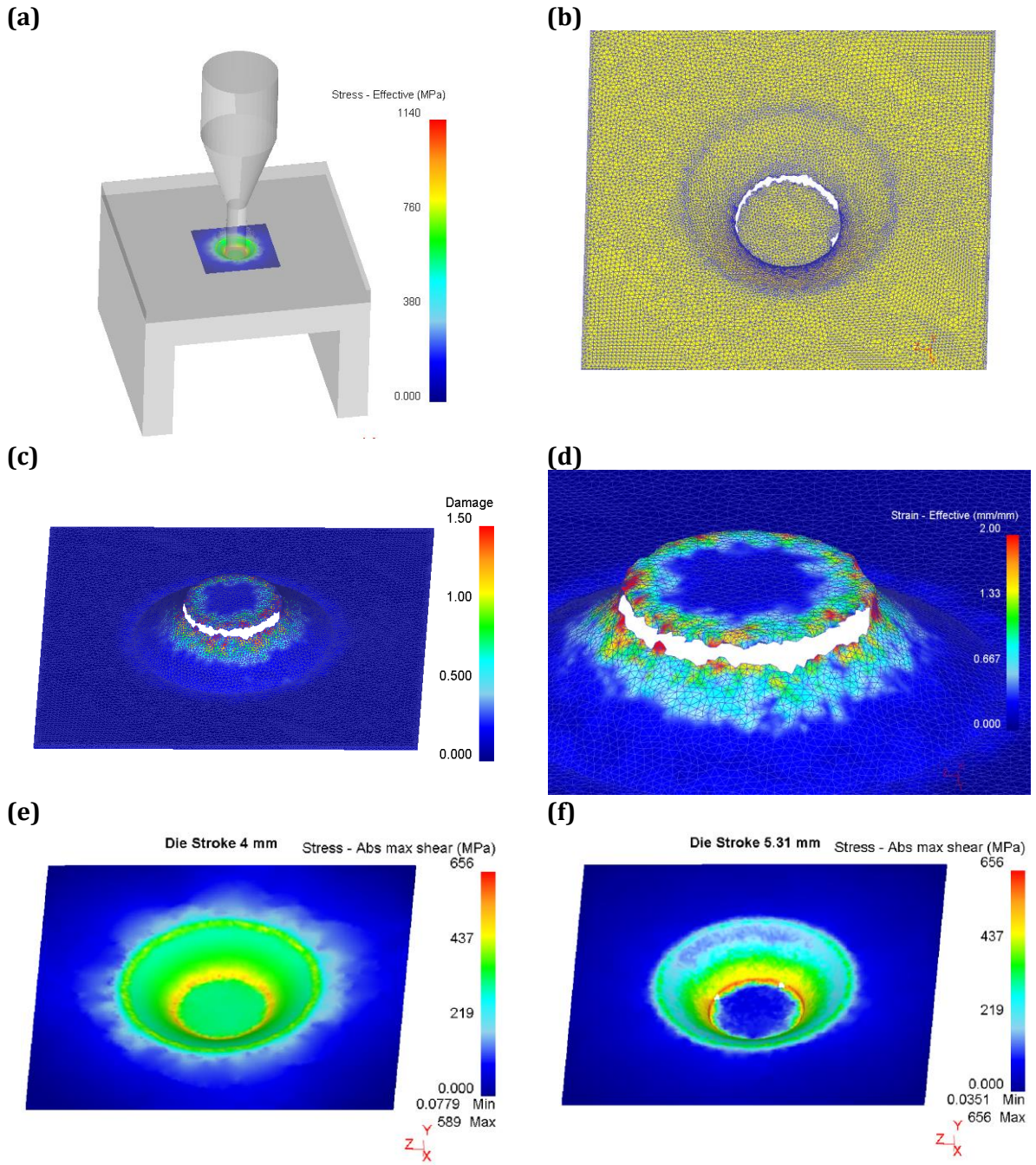

Figure 5. Numerical analysis result (a) test system, (b-e) workpiece stress, strain and damage results and views

Because of the material has a high formability feature, a high rate of deformation is observed until crack and separation formations as seen in figures (Fig. 3-4). In order to better analyze these properties, the tensile tests performed, and it was observed that the elongation of the material was around 45% (Fig. 3a). This result was confirmed by similar results in the literature review (Kaoumi & Liu 2018). In addition, it was observed that increasing the strain rate in the tensile test did not affect the deformation excessively, but decreased the maximum stress value (Fig. 3a). As a result of the tensile test, the material was broken with an angle from the planes with the maximum shear stress (Fig. 3b), the optical microscope view of the fractured surface and the measurement of the thickness decrease during fracture are shown in Fig. 3c.

Fig. 4 shows the workpiece before and after the experimental QS-PST, a close-up view of the deformation area and a microscope view of the separation surface. When the thinning rate of the surfaces after fracture was measured with the aid of a digital optical microscope, it was determined that the material thickness, which was 0.5 mm before the test, decreased to 0.15 mm (Fig. 3c) in the tensile test, and to 0.12 mm (Fig. 4) in the QS-PST result. This gives information about the ductility of the material. Further thinning of the material as a result of the QS-PST is due to the fact that the material is not only subjected to tension but also to compression during testing. Thus, the shear stress during the test increased to 550.6 MPa in analytical calculations given above (when the material thickness was kept constant), while as a result of this thinning, it increased to 656.0 MPa in the FEA (because the area 'A' became smaller).

During the analysis, the thickness of the material decreased due to the deformation, and the shear stress increased because the area on which the shear force was applied decreased. The FEA results are given below both visually (Fig. 5) and graphically (Fig. 6). In terms of comparison, when the experimental and numerical images after QS-PST are examined, the behavior and deformation areas of the material under loading show great similarity (Fig. 4-Fig. 5b).

In Fig. 5a, a numerical analysis image of the entire system after the test is given, while in Fig. 5b, the mesh structure of the workpiece after fracture is illustrated in detail. Thanks to the re-meshing feature pf the software during the FEA, the mesh size has been increased in areas with excessive stress by reducing the mesh structure. As a result of this, the results converged to the experimental results as more precise calculations were made. In Fig. 5c, the damage of the workpiece after breakage is shown, and the result with a value above 1 on the surfaces with separation confirms the analysis. In Fig. 5d, the effective strain results that occur in the workpiece during the test are shown. In Fig. 5e and Fig. 5f, the maximum shear stresses are given when the punch moves 4 mm and 5.31 mm (at the moment of fracture), respectively. As can be seen here, during the test, the maximum shear stress occurred around the surface where the punch contacts the workpiece, and as a result, separation occurred here.

When the numerical study results are compared with the experimental results, it is seen that there is a close similarity in both visual deformation and numerical results. The main reason for this is related to correctly defining the parameters such as friction, mesh structure, number of mesh and simulation steps during FEA. The effect of the number of mesh, which is one of the most important of these parameters, on the results has been examined in this study, and the force-deformation graph of the mesh number starting from 16700 to 151800 is given (Fig. 6a).

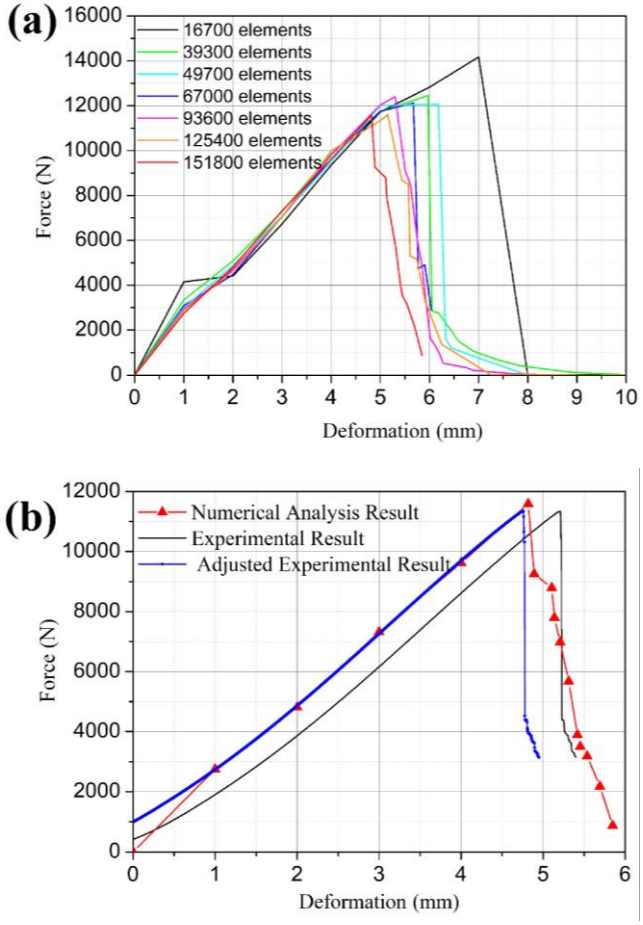

Figure 6. QS-PST Force-Strain graphs (a) numerical analysis result with different element numbers (b) numerical and experimental comparison

Then, these graphs were compared with the experimental force-shape change graph, this situation is shown in Fig. 6b and some values are also given as a table (Table 1).

It has been determined that the closest numerical solution to the experimental graph is the analysis with 151800 mesh, and in Fig. 6b it is given comparatively. As can be seen in the graph, the deformation caused by the stretching of the experimental workpiece is somewhat offset. This situation, which seems to be a shape change difference between experimental and numerical, has been resolved with the experimental adjusted graph. While generating the experimentally adjusted graph, the graph was shifted 45 mm to the left (in the strain axis) without changing the force values, and overlapped with the experimental. This is clearly seen from the values in Table 1.

As can be seen from Table 1, the values for maximum force (N) and maximum strain (mm) after QS-PST are given for all numerical analyses, experimental raw and adjusted experimental procedures. In the table, the numerical analysis results were compared with the

experimental (adjusted) results and it was seen that the smallest difference in both maximum force and maximum deformation was with the analysis with a mesh number of 151800.

Table 1. Comparison of Numerical Analysis results with experimental

Number of Elements	Max. Force (N)	Experimental Difference (%)	Maximum Deformation (mm)	Experimental (adjusted) Difference (%)
16700	14172.44	24.93	7.00	47.05
39300	12452.67	9.77	5.96	25.21
49700	12066.93	6.37	6.18	29.83
67000	12120.00	6.84	5.67	19.12
93600	12400.24	9.31	5.30	11.34
125400	11600.26	2.26	5.15	8.19
151800	11586.98	2.14	4.82	1.26
Experimental Raw	11343.99	0	5.21	9.45
Experimental Adjusted	11343.99	0	4.76	0

4. CONCLUSION

In this study, QS-PST was applied both experimentally and numerically for 304 SS then the results were compared. When the mesh size is thinned, a numerical model very close to the experiment is obtained. The same stainless steel sheet material and experimental setup used in the experiment were prepared for the numerical model. After that, a FEAs was carried out by assigning different mesh numbers to the workpiece. When the analysis with the highest number of meshes with 151800 elements is compared with the experimental results;

- A 2.14% difference in the maximum forces applied by the punch is detected,
- A 1.26% difference was observed in the maximum deformation of the material.

These very low differences are acceptable for numerical studies, and a model that is very close to reality has been obtained with this study. In future studies, this model can be examined on parameters such as material thickness, material layer number, punch-hole ratio.

In addition, as a result of the numerical analysis of this model, the damage, effective stress and effective strain values were examined and it was seen that the highest values were found in the parts of the material with tearing, as expected. This situation confirms each other with the optical microscope images, and it is seen that the thickness of this material, which has a very high ductility, decreased by about 4 times in the tear region and decreased to 0.12 mm.

ACKNOWLEDGEMENT

I would like to thank KMU Mechanical Engineering Department Head Prof. Dr. Uğur Köklü and his management team for the laboratory facilities. I would like to thank Dr. Ali İmran Ayten for mold supply and Dr. Bekir Güney and Teach. Asst. Hüseyin Kaya for material supply. I would like to thank the editors and referees for their contributions during the review and evaluation process of the article.

Conflicts of interest

The author declares no conflicts of interest.

REFERENCES

Al-Bakri A A, Sajuri Z, Ariffin A K, Razzaq M A & Fafmin M S (2016). Tensile and fracture behaviour of very thin 304 stainless steel sheet. Jurnal Teknologi, 78(6–9), 45–50. doi: 10.11113/jt.v78.9146

Aydın K & Karaağaç İ (2019). DP600 ve HSLA300 Sac Malzemelerde Geri Esneme Davranışlarına Proses Parametrelerinin Etkisinin Deneysel Araştırılması. Düzce Üniversitesi Bilim ve Teknoloji Dergisi, 7(3), 1456–1465. doi: 10.29130/dubited.532628

Ayten A İ, Ekici B & Taşdelen M A (2020). A numerical and experimental investigation on quasi-static punch shear test behavior of aramid/epoxy composites. Polymers and Polymer Composites, 28(6), 398–409. doi: 10.1177/0967391119881554

Çağdaş I U & Taşkın M (2020). A modified analytical expression to determine the quasi-static pre-indentation loads of metal-faced sandwich beams. Journal of Sandwich Structures & Materials, 22(5), 1404–1425. doi: 10.1177/1099636218785829

Çeliker S, Eşsiz E S & Oturakcı M (2021). Integrated AHP-FMEA risk assessment method to stainless tank production process. Turkish Journal of Engineering, 5(3), 118–122. doi:10.31127/TUJE.702369

Emirler B, Tolun M & Yıldız A (2019). Eğik Çekme Yükü Etkisindeki Tekil Kazığın Üç Boyutlu Sayısal Analizi. Çukurova University Journal of the Faculty of Engineering and Architecture 34(2), 219-229. doi: 10.21605/cukurovaummfd.609235

Hasçelik A & Aslantaş K (2021). Mikro tornalama işleminde kesme kuvveti katsayılarının mekanistik ve nümerik modelleme ile tespiti. Gazi Üniversitesi Mühendislik Mimarlık Fakültesi Dergisi.; 37(1): 235-246. doi:10.17341/gazimmfd.794462

Kaoumi D & Liu J (2018). Deformation induced martensitic transformation in 304 austenitic stainless steel: In-situ vs. ex-situ transmission electron microscopy characterization. Materials Science and Engineering A, 715, 73–82. doi: 10.1016/j.msea.2017.12.036

Karajibani E, Hashemi R & Sedighi M (2017). Forming limit diagram of aluminum-copper two-layer sheets: numerical simulations and experimental verifications. International Journal of Advanced Manufacturing Technology, 90(9–12), 2713–2722. doi: 10.1007/s00170-016-9585-1

Kawano S, Kaminishi K, Yamashita M & Shimizu S (1988). Energy-absorbing capacity of ductile thin metal sheet under quasi-statical penetration by conical punch. JSME Int J Ser 1, 31(1), 108–116. doi: 10.1299/jsmea1988.31.1_108

Köleoğlu Gürsoy Ö & Esener E (2019). Malzeme Modellerinin Sac Metal Sonlu Elemanlar Analizi Tahmin Performansına Etkisinin Değerlendirilmesi. Bilecik Şeyh Edebali Üniversitesi Fen Bilimleri Dergisi, 6(1). doi: 10.35193/bseufbd.549657

Longère P & Dragon A (2015). Dynamic vs. quasi-static shear failure of high strength metallic alloys: Experimental issues. Mechanics of Materials, 80(PB), 203–218. doi: 10.1016/j.mechmat.2014.05.001

Öğüt S, Kaya H, Kentli A & Uçar M (2021). Applying hybrid equal channel angular pressing (HECAP) to pure copper using optimized Exp.-ECAP die. International Journal of Advanced Manufacturing Technology, 116(11–12), 3859–3876. doi:10.1007/s00170-021-07717-9

Salman S D, Leman Z, Ishak M R, Sultan M T H & Cardona F (2018). Quasi-static penetration behavior of plain woven kenaf/aramid reinforced polyvinyl butyral hybrid laminates. Journal of Industrial Textiles, 47(7), 1427–1446. doi:10.1177/1528083717692593

Seyedzavvar M, Seyedzavvar M, Olıaeı S N B & Abbasi H (2022). Numerical simulation and experimental investigation: Metal spinning process of stepped thin-walled cylindrical workpiece. Turkish Journal of Engineering, 6(1), 67–80. doi:10.31127/TUJE.824890

Şahbaz M, Kentli A, Yilmaz M, Köten H & Yükselentürk Y (2013). Modeling and Thermal Analysis of High Power Led Armature. International Symposium on Computing in Science & Engineering. Proceedings, 164–168.

Şahbaz M, Öğüt S & Kentli A (2016). Cadde Tipi Led Armatürün Isı Yayıcısında SEY ve YSA Modeli Kullanılarak Sıcaklık Tahmini Yapılması. Marmara Fen Bilimleri Dergisi, 28(2). doi: 10.7240/mufbed.09519

Şahbaz M, Kaya H, Kentli A, Uçar M, Öğüt S & Özbeyaz K (2019). Analytical and Numerical Analysis Comparison of Equal Channel Angular Pressing for Al5083 Alloy. Advanced Science, Engineering and Medicine, 11(11), 1100–1103. doi:10.1166/asem.2019.2461

Şener B, Kılıçaslan E S & Firat M (2020). Modelling anisotropic behavior of AISI 304 stainless steel sheet using a fourth-order polynomial yield function. Procedia Manufacturing, 47, 1456–1461. Elsevier B.V. doi: 10.1016/j.promfg.2020.04.320

Türkoğlu T & Ay I (2021). Investigation of mechanical, kinetic and corrosion properties of borided AISI 304, AISI 420 and AISI 430. Surface Engineering. doi: 10.1080/02670844.2021.1884332

Uçtu Ö, Sevim İ, Karataş B & Şahin B (2017). Determination of optimum mesh size to measure tooth root stress of spur gear using finite element analysis. Turkish Journal of Engineering, 1(1), 37–43. doi:10.31127/TUJE.320047

Vatansever H & Esener E (2019). Sonlu Elemanlar Hesaplama Parametrelerinin Sac Metal Şekillendirme Simülasyon Süresi ve Hassasiyetine Etkisinin Tespiti. European Journal of Science and Technology, 16, 92-108 doi: 10.31590/ejosat.555491

Turkish Journal of Engineering
https://dergipark.org.tr/en/pub/tuje
e-ISSN 2587-1366

Determination of shear strength parameters of compacted high plasticity clay soils based on different laboratory tests

Burak Yilmaz*[1], Murat Türköz [1]

[1]*Eskisehir Osmangazi University, Engineering and Architecture Faculty, Department of Civil Engineering, Eskişehir, Turkey*

Keywords
Shear Strength
Shear box test
Unconfined compression test
Compaction

ABSTRACT

In civil engineering projects, soils are compacted to improve their engineering behavior and properties. Compacted soils are widely used in dams, embankments and road infrastructure. Compacted fine-grained soils, especially clay-containing soils, are frequently used as barriers to water and pollutant movement in landfills. Shear strength parameters of compacted high plasticity clay soils depend on many variables such as consistency limits, dry density, and degree of saturation. In this study, 20 high plasticity clay soil samples were used and geotechnical identification tests were performed on each of them. Direct shear box and unconfined compression tests were carried out to determine the shear strength parameters of the samples prepared by compression in their compaction characteristics. As a result of this study, the relationships between the geotechnical properties of soil samples and both the effective shear strength parameters and total shear stress parameters were evaluated.

1. INTRODUCTION

Compaction is one of the most important processes applied to improve soils during the construction of structures. The purpose of compaction is to improve the engineering properties of the soil mass. It is desired that the embankments used in the construction of structures such as highways, airports and embankment dams should be placed more firmly. This is achieved by reducing the air volume in the soil. Densification of soil by compaction depends on two factors, water content and compaction energy. The construction of earthen structures involves the use of compacted soils. In geotechnical problems such as bearing capacity, lateral soil pressure and slope stability, the shear strength parameters of compacted soils are primarily important. The shear strength parameters of compacted structural fills are usually measured using laboratory compacted samples. Wheeler and Sivakumar (1995) and Kong and Tan (2000) have studied the shear strength of unsaturated compacted soils.

Laboratory test methods have been developed to simulate the correct field conditions under the controlled conditions of the laboratory, and its main purpose is to accurately represent the mechanical behavior of the samples in the laboratory when exposed to the loads in the field (Yaghoubi et al. 2018). In order to understand the soil behavior after compaction in the field, it is necessary to determine the physical and engineering properties of the soil. Engineering tests to be carried out on samples prepared by compression in the laboratory environment on this basis provide important information on the behavior of fine-grained soils (Çalık and Sadağlı 2014). The performance of the compaction performed in the field is determined by comparing the compaction characteristics determined in the laboratory. Because laboratory compaction experiments are laborious and take a long time, many researchers have conducted research to determine the compaction characteristics depending on the physical properties of the soil. Çokça et al. (2004) examined the relationship between the strength parameters of the clayey sample and the water content in their laboratory study. As a result of this study, it has been shown that the cohesion value of the sample increases as it approaches the optimum water content, the cohesion value decreases at water contents above the optimum water content, and the internal friction angle decreases with increasing water content. Vondráčková et al. (2016) examined the parameters affecting cohesion in fine-grained soils. In this study, they stated that the saturation degree plays an important role on cohesion. Both Akgün et al. (2017) and Gençdal et al. (2018) evaluated the effect of increased water content on

* **Corresponding Author**
*(brkylmz186@gmail.com) ORCID ID 0000-0002-3708-766X
(mturkoz@ogu.edu.tr) ORCID ID 0000-0003-0241-113X

Cite this article
Yılmaz B & Türköz M (2022). Determination of shear strength parameters of compacted high plasticity clay soils based on different laboratory tests. Turkish Journal of Engineering, 6(4), 313-319

Research Article / DOI: 10.31127/tuje.1004043
Received: 03/10/2021; Accepted: 10/12/2021

strength. When evaluated in general, they stated that the soil strength decreased with increasing water content.

There are many experimental methods in the laboratory environment to examine the strength behavior of high plasticity clay soil to be used as a filling material under different loading conditions.

Ghosh (2012) conducted a series of veyn tests in the laboratory to examine the effect of water content on the shear strength of compacted clay soils. According to the results of the veyn test, it was determined that the increase in the water content caused a decrease in the undrained shear strength. VandenBerge et al. (2014) carried out consolidated undrained (CU) triaxial compressive tests on the soil they compacted with standard compaction in order to determine the undrained shear strength of the soil.

In this study, unconfined compression strength (UCS) and direct shear box (DSB) tests were conducted to determine the shear strength behavior of the specimens prepared by compression, and the relationships between the obtained strength parameters were investigated.

2. MATERIAL AND METHOD

2.1. Material

Soil samples excavated from the filling areas made in the same region but in very different locations were used. In order to determine the geotechnical properties of 20 different samples used in the experimental study, necessary classification experiments were carried out in the laboratory. In order to determine the compaction characteristics (optimum water content, OWC, and maximum dry density, MDD), the Standard Proctor test was carried out. Statistical evaluation of the geotechnical properties of the samples is given in Table 1. Fig. 1 shows the compaction curves of the samples, Fig. 2 shows the locations of the samples on the plasticity card, and Fig. 3 shows the distribution of the grain size in the samples.

When the identification test results are evaluated statistically, it is seen that the liquid limit (LL) values of 20 samples vary between 52% and 72% and the average value is 60%. Plasticity index (PI) values also vary between 25% and 39%, with an average value of 31.1%. Soil samples are fine-grained, and the fine-grain ratio is between 71.4% and 96.2%. The locations of 20 samples used in this study on the Casagrande Plasticity Card are shown in Fig. 2. As can be seen from this figure, all of the samples used in the experimental study are in the high plasticity clay (CH) class in the Unified Soil Classification System.

2.2. Method

Unconfined compression strength (UCS) and direct shear box (DSB) tests were carried out on the samples. During the engineering tests, ASTM D2166-00 and ASTM D3080/D3080M-11 standards were followed for the unconfined compression test and the shear box test, respectively.

Table 1. The statistical data of the geotechnical properties of the soil samples

Property	Num.	Value			
		Min.	Max.	Mean	Std. Deviation
Grain size					
<0.002 mm (%)	20	33.1	64.5	49.6	9.5
<0.075 mm (%)	20	71.4	96.2	89.1	6.6
<4.75 mm (%)	20	84.6	100.0	97.9	4.1
Atterberg limits					
LL (%)	20	52.0	72.0	60.0	5.3
PL (%)	20	25.0	36.0	28.9	2.6
PI (%)	20	25.0	39.0	31.1	3.9
Gs	20	2.73	2.81	2.77	0.002
Std. Proctor					
-MDD (Mg/m³)	20	1.421	1.616	1.537	0.046
- OWC (%)	20	21.6	29.4	24.4	2.0
-S (%)	20	78.6	89.8	83.9	3.5

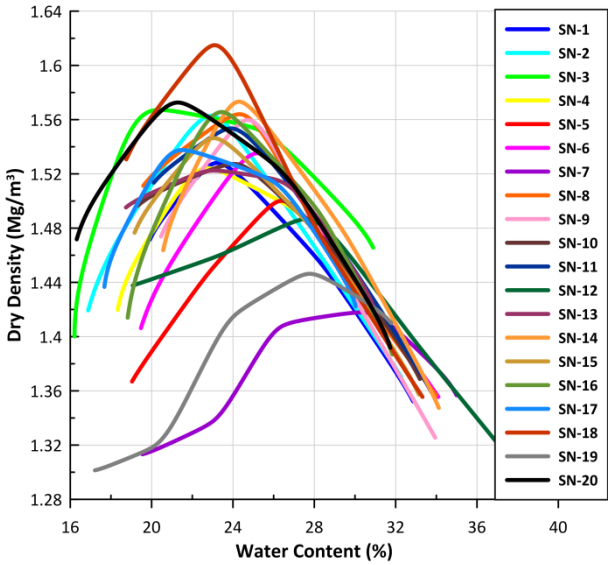

Figure 1. Compaction curves of the samples

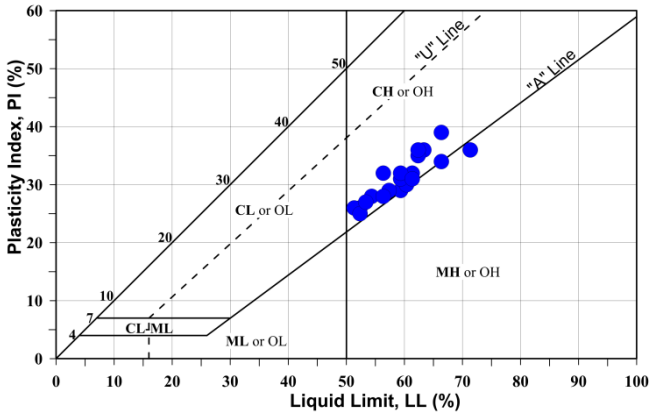

Figure 2. Location of the samples on the Casagrande Plasticity Card

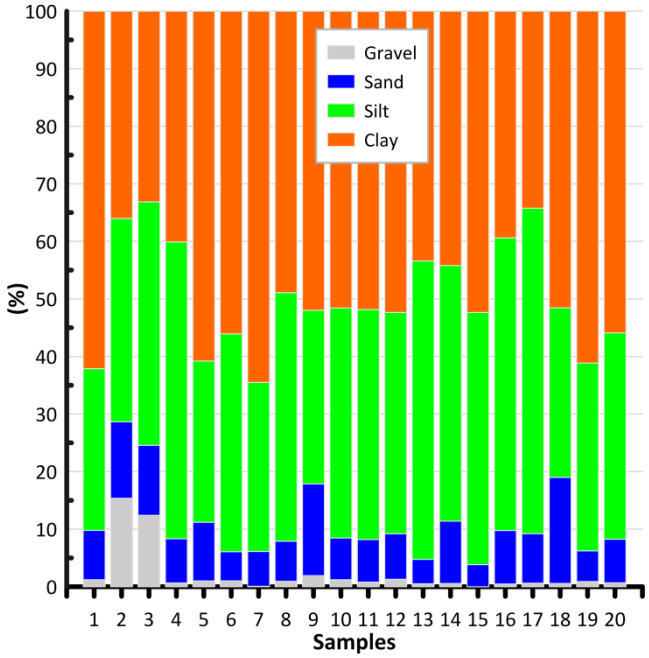

Figure 3. Grain size distributions of the soil samples

2.2.1. Preparation of samples

The disturbed samples were ground with a plastic-headed hammer and passed through a 4.75 mm mesh sieve. The amount of water needed to be added to bring it to the optimum water content was calculated and after adding the necessary water to the samples, they were packed in an air and watertight manner and waited for 24 hours to ensure a homogeneous distribution of the water in it. For the samples brought to the optimum water content, it was calculated how much sample should be compressed considering the dry density and mold volume. After the samples were compressed, they were wrapped in cling film in order to distribute the water in them homogeneously and kept in the desiccator for 24 hours.

All experiments within the scope of this study were carried out in the laboratory of Eskişehir Osmangazi University.

2.2.2. Unconfined compression strength test

UCS test is a widely used test because it gives very quick results. Although this test is performed in two ways as stress-controlled and deformation-controlled, the deformation-controlled method is commonly preferred. Since the drainage conditions of the sample were not controlled during the test, it is assumed that the undrained shear strength of the soil is obtained by rapid loading. In the test, the ratio of the sample length to the diameter is taken as 2, so that the loading head does not prevent the failure planes formed in the sample. UCS tests were performed on the samples prepared by compression in steel cylinders with a diameter of 50 mm and a height of 100 mm. In the experiment carried out under deformation control, the loading speed was chosen as 1 mm/min. The stress-strain relations of the samples were obtained and the unconfined compressive strength value at the time of collapse was obtained. Fig. 4 shows the unconfined pressure test equipment and shows the failure plane of the specimen after the test.

2.2.3. Direct shear test

The parameters found by the DSB test method are considered to be drained. For this reason, the cutting speed in the shear box should be selected at a speed that will not allow the formation of pore water pressure in the sample. Therefore, while the shear rate is high due to the high permeability of coarse-grained soils, the shear rate is quite slow in fine-grained soils due to low permeability.

The test was carried out under 3 different normal stresses, at a speed of 0.05 mm/min. After the sample was placed, the arm to which the normal stress would be transferred was placed on the sample. Distilled water was filled into the chamber and consolidation was initiated under the corresponding normal stress. After the sample had consolidated, shearing was performed at a speed of 0.05 mm/min. After the cutting process was carried out, the wet weight of the sample removed from the cutting box apparatus was taken and its dry weight was determined after it was kept in the oven for 24 hours. The experimental setup, the prepared sample and the post-test sample are shown in Fig. 5.

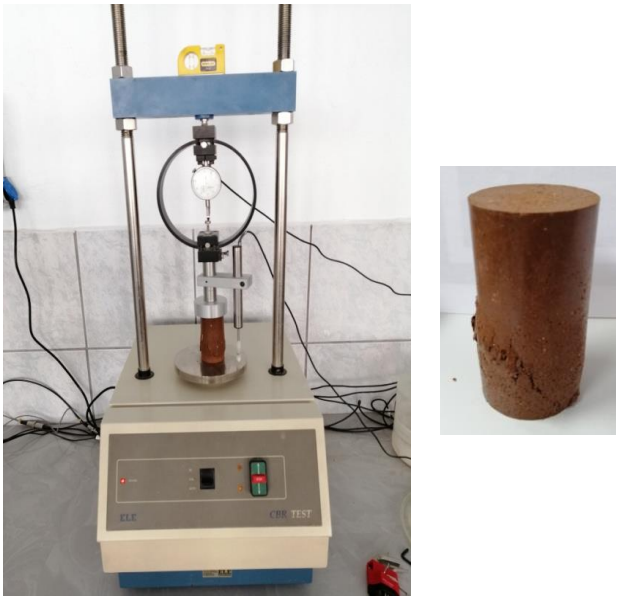

(a) (b)

Figure 4. (a)Unconfined compressive strength equipment, (b) Image of the sample after the test

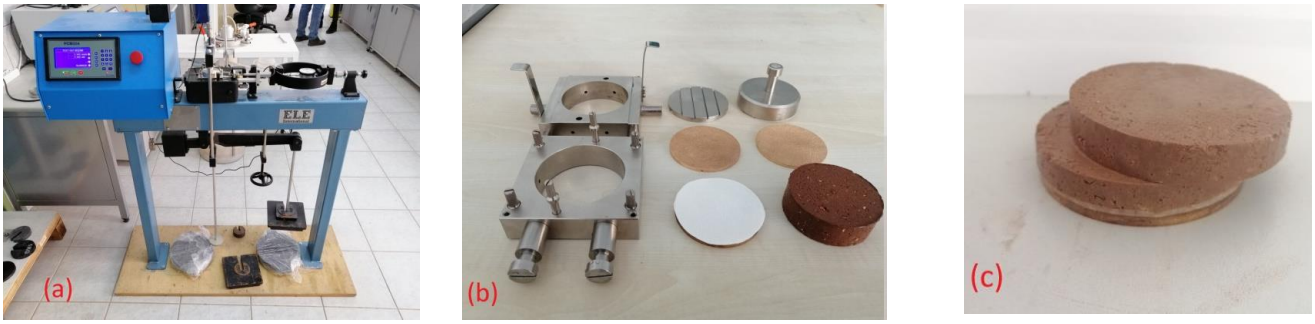

Figure 5. (a) Shear box assembly. (b) Compacted specimen, porous stones and cutting box apparatus. (c) Visual of the sample after the test

3. RESULTS AND DISCUSSION

The strength values at the time of failure (q_{un}) and axial deformation values were determined from the coordinates of the peak point in the stress-strain curves obtained as a result of the UCS experiments. In Figure 6, the stress-strain relations obtained as a result of the UCS test performed on samples 1 and 2 are presented as an example. Table 2 presents the q_{un} results for all samples. It was observed that the compressive strength of the samples was between 107 kPa and 250 kPa and the average value was 173 kPa. The axial strain values at the time of failure were also between 1.41% and 3.48%.

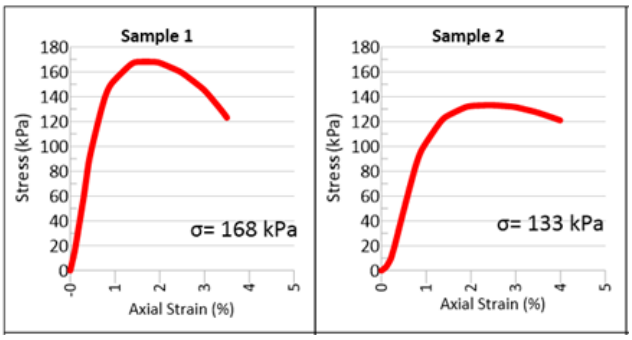

Figure 6. Stress-strain relations obtained as a result of unconfined compressive strength test for samples 1 and 2

Shear stress deformation curves obtained from DSB experiments were obtained for three different normal stresses. As an example, the curves obtained for samples 1 and 2 are presented in Fig. 7. As seen in Fig. 7, larger shear stress values were achieved with increasing normal stress values. Peak shear strengths were found from the peak of the curves. Residual shear strength values were also determined as the value at which the stress remained constant with increasing deformation. With the reduction of the grain size in clays, the specific surface increases, thus causing a decrease in residual strength.

Fig. 8 shows both the peak and residual strength envelopes for samples 1 and 2 as an example.

The shear strength parameters obtained from the engineering tests carried out within the scope of this study are presented in Table 2.

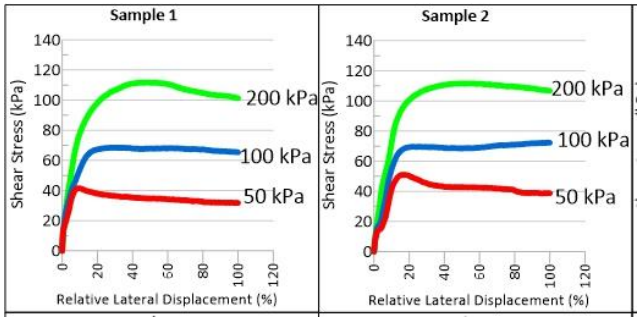

Figure 7. Stress-strain relations obtained as a result of direct shear box test for samples 1 and 2

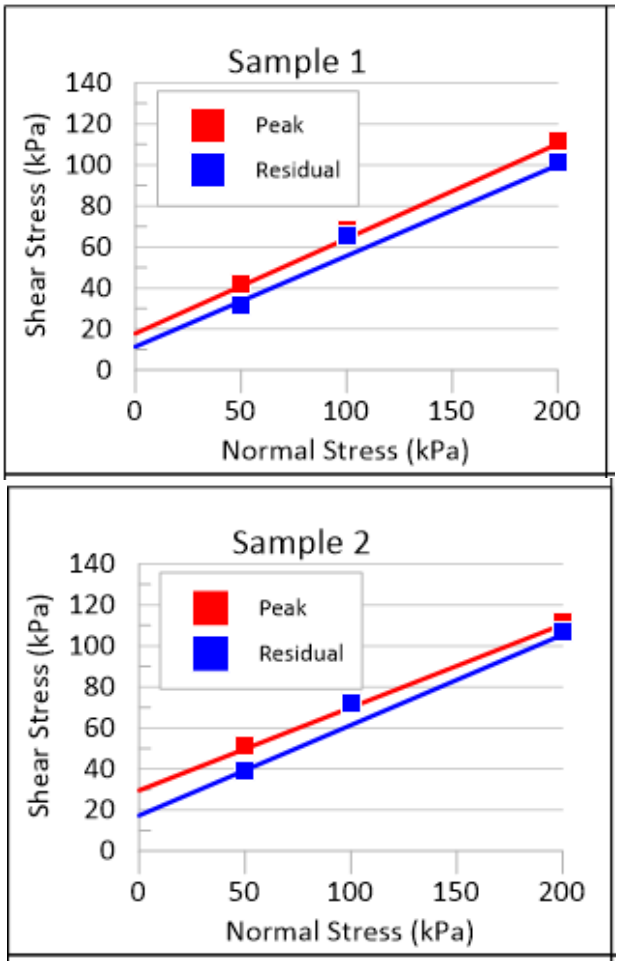

Figure 8. Failure envelopes for samples 1 and 2

The peak effective cohesion (c'_{peak}) and internal friction angle ($Ø'_{peak}$) values of the samples were in the range of 15.7-43.1 kPa and 15.7-27.3°, respectively. Residual effective cohesion (c'_{rez}) and internal friction angle ($Ø'_{rez}$) values, which are the residual strength parameters, also varied in the range of 4.5-17.7 kPa and 14.2-28.6°, respectively. The results showed that the residual cohesion strength values reached at large deformation levels were much lower than the peak strength values, especially when evaluated in terms of cohesion resistance, which is important on the strength of clay soils. Considering the cohesion and friction components, which are defined as shear strength parameters according to the Mohr Coulomb failure criterion, since the intergranular bonds are completely removed as a result of large deformations, when the permanent state is reached, even in high plasticity clays, there is no cohesion effect or takes very low values. Therefore, it has been shown by many researchers that the permanent shear strength is only due to intergranular friction (Skempton 1964; Mesri and Shahien 2003).

When a general statistical evaluation was made, no significant relations could be reached between the consistency limits and strength parameters. Although there was a tendency to decrease in strength with the increase of the consistency limits, a significant scattering was observed in the data. It can be said that the main factor controlling the shear strength is the mineralogical structure of the soil grains. Although all samples are classified as high plasticity clay, the variability of the clay mineral types they contain may be a factor in this situation.

The obtained relationships are presented in Figures 9, 10 and 11. As seen in Fig. 9, it has been determined that optimum water content (w_{opt}) has a negative correlation and maximum dry density (q_{dmax}) value has a positive correlation on q_{un}. In Fig. 10, the effect of w_{opt} and degree of saturation (S) on the peak shear strength parameters obtained from the shear box test results is shown. There was a negative correlation between the w_{opt} and the effective peak internal friction angle, while a positive correlation was observed between the S and the effective peak cohesion values.

Table 2. Strength parameters obtained from UCS and DSB test results

SN	q_{un} (kPa)	c'_{peak} (kPa)	$Ø'_{peak}$ (°)	c'_{rez} (kPa)	$Ø'_{rez}$ (°)
1	168	17.88	24.8	11.42	23.88
2	133	29.59	22.0	17.34	23.78
3	236	26.13	25.3	12.43	25.47
4	189	17.06	24.7	6.57	23.94
5	123	26.63	20.1	14.74	19.45
6	171	43.12	15.7	17.67	18.36
7	107	25.36	20.5	16.30	19.29
8	160	30.19	21.1	13.76	22.84
9	133	27.83	25.5	9.68	28.62
10	148	19.92	25.4	9.39	26.33
11	170	24.87	23.3	7.79	25.53
12	139	32.99	17.7	14.85	16.71
13	193	33.53	21.3	13.90	23.97
14	199	40.19	22.0	16.61	23.74
15	235	27.92	23.5	11.41	23.41
16	194	32.91	21.5	14.86	22.74
17	210	18.34	23.0	6.53	23.71
18	166	29.19	19.6	9.97	21.31
19	134	15.72	15.9	7.36	14.15
20	250	17.76	27.3	4.46	28.26

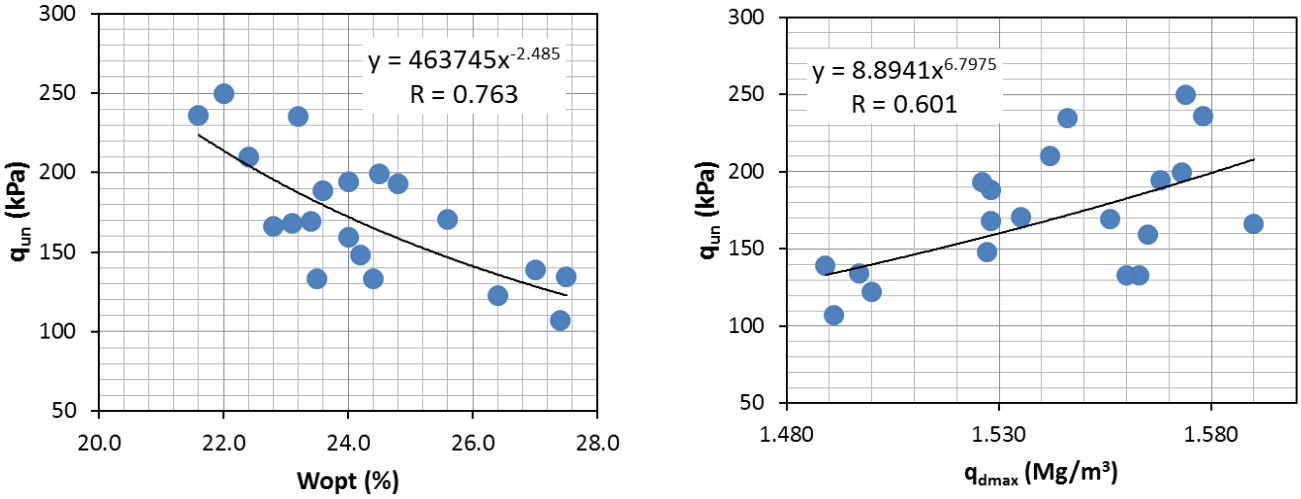

Figure 9. Relationships between unconfined compressive strength and compaction characteristics

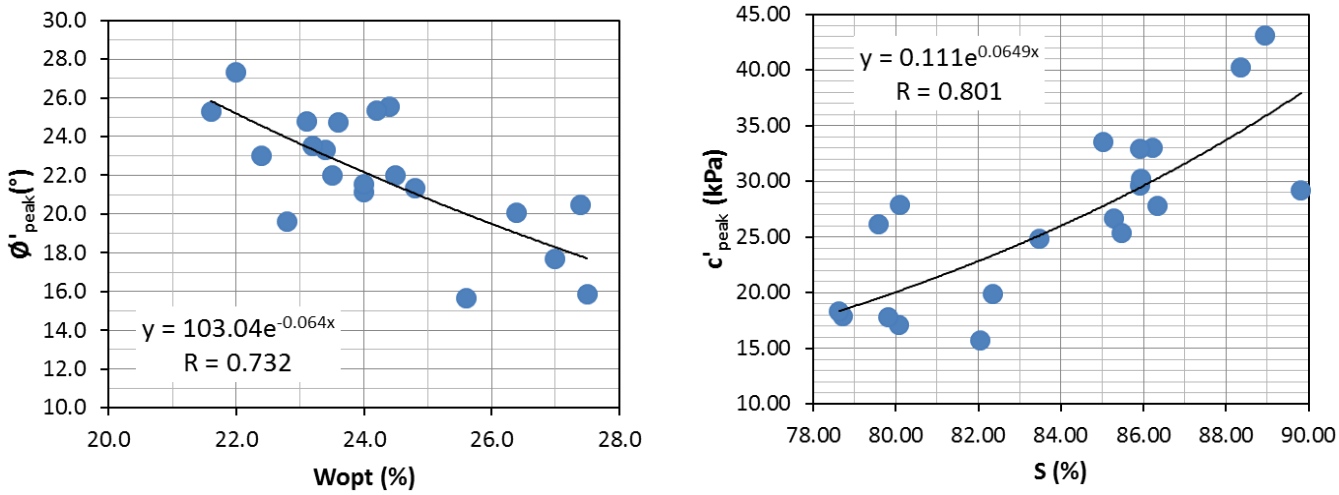

Figure 10. Relationships between effective peak strength parameters and, w_{opt} and S

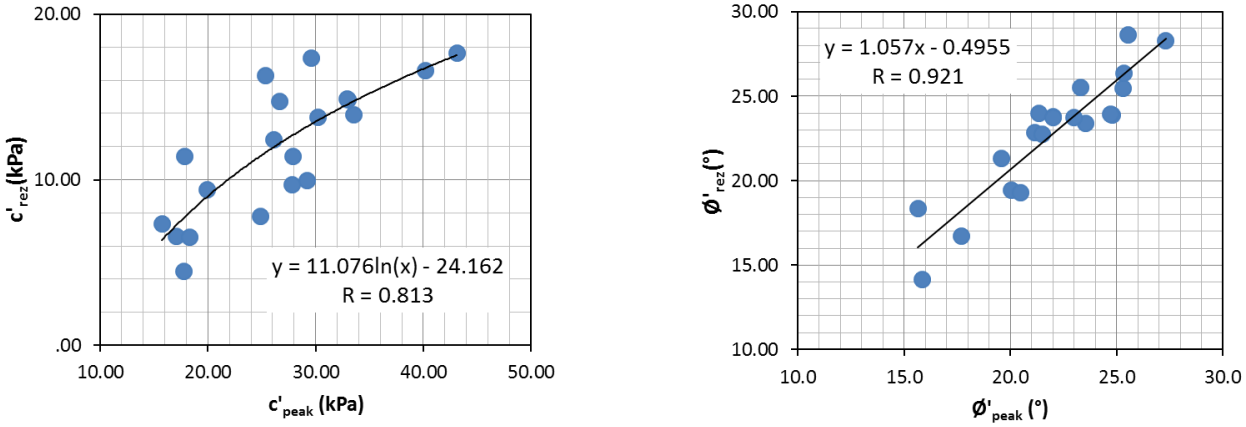

Figure 11. Relationships between effective peak and residual strength parameters

In Figure 11, the relationships between the peak and residual strength parameters found as a result of the shear box test are presented. It has been determined that the relations between the peak and residual strength parameters are at a very significant level. It has been seen that by using these relations, it is possible to approximate the strength parameters on the basis of effective and total stress.

4. CONCLUSION

In this study, shear strength parameters of compressed high plasticity clay soils were determined on the basis of both effective stress and total stress. The relationships between the geotechnical properties of the soil samples and the strength parameters were investigated. It has been observed that compaction characteristics are more important than other physical properties of soil samples on unconfined compressive strength. Although the geotechnical properties of the soil samples are quite close to each other, differences were determined between the strength parameters. For this reason, it should be noted that it will be necessary to evaluate the chemical and mineralogical properties of the samples in future studies.

ACKNOWLEDGEMENT

This study includes a part of the master's thesis of the 1st author, continuing at Eskişehir Osmangazi University, Institute of Science and Technology. The study was supported by Eskişehir Osmangazi University Scientific Research Projects Coordination Unit within the scope of the project numbered FYL-2021-1569.

Author contributions

Burak Yılmaz: Investigation, Experimental, Writing. **Murat Türköz:** Conceptualization, Design, Reviewing and Editing.

Conflicts of interest

The authors declare no conflicts of interest.

REFERENCES

ASTM D 2166-00 (2000). Standard Test Method for Unconfined Compressive Strength of Cohesive Soil, American Society for Testing and Materials, West Conshohocken, Pennsylvania, USA.

ASTM D 3080, D3080M-11 (2011). Standard Test Method for Direct Shear Test of Soils Under Consolidated Drained Conditions, American

Society for Testing and Materials, West Conshohocken, Pennsylvania, USA.

Akgün H, Türkmenoğlu A G, Kelam A A, Yousefi-Bavil K, Öner G & Koçkar M K (2017). Assessment of the efect of mineralogy on the geotechnical parameters of clayey soils: A case study for The Orta County, Çankırı, Turkey. Applied Clay Science, 164, 44-53.

Calik U & Sadoglu E (2014). Engineering properties of expansive clayey soil stabilized with lime and perlite. Geomechanics and Engineering, 6(4), 403-418.

Cokça E, Erol O & Armangil F (2004). Effects of compaction moisture content on the shear strength of an unsaturated clay. Geotechnical and Geological Engineering, 22, 285–297.

Gençdal H B, Berilgen S A & Kiliç H (2018). Sıkıştırılmış kil dolgu zeminlerin kayma mukavemeti parametrelerinin belirlenmesi. Zemin Mekaniği ve Geoteknik Mühendisliği 17. Ulusal Konferansı. 26-28 Eylül, İstanbul.

Ghosh R (2012). Effect of soil moisture in the analysis of undrained shear strength of compacted clayey soil. Department of Construction Engineering, Jadavpur University, Kolkata, India, 10 December.

Kong L W & Tan L R (2000). Study on shear strength and swelling-shrinkage characteristic of compacted expansive soil. Unsaturated Soils for Asia, Rahardjo, Toll and Leong (eds.), Balkema, Rotterdam, 515-519.

Mesri G & Shahien M (2003). Residual shear strength mobilized in first time slope failures. Journal of Geotechnical and Geoenvironmental Engineering, 129 (1), 12-31.

Skempton A W (1964). Long-term stability of clay slopes. Geotechnique, 14 (2), 75-101.

VandenBerge D R, Brandon T L & Duncan J M (2014). Triaxial Tests on Compacted Clays for Consolidated Undrained Conditions. Geotechnical Testing Journal, 37(4).

Vondráčková T, Kmec J, Čejka J, Bartuška L & Stopka O (2016). Evaluation of the parameters affecting the cohesion of fine grained soil. World Multidisciplinary Earth Sciences Symposium (WMESS 2016). IOP Conf. Series: Earth and Environmental Science 44.

Yaghoubi E, Disfani M M, Arulrajah A & Kodikara J (2018). Impact of compaction method on mechanical characteristics of unbound granular recycled materials. Road Materials and Pavement Design, 19(4), 912-934.

Wheeler S J & Sivakumar V (1995). An elasto-plastic critical state framework for unsaturated soil. Geotechnique, 45(1), 35-53.

Turkish Journal of Engineering
https://dergipark.org.tr/en/pub/tuje
e-ISSN 2587-1366

Image processing-based realization of servo motor control on a Cartesian Robot with Rexroth PLC

Fatma Kuncan[*1], **Sıtkı Öztürk** [2], **Fatihhan Keleş** [2]

[1]*Siirt University, Faculty of Engineering, Department of Computer Engineering, Siirt, Turkey*
[2]*Kocaeli University, Faculty of Engineering, Department of Electronics and Communication Engineering, Kocaeli, Turkey*

Keywords
Image Processing
Servo Motor Control
Cartesian Robot
Rexroth PLC

ABSTRACT

The aim of this study was to separate the objects, whose position was determined using Rexroth PLC on a workbench, and bring them to different locations. Position control of synchronous motors with PLC was done with coordinates obtained by image processing. A real-time Gantry robot was set up for the study. An image taken with the camera connected to Gantry robot is transferred to the Matlab environment. The coordinate data obtained by processing the image are separated for the coordinates used, and the position control of the motors is provided. First, the image was changed to grayscale to apply image processing methods. Then, with the image processing formula, 'viscircles' has been applied to mark the detected circles. The obtained coordinates were transferred to IndraWorks PLC to be used in the portal robot. Objects in the determined coordinates were moved to another coordinate with the help of the pneumatic system that integrated to Gantry Robot. The system has been tested for different conditions. As a result of studies, it has been observed that both the image processing method and the system work simultaneously with high accuracy. It is thought that the study can be used in many areas in the literature.

1. INTRODUCTION

In the technology movement that progresses with time and continues to accelerate, it is a necessity to solve the problems with fast and sharp methods. This requirement has played a major role in the transition of people to robotic systems, and we see that many industrial factories produce by using robots in their systems in this area. It has become essential that these systems should become widespread not only in the industrial sector but also in every stage of life such as education, health, military, and economy. In recent years, researchers have widely used robot, autonomous and image processing studies (Bakır et al. 2012; Çubukçu et al. 2015; Köse et al. 2019). One of the most important reasons for this increase is the transition to automation systems instead of people. Both researchers and industrial (industrial) practitioners have turned to automation and robotics in recent years (Horoz et al. 2013; Jose and Udupa 2021; Hu et al. 2021). This study, on the other hand, is a study of an autonomous system in which servo motors, one of the cornerstones of industrial motion, are controlled by PLCs. The applications made during the project process firstly start in the software part. The image taken with the camera is first processed in the MATLAB software program. Our goal is, find the coordinates of objects on a gantry robot workbench. In this study, the image processing functions of the 'Image Processing Toolbox' application are applied to the image. After the pixel coordinates are processed with functions containing the obtained image synchronization parameters, coordinate information in 'mm' unit is obtained. Obtained coordinates are writed to data sequences in PLC. With many components such as variables, buttons, timers defined in the PLC program, movement is provided with logic operations in the program blocks. After the motion is provided, the necessary program blocks for system automation are written. Pneumatic piston is used to control movement in z-axis. It is aimed to move the objects in the obtained coordinates to other coordinates with this pneumatic system. After the pneumatic system is activated, the autonomy is checked and the results are shared. The PLC used on the system belongs to Bosch-Rexroth. The software of the study was IndraWorks software published by Bosch-Rexroth Company for PLC.

* **Corresponding Author**

*(fatmakuncan@siirt.edu.tr) ORCID ID 0000-0003-0712-6426
(sozturk@kocaeli.edu.tr) ORCID ID 0000-0003-3804-5581
(fatihkeles.41@gmail.com) ORCID ID 0000-0002-6375-5553

Cite this article

Kuncan F, Öztürk S & Keleş F (2022). Image processing-based realization of servo motor control on a Cartesian Robot with Rexroth PLC. Turkish Journal of Engineering, 6(4), 320-326

Research Article / DOI: 10.31127/tuje.1004169

Received: 04/10/2021; Accepted: 20/11/2021

2. SYSTEM COMPONENTS

The Block Structure of the realized gantry robot is given in Figure 1. In this work, basically 3 main components were used to make the system the desired one. These are Servo motor, PLC, and Image Processing, respectively. First of all, these 3 components are explained in the article, then the general operation of the system will be discussed.

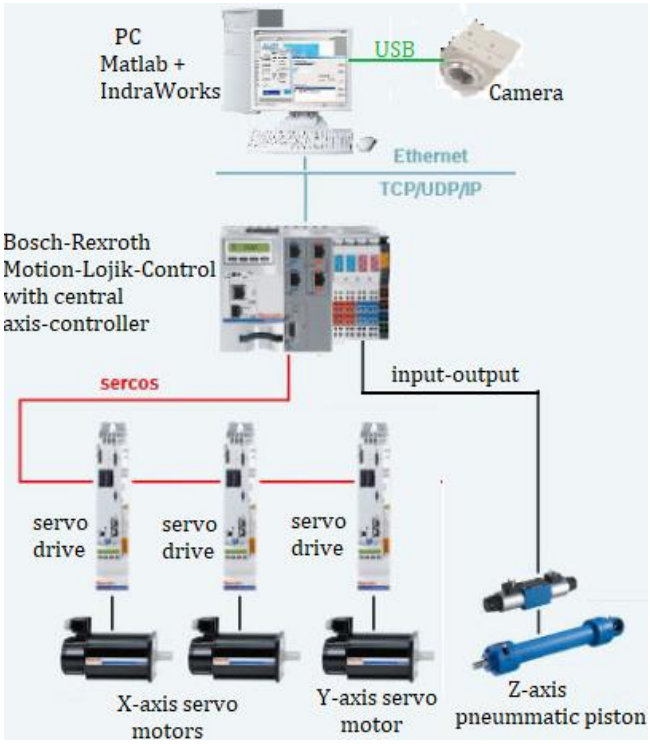

Figure 1. Block structure of the realized gantry robot

2.1. Servo Motor

Servo motors contain a DC motor that drives the motor. Apart from this motor, there is a gear mechanism, a potentiometer, and a motor driver circuit. The potentiometer measures the amount of rotation of the motor shaft. As the DC motor in the servo moves, the potentiometer rotates and the control circuit compares the position of the motor with the desired position and drives the motor. The servo motors used in the portal robot bench are shown in Figure 2.

2.2. PLC

PLC receives analog and digital information from the sensors or input devices it is connected to. The program written for the control of these data outputs is run and new output values are obtained based on the pre-programmed parameters. The output ports of the PLC are updated to control the system with the obtained analog and digital output values. This study generally constitutes the working principle of PLC. Briefly, a PLC first writes the data on the input port to the input data memory. Then the program written to control the system is run. Finally, analog and digital values in the output data memory are written to the output port. This cycle of the PLC starts when the PLC is RUN and continues its operation by repeating the cycle until it stops.

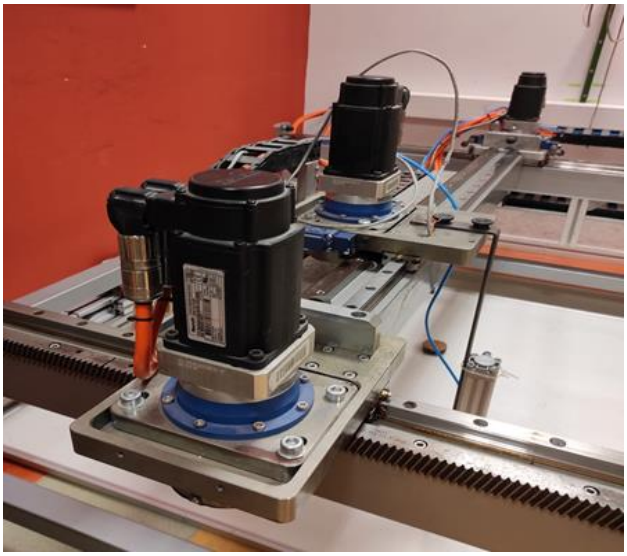

Figure 2. Servo motors used in gantry robot workbench

In this study, the control of the system and real-time operation are carried out by PLC to make the results obtained by the image processing method by the Matlab software. To carry out these operations, the necessary software work for the PLC must be done. The software made is written in the 'Drive Control' section, which is the sub-tab of the POU. This is where code diagrams are written through networks. These software studies have been carried out as the program progresses autonomously. For the motors to reach the desired position, all parameters must be defined in the PLC block.

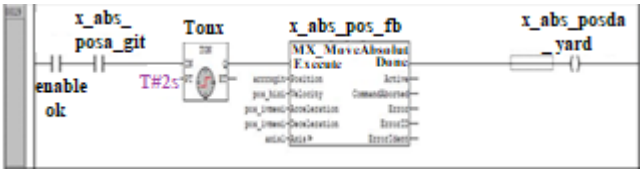

Figure 3. Defining the coordinates to the motion block

To access the detected objects, the x and y coordinates of the object must be pulled from the array sequentially. An 'i' variable is defined for this action. Objects are accessed sequentially with a for loop connected to the variable 'i'.

Figure 4. Go to the first coordinate

Figure 5. PLC block diagram

2.3 Image Processing

In recent years, image processing studies have been widely used in many different fields (Priyanto et al. 2015; Senthilkumaran et al. 2016; Vishesh et al. 2017; Banafian et al. 2021). In this study, an image processing application was carried out on the Gantry Robot mechanism. With the 'Image Processing Toolbox' it contains, MATLAB has enabled the 'Image Processing' technique used in today's technology to be used very quickly and effectively. It is widely used in fields such as military, medicine, security systems, industrial systems, astronomy. In this study, the image was processed with the MATLAB software applied on the image that we took from the "uEye industrial type camera" produced by IDS Company and it was desired to obtain the necessary data that we would use on the PLC. The camera we used is shown below.

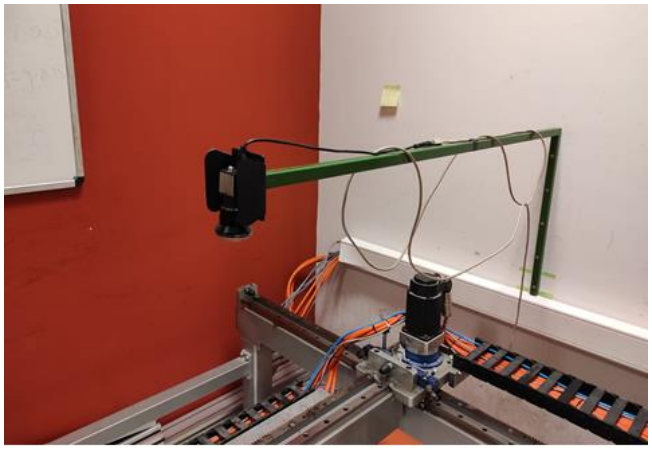

Figure 6. Image Processing Setup

In the image processing stage of the study, work is carried out on pixels. However, since the coordinate values we want to find are real-time, it is necessary to establish the pixel & distance relationship between them. Our goal is to access the variable values that create this difference between them. First, the image is taken from the camera. Thus, it is aimed to reach the information according to which dimensions an image is taken from the camera should be synchronized. It looks like below.

Figure 7. The maximum viewing angle of the image that can be taken with a camera

Next, the information we need to know is where the maximum and minimum points of the servo motors we control with PLC are. After obtaining the information about where these points are, images of the points are taken and a note is taken to which pixel values they correspond to. In Figure 7, the maximum and minimum points are marked.

Figure 8. Regions corresponding to Min (0,0) and Max (10000000,10000000) points in the Cartesian system.

After the corresponding points are found, the Eq. (1) is used.

$$f(x) = m(x - X_i)$$
$$f(y) = m(y - Y_i) \quad (1)$$

To solve these equations, we first define the f(x) and f(y) values to be 1000000, which is the maximum value reached by the servos.

Next, define the Xi and Yi values to the pixel values corresponding to the minimum points reached by the servos.

Figure 9. Pixel values corresponding to the point (0,0) used on the machine are shown

As seen in Figure 8, the pixels corresponding to the minimum points obtained in the Cartesian plane are 257 for Xi value, For the Yi value, it is found as 137. The pixel

locations obtained by moving the servos to any desired point are assigned to the x and y values. The values are assigned, the Eq. (2) is checked. As a result of the check, the following equation is obtained.

$$f(x) = 14836.79(x - 257)$$
$$f(y) = 14136.91(y - 137) \quad (2)$$

With Eq. (2), it is aimed to reach the information of which coordinates the image taken by the cameras should reach in 'mm'. In these processes, the system was sent to random points and the results were tested. At the end of the results, it was obtained that the camera was synchronous.

First of all, the image taken from the camera is taken on MATLAB with the 'imread' command. The captured image is in RGB (Red-Green-Blue) color space. To facilitate image processing, the image should be converted to gray color space. If the image is not converted to the gray color space, separate operations will not have performed on the three-color domains. This causes processing to slow down. In the figures below, the image is in its original state and converted to gray color space on MATLAB.

In the continuation of the operations, the 'imfindcircles' function included in the 'Image Processing Toolbox' application of MATLAB is used. The 'imfindcircles' function is a function that finds the circular objects in the image between the entered radius values by applying Hough Transform. With the 'Edge Detection' algorithm, it has been tried to detect the edges of the objects in the image. Each pixel is searched for a circle that can be created at the coordinates of the accumulator array mentioned above. If the operation is positive, it calculates the center and radius of the circle. All the circular objects created are specified as the largest shape rounds in the Hough Transform space with the accumulator sequence. At the output of the operations, the x, y coordinates, and radii of the circles are obtained. The received coordinate data is transferred to a matrix called 'center', which has the number of rows to which the number of rounds received and the number of two columns depend. Radius information, which is another information received, is transferred to an array named 'radicap' whose element number depends on the number of circles. In the figure below, the values rounded to integers with the 'round' operation are divided into different matrices one by one. Its purpose is to obtain the coordinates as a result of multiplying each coordinate with separate parameters during synchronization. The following image shows the relevant code block.

In the rest of the software, the 'viscircles' function was applied. The purpose of this function is to draw circles with certain centers and radius specified above, according to the entered values to determine which ones are on the image. The synchronization of the camera has been done in the above-mentioned topic. To apply the synchronization application function, the 'x' and 'y' values of the received coordinates were separated from each other and assigned to other variables. Immediately after, the synchronization process was applied to the variables and real-time coordinates were obtained and defined to "Koor1..N" variables (Kuncan et al. 2016; Kuncan and Kaplan 2016; Şengül et al. 2020; Alekseevic 2020; Belgacem et al. 2020).

Figure 10. The maximum viewing angle of the image that can be taken with a camera

Figure 11. The maximum viewing angle of the image that can be taken with a camera

```
10 -    m=14836,79;n=14136,91;x=0;y=0;
11 -    A1X=round(merkez(1,:));
12 -    A2X=round(merkez(2,:));
13 -    A3X=round(merkez(3,:));
14 -    A4X=round(merkez(4,:));
15 -    A5X=round(merkez(5,:));
```

Figure 12. The process of assigning 'round' coordinate values rounded to integers with synchronization parameters

```
17 -    a1=A1X(1,1);
18 -    b1=A1X(1,2);
19 -    A11=m*(a1-257);
20 -    B11=n*(b1-137);
21 -    Koor1=[A11 B11];
22 -    a2=A2X(1,1);
23 -    b2=A2X(1,2);
24 -    A22=m*(a2-257);
25 -    B22=n*(b2-137);
26 -    Koor2=[A22 B22];
27 -    a3=A3X(1,1);
28 -    b3=A3X(1,2);
29 -    A33=m*(a3-257);
30 -    B33=n*(b3-137);
31 -    Koor3=[A33 B33];
32 -    a4=A4X(1,1);
33 -    b4=A4X(1,2);
34 -    A44=m*(a4-257);
35 -    B44=n*(b4-137);
36 -    Koor4=[A44 B44];
37 -    a5=A5X(1,1);
38 -    b5=A5X(1,2);
39 -    A55=m*(a5-257);
40 -    B55=n*(b5-137);
41 -    Koor5=[A55 B55];
```

Figure 13. Applying the synchronization function to pixel coordinates and moving to real-time coordinates

Koor1	[3887032 2954424]
Koor2	[2596300 8114064]
Koor3	[5444812 8057520]
Koor4	[5726696 6431880]
Koor5	[7581196 8877408]

Figure 14. Obtained real-time coordinates

3. REAL-TIME OPERATION OF THE SYSTEM

At this stage of the study, the real-time operation of the system is explained. In the first part of this study, there is the stage of determining the coordinates of the objects with the proposed image processing method. In the second stage of the system, the coordinate values determined by image processing should be transmitted via software. According to the information received in the third stage, the servo motors have to perform the movement process correctly in the Gantry Robot system. As the last stage, there is the process of leaving the determined object to the determined place with the pneumatic equipment. Simultaneous transmission of all these stages is done via PLC. With the implementation of the autonomous system that has been built, the expected action is to transport the objects in the reached coordinates to different points on the Cartesian plane with a pneumatic system. For this action, there is a piston at the end of the servo moving on the 'y' axis. The task of this piston is to lift the object with the pneumatic system when the coordinate is reached and to leave it in place when the determined coordinate is reached.

The flowchart in Figure 15 consists of 4 separate columns. These columns represent 4 main operations.

The first column of the flow chart includes the description of the image processing phase. In this phase image will be taken by the camera and various functions will be applied to get the centers and coordinates.

The second column also shows that the coordinates obtained from image processing are assigned to the necessary sequences in the PLC. Movements of the servo motors that are controlled by PLC will be checked by 'DONE' bits to move synchronized as real-time coordinates given by it. If the synchronization process is successful, the transition to the next phase is achieved.

The third column of the chart includes the process of reaching the objects and lifting them with a vacuum and delivering them to the assembly coordinate.

The final column starts with the condition. The condition represents the final movement of the third column. If the last object has been lifted and delivered to the rally point, the mechanism will advance to the starting point. Otherwise, the system will repeat the third column until the last point will be reached.

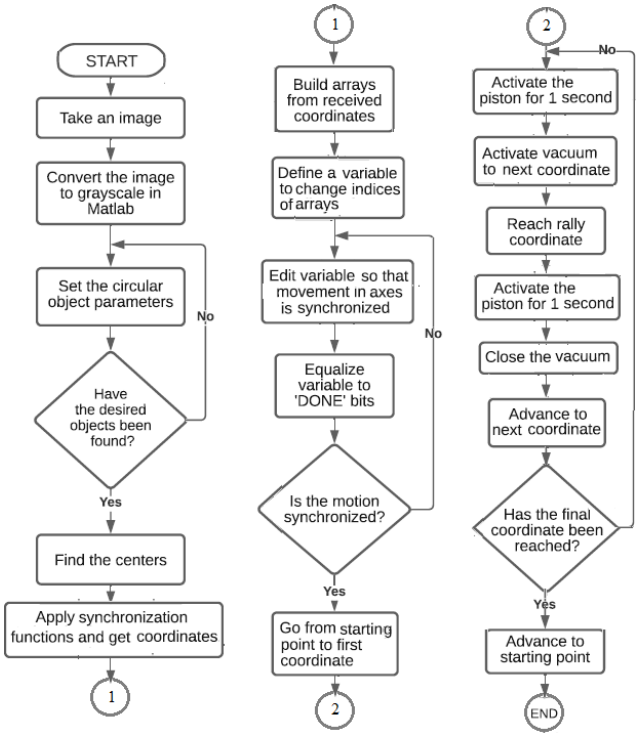

Figure 15. Flowchart of the system algorithm

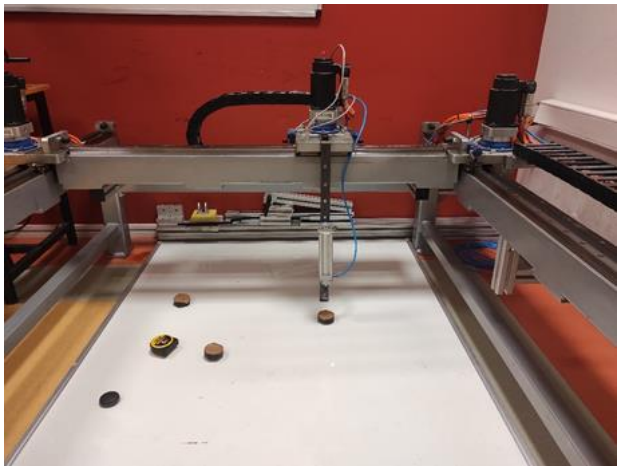

Figure 16. The system reaches the first coordinate received

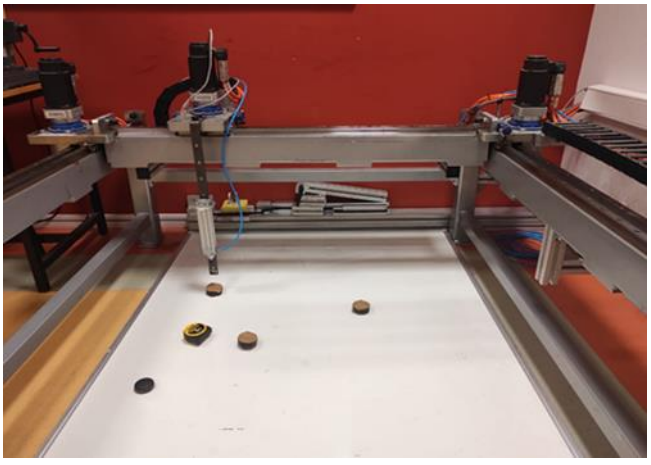

Figure 17. The system reaches the second coordinate received

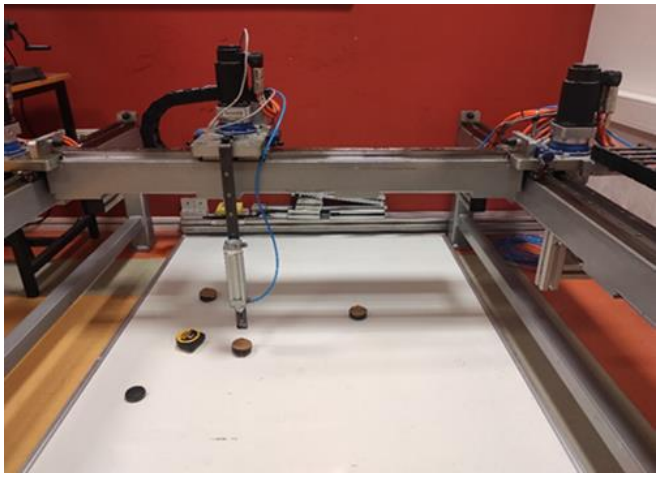

Figure 18. The system reaches the third coordinate received

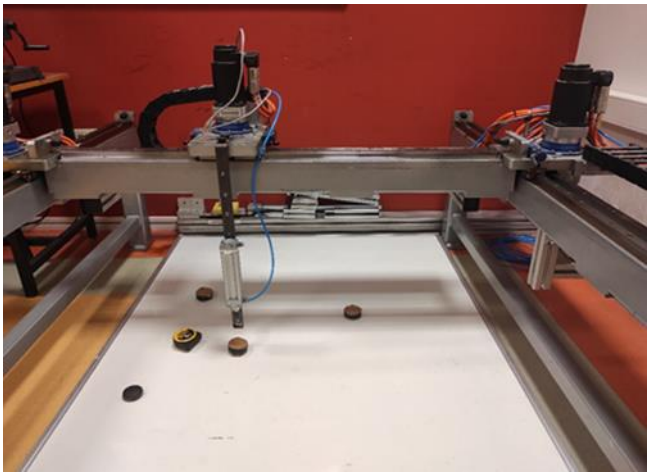

Figure 19. The system reaches the fourth coordinate received

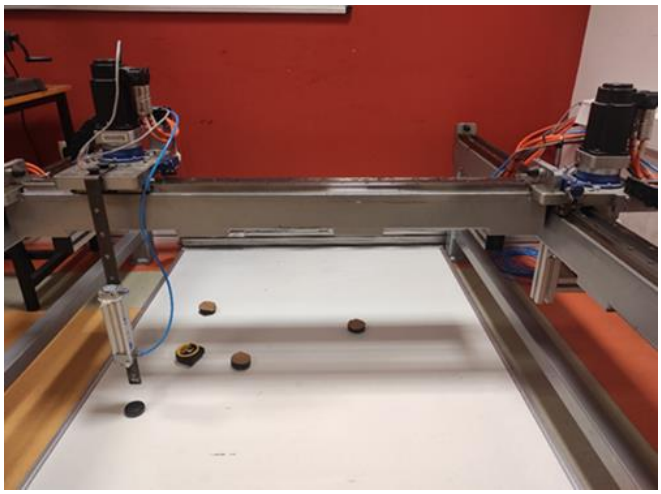

Figure 20. The system reaches the last coordinate received

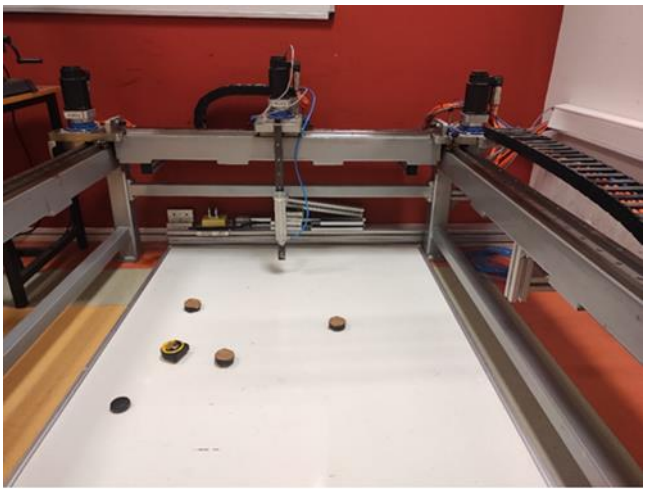

Figure 21. System returns to the initial position

4. CONCLUSION and RESULTS

In this study, it is aimed to create an autonomous system with Bosch-Rexroth PLC, in which the image was taken with an industrial camera, image processing methods in the MATLAB environment, and servo motors and drivers are controlled on the Cartesian machine. With this system, the coordinate data obtained by using image processing methods using the MATLAB program and the coordinates targeted by the PLC were transmitted to the system autonomously. Afterward, a pneumatic system was established and it was aimed to transport the objects to different points. During the study, the results obtained by using the image processing functions, the working logic of the servo motors, and the programming techniques of the PLC systems were made on the setup.

The coordinates of the objects are determined by using image processing methods, and these coordinates are sent to the desired point by using PLC in the Gantry Robot system. A pneumatic system was designed on the y-axis of the Gantry Robot system and the designed system was mounted. Thanks to this pneumatic system integrated into the Gantry Robot system, the objects in the determined coordinates were transported to another coordinate with the help of air. The performance of the system was evaluated by repeating the study on the setup developed for many test applications for different conditions. As a result of the test studies, it has been observed that both the image processing method and the system work simultaneously with high accuracy.

It is known that the Gantry Robot system works in different conditions in many industrial applications and gains high accuracy results to users as their desires. Technological improvements of robotics demand high accuracy with ergonomic designs. This kind of PLC system also can be developed in many different industrial areas. The algorithm can be upgraded or downgraded to wanted spectrums. Thanks to the study, it is thought to be a real-time study that has the potential to be used in many different studies.

Author contributions

Fatma Kuncan: Conceptualization, Methodology, Software, Writing-Reviewing and Editing. Sıtkı Öztürk: Data curation, Writing-Original draft preparation, Software, Validation. Fatih Han Keleş: Visualization, Investigation, Writing-Reviewing and Editing.

Conflicts of interest

The authors declare no conflicts of interest.

REFERENCES

Alekseevic N R (2020). The investigating algorithms of crack position determination based on imagery processing and photogrammetry methods.

Bakır A, Güney Ö F, Kuncan M, Ertunç H M (2012). 3 Eksenli Robot Mekanizmasına Monte Edilmiş Bir Kamera Vasıtasıyla Farklı Rotasyon ve Boyutlardaki Geometrik Cisimlerin Tanımlanarak Vakum Tutucu ile Ayrılması. Otomatik Kontrol Ulusal Toplantısı, Niğde, Turkey, 606-609.

Banafian N, Fesharakifard R & Menhaj M B (2021). Precise seam tracking in robotic welding by an improved image processing approach. The International Journal of Advanced Manufacturing Technology, 114(1), 251-270.

Belgacem I, Jonniaux G & Schmidt F (2020). Image processing for precise geometry determination. Planetary and Space Science, 193, 105081.

Çubukçu A, Kuncan M, İmren M, Erol F, Ertunç H M, Öztürk S & Kaplan K (2015). Görüntü işleme ile 3 eksenli robot mekanizması üzerinde nesne ayırt edilmesi ve sıralanması. Otomatik Kontrol Ulusal Toplantısı. 637-641.

Horoz E, Öten H F, Kuncan M & Ertunç H M (2013). Kamera Yardımı ile Ayırt Edilen ve Tanımlanan Cisimlerin 3 Eksenli Robot Mekanizması ile Taşınması. Otomatik Kontrol Ulusal Toplantısı, Malatya, Turkey, 1236-1240.

Hu X, Deng X & Zhao Q (2021). A gantry robot system for cutting single Y-shaped welding grooves on plane workpieces. Proceedings of the Institution of Mechanical Engineers, Part E: Journal of Process Mechanical Engineering, 235(2), 321-331.

Jose A & Udupa G (2021). Gantry robot system for preventing drowning accidents in swimming pools. Materials Today: Proceedings, 46, 4975-4981.

Kuncan M, Kaplan K, Acar F, Kundakçi I M & Ertunç H M (2016). Fuzzy logic based ball on plate balancing system real time control by image processing. International Journal of Natural and Engineering Sciences, 10(3), 28-32.

Köse İ, Öztürk S, Kuncan M (2019). Pantography application with real-time PLC based on image processing in gantry robot system. European Journal of Technique (EJT), 9(2), 219-229.

Kuncan M & Kaplan K (2016). POSITION DETERMINATION BY USING IMAGE PROCESSING METHOD IN INVERTED PENDULUM. Middle East Journal, 1(2).

Senthilkumaran N, Vaithegi S, (2016). Image Segmentation by Using Thresholding Techniques for Medical Images, Computer Science & Engineering: An International Journal (CSEIJ), 6(1), February 2016.

Şengül Ö, Öztürk S & Kuncan M (2020). Color based object separation in conveyor belt using PLC. Avrupa Bilim ve Teknoloji Dergisi, (18), 401-412.

Priyanto H & Miftahuddin Z (2015). Color-Texture Based Object Tracking Using HSV Color Space and Local Binary Pattern, International Journal on Electrical Engineering and Informatics – 7(2), June 2015.

Vishesh G, Tarun J, Sahil S & Silica K (2017). Specific Color Detection in Images using RGB Modelling in MATLAB, International Journal of Computer Applications (0975 – 8887), 161(8), March 2017.

Turkish Journal of Engineering
https://dergipark.org.tr/en/pub/tuje
e-ISSN 2587-1366

A systematic review study on different kinds of interlocking concrete blocks designs and properties

Ahmad Aswad*[1], Mahmut Cem Yılmaz [1], Salah Haj İsmail [1]

[1]*Ankara Yildirim Beyazit University, Faculty of Engineering and Natural Science, Civil Engineering Department, Ankara, Turkey*

Keywords
Compressive strength
Recycled aggregate
Concrete block
Interlocking

Abstract

Interlocking concrete blocks (ICBs) have been recently used worldwide to be alternative conventional blocks. ICBs are more sustainable, low involve low production cost, and environment-friendly as they emit less carbon dioxide than normal ones. ICBs have been used particularly in war zones and places affected by natural disasters where the need for quick, sustainable, low-cost buildings and earthquake-resistant buildings is indispensable. This paper provides a comprehensive literature review about different types of ICBs. It aims to demonstrate different configurations of ICBs incorporated with recycled concrete aggregate (RCA) and other additive materials used for construction. To achieve this, the compares different related studies which analyse the compressive strength results of RCA mixtures with different RCA replacements, w/c ratio, and mix proportions. Additionally, the paper discusses several techniques and methods to improve the behaviour of ICBs.

1. INTRODUCTION

Construction industries produced enormous amounts of rubbles and demolition waste; some of them are composed of original materials mixed with other wastes that are non-structural usage. Recovering construction and demolition (C&D) waste is divided into two main methods downcycling (backfilling) and upcycling, which generate new materials for construction (Ferriz-Papi & Thomas, 2020).

Rubble recycling has dramatically increased over the last several decades to produce alternative sustainable products. There are different solutions to recycle concrete waste, one of them is using recycled concrete aggregates into an innovative interlocking recycled concrete block (IRCB) to be used in a structural application instead of using conventional concrete. IRCB should be developed to be affordable for normal people live in developing countries using recycled concrete aggregate (RCA), which requires less effort and time during installation.

Generally, concrete blocks are the most common type of concrete structure in industrial construction. Researchers have developed different types of interlocking blocks by using several substitution products. Some of ICB can be built as a structural element such as retaining walls and bearing walls with reduction of mortar called; mortar-less interlocking recycled concrete block wall. IRCBs can provide good compressive strength and feasibility after adding additive materials (ADD) or by-products; and are reinforced with steel bars in the cores, which offer a great lateral, tensile, and shear strength to structures. However, several studies shed light on several structural behaviors of blocks using RCAs (Guo et al., 2018).

2. ADVANTAGES OF IRCB

IRCBs present sustainable solutions and offer several advantages, especially in disaster\war torn countries such as Syria. They are cost and time effective in various construction applications, such as pavements, temporary roads, and structural construction for both low and high-grade applications including columns, beams, and walls by developing different block patterns to be load-bearing blocks.

Some of the proven advantages of IRCB can be stated as follow:

* **Corresponding Author**

*(185110119@ybu.edu.tr) ORCID ID 0000-0001-5497-743X
(mcemyilmaz@ybu.edu.tr) ORCID ID 0000-0003-0670-4095
(sismail@ybu.edu.tr) ORCID ID 0000-0001-6682-6663

Cite this article

Aswad A, Yılmaz M C & Ismail S H (2022). A systematic review study on different kinds of interlocking concrete blocks designs and properties. Turkish Journal of Engineering – 2022; 6(4); 327-337

Review Article / DOI: 10.31127/tuje.931076

Received: 08/05/2021; Accepted: 15/12/2021

- Easy to install.
- Manually assembling requires no specialized masonry labor skills for wall construction.
- Used for both non-structural and structural applications such as column, wall, beam, etc...
- Used to construct single or multi-story buildings. Especially, in rural areas.
- Designed to be used in both horizontal and vertical directions, which gives an aesthetic architectural view of the building.
- Dry laying without mortar, which saves a considerable amount of cement.
- Embedded holes for electrical and plumbing installations.
- Insulating both sound and heat.
- Resistant to earthquakes, especially in disaster-prone countries.

3. LITERATURE REVIEW

Deepak (2012) concentrates on a typical case of interlocking concrete blocks called Hydraform interlocking in India. This type of block was not noticed in the Indian masonry code. For earthquake-resistant buildings, Deepak (2012) argues that grooved inside blocks can be used to strengthen the blocks. The results showed compressive strength was higher than the minimum values obtained in the Indian code (IS 1905-1987) when compared to traditional burnt clay brick. Ali et al., (2012) study some of the mechanical properties of the novel interlocking blocks (top, bottom, standard, and a half) such as shear and compressive strength, which were made of coconut fibre and reinforced concrete. Their study tests several mixed design percentages. The experimental results point that the compressive strength of many blocks is lower than an individual one, and the bottom block's compressive strength, as well as the total compressive toughness, are higher than others. Furthermore, shear strength (out-of-plane) is 25 per cent greater than in the in-plane one. Meanwhile, Sabai et al., (2013) investigate whether recycled aggregates (cementation rubble) could be used like concrete blocks for building construction in Tanzania. They used 100 per cent of recycled aggregate and tested their mechanical, physical, and chemical properties. The results showed the strength of recycled aggregate is weaker than that one made from the natural aggregate, which was the same in Hong Kong. In addition, 85 per cent of concrete block specimens have attained more than 7 N/mm^2 in the compressive strength test, which refers to the possibility to use the rubbles in building construction. Kumar & Vigneshvar (2014) focus on the design of innovative interlocking masonry blocks, which consist of two parts. The first part includes the tongue and groove parts. The second one is projection. These parts can fit each other to align perfectly. However, they have partially substituted fly ash with cement in blocks' production. This particular study aims to build mortar-free structures, which will be earthquake resistant, saving 65 per cent of time and cost, and reducing labor and materials needed for construction. Onyeakpa & Onundi, (2014) refer to the production of a new pattern of interlocking masonry blocks for sustainable construction by using local materials in both urban and rural areas; such as portland cement, water and eliminating of use mortar in construction. The block production was made in different dimensions and shapes (top, bottom, and toe shape) for wall construction and this was produced by standard dual mould. The compressive strength and compaction effort of interlocking concrete blocks are 4.80 (N/mm^2) and 3.687 (KJ/m^3), respectively. Watile et al. (2014) investigate the feasibility of using interlocking blocks incorporation with different additives materials such as sand, fly ash, and stone dust as well as reinforcing manmade fibre material as GFRP (Glass Fibre Reinforce Polymer). According to test results, increasing fly ash content leads to increasing compressive strength of interlocking blocks, absorption as well as density. Water absorption of interlocking blocks without GFRP material was ranged between 6.42 and 12.4 per cent. Meanwhile, the absorption percentage should not be more than 20 per cent in ordinary burnt clay bricks. Thus, using additives materials in interlocking blocks consumes less mortar and achieves better tolerances and efficiency in laying. Sarath et al., (2015a) create a new hollow in an interlocking concrete block that can be reinforced by steel fibres. The block's compressive strength was 6.05 N/mm^2, which was 68 per cent and 14 per cent greater than local ones, respectively. This new pattern of hollow block decreased the dead load by 28 per cent and 11 per cent compared to the local one. Interlocking blocks failures and cracks were developed through face shells, whereas the failures of solid and hollow blocks were developed due to crashing and splitting webs, respectively through the center of the block. Sarath et al. (2015a) investigate a new design of a hollow interlocking concrete block with a proper finish to construct a load-bearing wall that was reinforced with steel fibre. This kind of block has been studied to explore the failure patterns of the masonry wall and comparing the load capacity and the failure patterns to the local solid and hallow ones. The local capacity of the hallow interlocking wall was greater than in local solid and hollow block wall by 12 per cent and 22 per cent respectively. In addition, the steel fibre decreased the dead load by 28 per cent and 11 per cent as opposed to the local one. However, the failure of the interlocking hollow concrete wall was developed from detached face shells, whereas the failure in local ones was failed from joints. Ganesh & Lokeshwaran (2017) reveal the possibility of designing a new interlocking concrete block pattern used in load-bearing and building walls. The experiment was conducted by applying two types of loading on interlocking concrete block walls, compressive strength load, and axial load (uniform distributed load). Results show that the new pattern of interlocking blocks can act as a concrete wall structure and be used in ordinary load-bearing walls, in which the curves show that the block wall failure at maximum load of axial load. Lee et al., (2017) investigate how an innovation reinforced interlocking blocks could be developed to be a structural element and assembled as columns, which could be a replacement for conventional concrete construction. Columns have been tested under axial loads. Researches have conducted a comparison between experimental

results and different code design specifications, such as MSJC code and Eurocode design. They used two types of infills materials grout and concrete. Results have shown that the infills significant connection with column compressive strength by using Pearson and partial correlation analysis, where the differences were between 0.65 – 1.85. The study conducted by Lee et al. (2017) recommended that the height of the reinforcement bar should not exceed 30 mm, and the infill materials' strength should be limited to 50 MPa. In their experiment, Guo et al. (2018) have used 75 per cent recycled concrete aggregate to produce building concrete blocks. The experiment investigated the durability and mechanical properties of these blocks through series of tests. It also compared RCA blocks to conventional blocks in compressive and shear capacity. The experimental results have revealed that concrete blocks incorporation with 75 per cent RCAs weaken the mechanical properties of blocks. Nevertheless, the compressive & shear performance and other mechanical properties such as normal building concrete blocks and the RCA blocks have less environmental impact than conventional ones. The study had indicated that RCA blocks are suitabe and viable to use in multi-story building construction. Safiee et al. (2018) have studied 5 full-scale interlocking masonry walls to investigate their behavior under two combined loads, in-plane lateral load and pre-compressive vertical load. These walls were constructed by using an interlocking mortar-less system. Results have shown that when the pre-compressive load has increased, the lateral load capacity of walls increased. Because of moderate toe crashing or /and diagonal shear failure, walls have failed. However, the developed tie and strut models have a role to give the logical predictions of interlocking wall tested.

Wani & Kumar (2018) have developed a simple kind of interlocking masonry block and discussed the compressive strength result, which is 5.6 – 9.46 as compared to the ordinary one which is 5.4 – 7.54 MPa. The results of this experiment have shown a reduction of up to 80 % in labour cost and quicker in construction. Besides, the experiment eliminated bed mortar and thereby it led to removing biaxial lateral tensile stresses in masonry units. Pavlu et al. (2019) have developed concrete mixtures incorporation with different substitutional materials. They have replaced quantities of two materials for building mortar-less masonry walls; the first material was recycled concrete aggregate RCA and the second one was recycled expanded polystyrene EPS. They have applied several tests on ten concrete mixtures and investigated their mechanical and thermal properties. Results have shown that by using recycled aggregate in place of natural aggregate, the thermal conductivity of concrete will increase; (almost 70 per cent lower than what was founded in ordinary concrete), but influenced negatively on the mechanical properties (e.g. the compressive strength has declined between 30 per cent to 75 per cent depending on the replacement rates).

4. REVIEW OF DIFFERENT DESIGN OF INTERLOCKING BLOCK

- **CFRC interlocking block**

- Dimention: standard block (400 × 200 × 195) mm.
- Using coconut fiber reinforced concrete for load-bearing and earthquake-resistant structures.
- Average compressive strength (MPa) of (standard, top, bottom and half) blocks is 16.48, 17.02, 7.73, and 8.66, respectively.
- Average compressive strength (MPa) of stacked standared blocks is 15.78.
- Reference: (Ali et al., 2012)

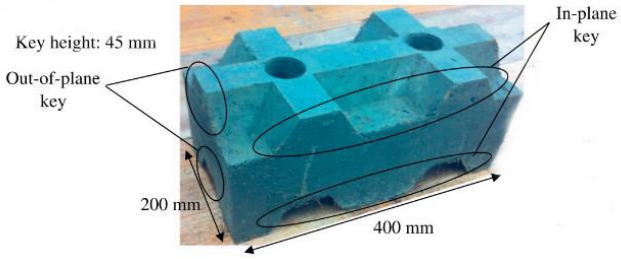

Figure 1. Coconut fiber reinforced concrete intrlockimg block

- **Interlocking lightweight cement block**

- Dimension: (600 x 200 x 200) mm.
- Using expanded polystyrene beads to reduce the self-weight.
- Designing for load-bearing masonry walls.
- Average compressive strength (MPa) of block and Wall panel strength is 4.91 and 2.13 Mpa, respectively.
- Reference: (Sayanthan et al., 2013)

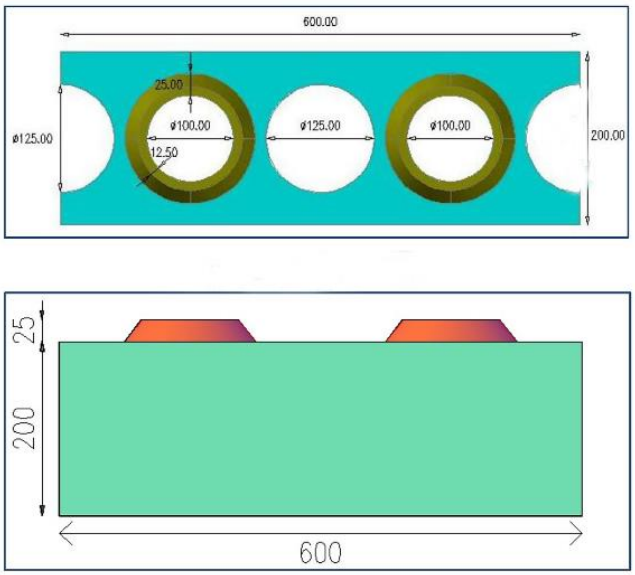

Figure 2. Interlocking lightweight cement block

- **Haener block** (U.S and Canada)

- Dimension: standard block (406.4 x 203.2 x 203.2) mm.
- Haener is a Mortarless interlocking block system.
- The main Block has three cavities, and it can be designed with only one cavity for insulation purposes.

- using Haener's two-block system to build walls and columns as well.
- Reference: (Haener, 2005)

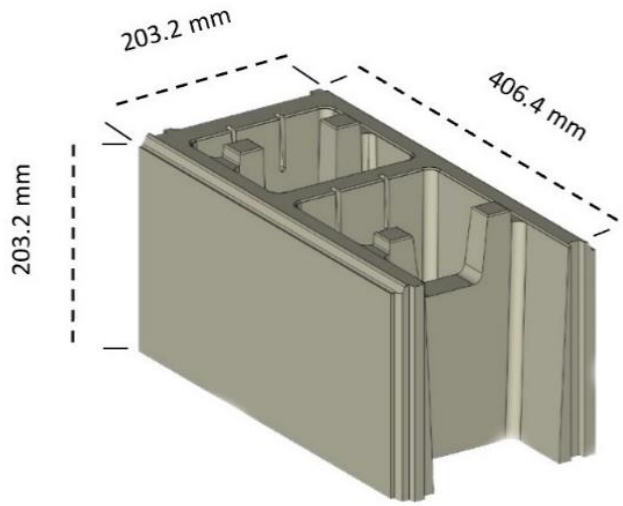

Figure 3. Haener block

- **Thai interlocking brick** (Bangkok)

- Dimension: (300 x 150 x 100) mm.
- It has vertical grooves and holes to reduce the weight that can reinforce to increase wall stability and can be used for electrical conduits.
- Reference: (Kintingu, 2009)

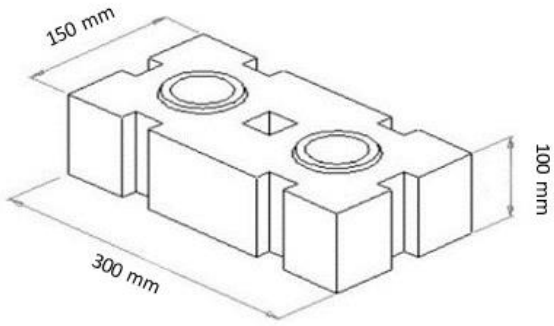

Figure 4. Thai interlocking brick

- **Putra block** (Malaysia)

- Stretcher block dimension: (300×200×150) mm.
- Average compressive strength (MPa) of (stretcher, half, and corner) blocks are 22.85, 22.02, and 23.67, respectively.
- Putra blocks were designed to explore the structural behavior of Putra block wall under out-of-plane load.
- Reference: (Safiee et al., 2018)

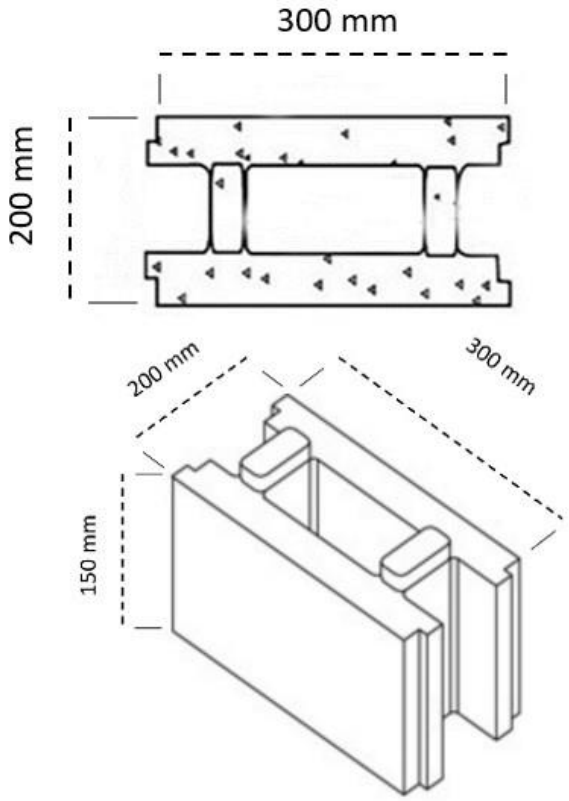

Figure 5. Putra block

- **Steel fibre reinforced concrete hollow block**

- Dimension: (600 × 200 × 300) mm.
- Using hooked end steel fibers in casting hallow blocks as a load-bearing wall.
- Using concrete cube of M10 grade (150 x 150 x 150) mm.
- After 28 days, the block's compressive strength is 6.05 Mpa.
- Reference: (Sarath et al., 2015b)

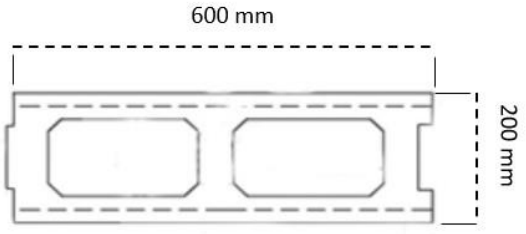

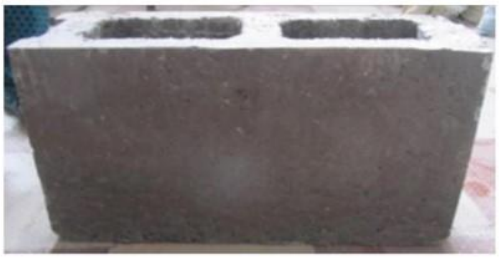

Figure 6. Steel fibre reinforced concrete hollow block

- **Interlocking concrete block**

- Dimension: (400 × 200 × 200) mm.
- Designing for a load-bearing wall (shear wall).
- Using concrete cube of M40 grade (150 x 150 x 150) mm.
- After 28 days, the block's compressive strength is 52.15 Mpa.
- Reference: (S. Jai Ganesh & Lokeshwaran, 2017)

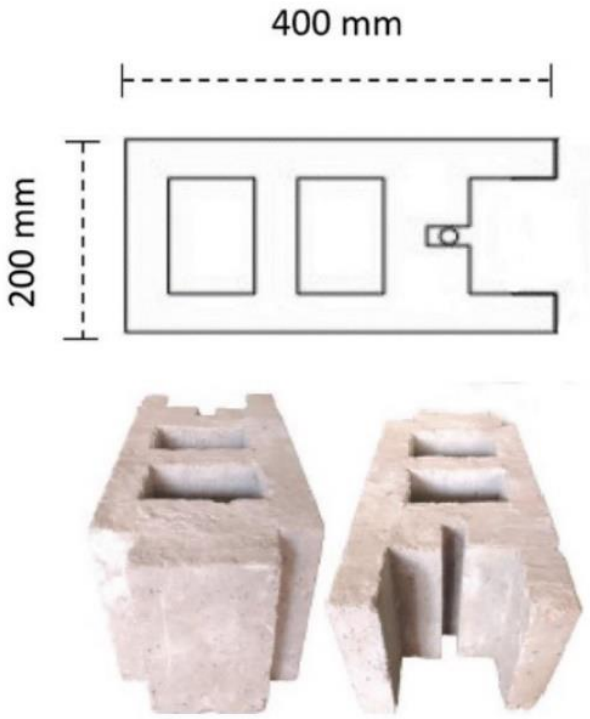

Figure 7. Interlocking concrete block

- **Tanzanian interlocking brick (TIB)**

- Dimension: full brick (300 x 150 x 100) mm.
- The key locking knops & depression are two and they are in pyramids shape with holes.
- Reference: (Kintingu, 2009)

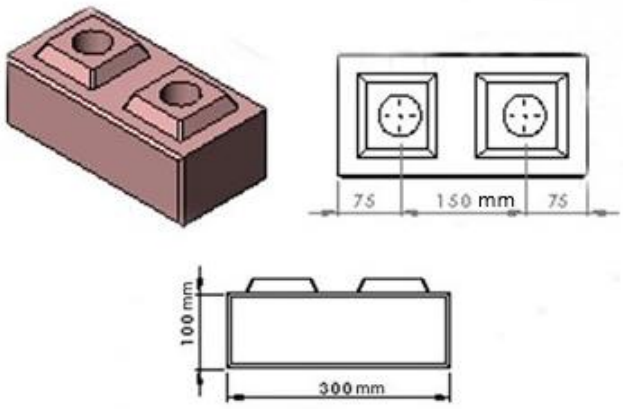

Figure 8. Tanzanian Interlocking Brick

- **Interlocking brick system**

- Dimension: standard (250 x 125 x 100) mm
- Aiming to reduce using more structural reinforced concrete reinforced elements.
- U-shape used as a supporting element of wall construction.
- Grade of mixing concrete design 35
- Compressive strength at 28 d: 35 Mpa.
- Reference: (Mirasa & Chong, 2020)

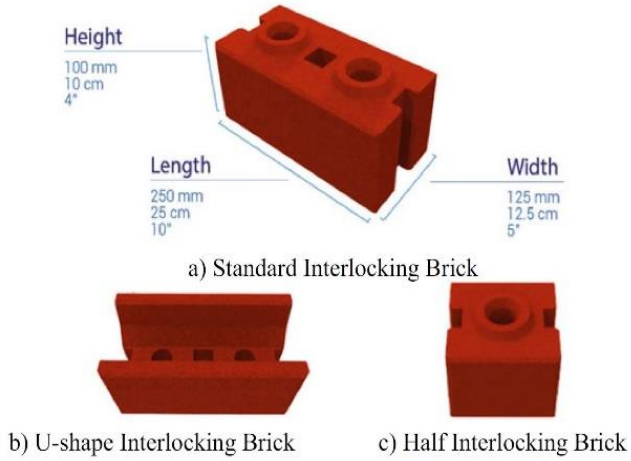

Figure 9. Interlocking brick system

- **Hollow concrete interlocking blocks**

- Dimension: full block (400 x 190 x 200) mm.
- Mortarless masonry system: MMS compressive Strength data:
 *Average strength unit: 40 Mpa.
 *Average strength masonry: 30.67 Mpa.
- Reference: (Zahra & Dhanasekar, 2018)

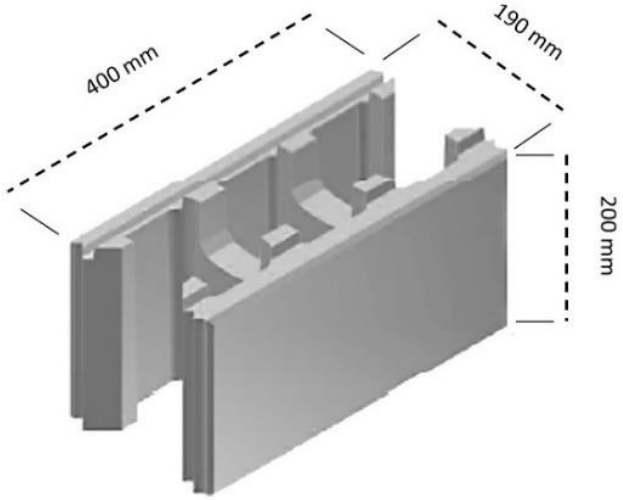

Figure 4. Hollow concrete interlocking block

5. REVIEW OF (RAC) MIXTURES

Table 1. Review of various RAC mixtures

Reference	Mix proportion			Specimens	Mould Type	Curing (Day)
	Concrete Class	W\C Ratio	RCA Replacement %			
(Opara et al., 2016)	\	0.5	(0 -100)	12 specimens for each replacement rate	Cube (150x150x150 mm)	28
(Abdel-Hay, 2017)	\	0.55	(0-25-50-100)	3 specimens for each test	Cube (150x150x150 mm) for C.S[1]	28
(Hamad & Dawi, 2017)	C28 C60	0.57 0.33	(0-20-40-60-80-100)	6 for each concrete strength type.	Cylinder 150 ×300 mm	28
(Ozalp et al., 2017)	C25\30 C30\37	\	(10-15-20) for each series	Two series, each one has three specimens	Cube (150x150x150 mm)	28
(Taffese, 2018)	C25/35 C35/45	0.61 0.55	(0-10-20) for each group	Two groups, each group has three mixes	Cylinder 150x300 mm for C.S	28
(Zheng et al., 2018)	C25 C50	0.55 0.35	(0-25 -50 -75-100) for each concrete grade	6 for each mix	Cube (100x100x100 mm)	28
(Ozbakkaloglu et al., 2018)	C40 C80	0.62 0.36	(0-25-50-100)	14 batches, 3 specimens for each mix and test	Cylinder (100x200) mm for C.S	28
(Pavan et al., 2018)	M20	0.5	(0-25 -50 -75-100) for each mould type	6 for two concrete strength type	Cube & Cylinder	28
(Pacheco & de Brito, 2019)	C25 C50 C100	0.535 0.538 0.544	(0-25-50-100)	39 specimens	Standard Cube	28
(Ajmani et al., 2019)	\	0.31	(20-50-80)	36 cube SP. for C.S,	Cube	28

[1] Compressive strength

6. COMPRESSIVE STRENGTH OF MIXTURES AND INTERLOCKING CONCRETE BLOCKS

Table 2. Review of compressive strength of mixtures

Compressive strength of Mixtures containing RCA (Mpa)						
Reference number	Reference	25%	30%	40%	50%	60%
1	(Pavan et al., 2018)	25.5			27.8	
2	(Abdel-Hay, 2017)	28.1			30	
3	(Zheng et al., 2018)	24.9			23.7	
4	(Nagaraja et al., 2017)	26.55	21.1		18.66	
5	(Manasa et al., 2019)	29.2			27.98	
6	(Hamad & Dawi, 2017)			31.4		31.6
Compressive strength of Mixtures containing RCA and ADD (Mpa)						
Reference number	Reference	25%	30%	40%	50%	60%
7	(Ozbakkaloglu et al., 2018)	41			40.5	
8	(Pacheco & de Brito, 2019)	51.1			48.2	
9	(Nagaraja et al., 2017)	26.89			22.44	
10	(Tembhurne et al., 2018)			46.7		42.7
11	(Pavlu et al., 2019)					
12	(Pavlu et al., 2019)					
13	(Akhtar & Sarmah, 2018)		46.9		33.2	
14	(Akhtar & Sarmah, 2018)				44.1	

Table 3. Review of compressive strength for interlocking concrete blocks

Compressive strength of ICB containing NCA (Mpa)			Compressive strength of ICB containing ADD (Mpa)			
Reference number	Reference	25%	Reference number	Reference	30%	40%
15	(Safiee et al., 2018)	22.85	20	(Sabai et al., 2013)	9.4	
16	(Ali et al., 2012)	16.48	21	(Guo et al., 2018)	9.38	
17	(Lee et al., 2017)	14.28	22	(Sarath et al., 2015a)		6.05
18	(Sabai et al., 2013)	14.2	23	(Sayanthan et al., 2013)		4.91
19	(Guo et al., 2018)	9.86				

6.1 RESULTS and DISCUSSION

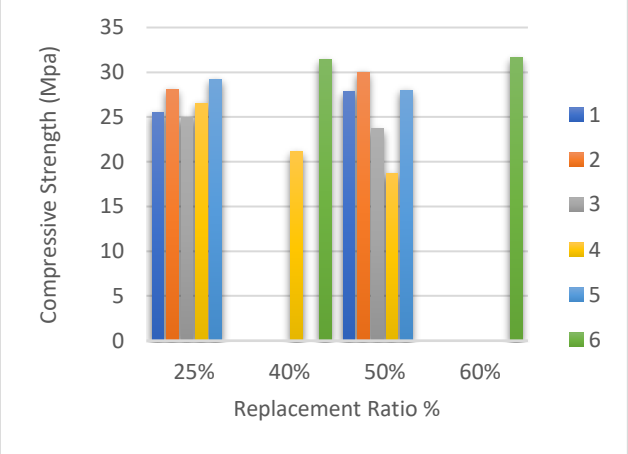

Figure 5. Compressive strength of mixtures containing RCAs

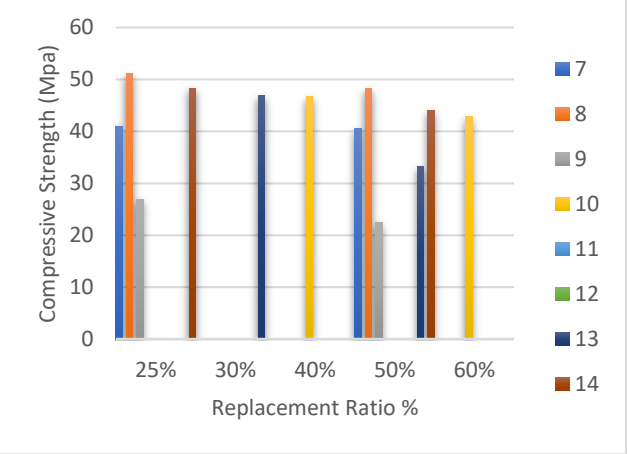

Figure 6. Compressive strength of mixtures containing NCA

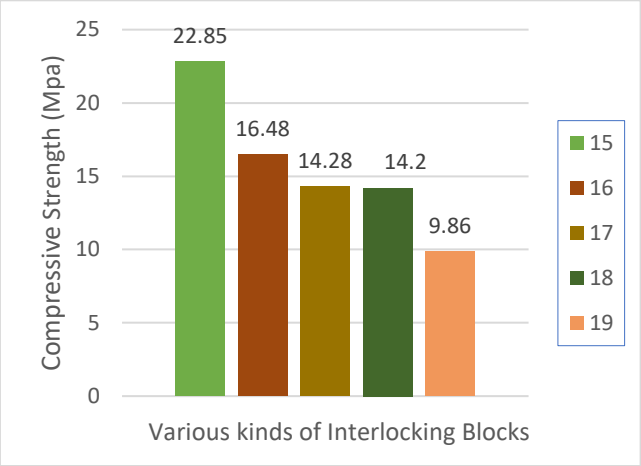

Figure 7. Compressive strength of ICBs containing RCAs & Additives

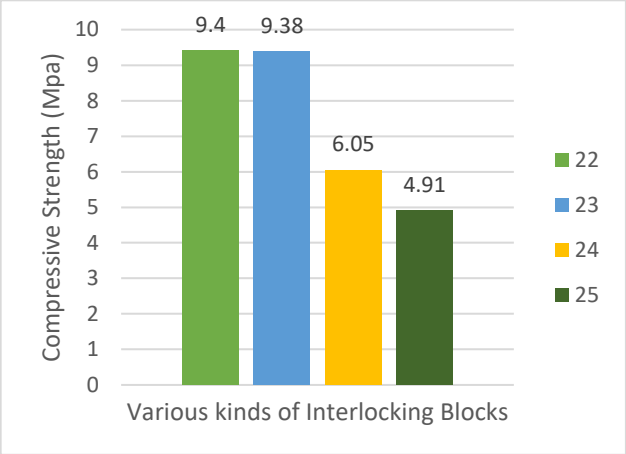

Figure 8. Compressive strength of ICBs containing RCA & Additives

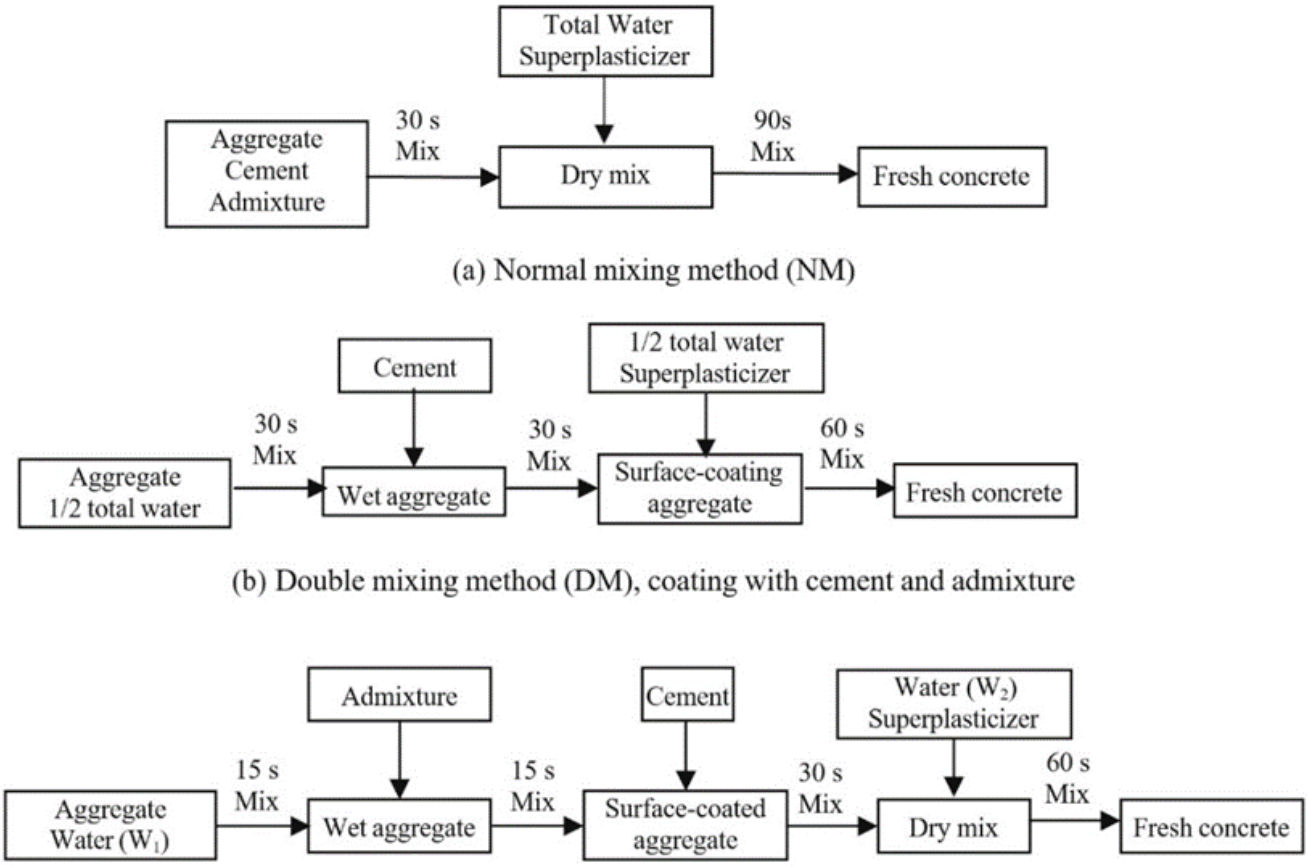

Figure 9. Double and Triple mixing methods of NAC and RAC (Kong et al., 2010)

Results in figures [14,15] show the compressive strength of mixtures containing RCA with NCA. They are ranged between 20 to 35 per cent, but they increased when adding additive materials to RCA which ranged between 25 to 50 per cent.

The bar graphs in the figures [16,17] show the changes in compressive strength by adding RCAs alone and additive materials. They demonstrate that compressive strength is increasing gradually according to the design of block pattern and the source of RCA & additive materials.

Based on previous test results, the compressive strength of interlocking concrete blocks containing RACs & additives decreased approximately between 10 to 25 per cent compared to ICB & NAC. However, researchers point out different methods to improve the strength of RAC. There are techniques classified into 2 main categories according to Purushothaman et al. (2015) and Shaban et al. (2019), the first one is eliminating adhered mortar and the second one is improving the quality of adhered mortar:

1- Eliminating adhered mortar

- Physical treatment: containing several treatments as thermal, mechanical, and thermal/mechanical.
- Chemical treatment: containing different treatments such as acid soaking.

2- Improving the quality of adhered mortar

- Physical treatment

- Polymer treatment has different solutions such as polyvinyl alcohol solution and repelled water absorbed).
- Calcium carbonate bio deposition.

- Chemical treatment

- Pozzolanic and cementitious materials such as granulated blast, furnace slag, silica fume, natural pozzolan, and metakaolin. Some of these can increase the strength between 5 to 15 per cent.
- Carbonation.
- Sodium silicate.
- Polymer treatment.

Besides, other additive materials could be used in treatments:

- limestone filler and recycled masonry aggregate.
- Steel fibres.

Furthermore, there are other techniques to enhance strength of concrete mixture such as mixing techniques:

- ❖ Normal, double, and triple mixing methods:
- ❖ Packing density mix method:

"The packing density of the aggregate mixture is defined as the solid volume in a unit total volume. The aim of obtaining packing density is to predict the number of aggregates used in the mixture and to minimize porosity and reduce the amount of cement used in the concrete" (Huang et al., 2017).

7. CONCLUSION

This review paper has discussed multiple points based on different design patterns of ICB as well as reviewing more than 40 journal papers that are related to the study. According to previous papers, the compressive strength of ICB is affected by several factors:

- RCA replacement ratio: the higher percentage of RCA leads to the lower compressive strength of RAC because the link between old mortars and new ones was weak.
- W/C ratio: RAC compressive strength has decreased when the w/c ratio increased.
- Age and Source of RCA.
- Type of additive material, replacement ratio of additive material, and ICB design as well.

These experimental studies clearly illustrate that first the appropriate replacement ratio of RCA has an efficient role in increasing the strength, which ranges between 20 to 35 per cent of concrete mixture for structural applications. Second, adding additives such as pozzolanic materials especially those materials containing silica to the RAC mixture at 28 days will improve ompressive strength by 23 per cent.

Third, different kinds of treatments such as calcium carbonate bio deposition could make improvement up to 40 % , but it will take more cost and time, and it won't be applicable for large scale according to (Shaban et al., 2019).

8. FUTURE STUDY

The review study is the first step towards the design and experiments of interlocking block dry-stack wall system with RCA from debris. The aim is to check the possibility for its structural use in post-war/disaster reconstruction processes.

An interlocking dry-stack block system can be used with a minimal amount of mortar. The interlocking mechanism allows blocks to lay on cement slurry not on mortar to provide resistance to different loads; ICBW can be assembled at least three times faster than an ordinary block wall (Guo et al., 2018). Masonry dry-stack system based on blocks that interlock with grooves and tongues to provide appropriate alignment in construction. This wall system will be resistant to several external forces, especially when it is reinforced by steel rods through holes. A dry-stacking wall system would allow eliminating the cracks of shrinkage issues on a concrete wall (Zahra, 2017).

Design:

This system has different block configurations. Each block has an interlocking key at its both top and sides in the long direction:

- Standard block (Dim: 400 x 200 x 200 mm).
- Half stretcher block is used for special situations that will arise in the field.
- Right & left corner block is used for corners.
- Quarter block is used when the wall needs to end correctly.
- The bottom U-shape block like a channel is used as a supporting element for the wall, which has the same shape and holes as the standard one.

Experimental process:

The experimental study will focus on the structural behaviour for both individual blocks and the block wall. The compressive strength, shear strength, flexural strength of RAC interlocking block, and wall will be tested to investigate the failure mode, load-bearing, damage process, and deformation shape on ICB and ICB walls.

It will be 3 series of groups; each group has three types of concrete mixtures that will be tested with different replacement ratios of NCA:

- Replacement ratios suggestions:

30 % RM (25% RCA + 5% ADD) + 70 NCA
40 % RM (30% RCA + 10% ADD) + 60 NCA
50 % RM (35% RCA + 15% ADD) + 50 NCA

- W/C ratio: 0.5 for concrete grade C25

Finally, this wall system could be provided with an insulation material for exterior and interior sides as expanded polystyrene.

Abbreviations

- NCA: Natural concrete aggregate
- RCA: Recycled concrete aggregate
- RAC: Recycled aggregate concrete
- ADD: Additive material
- ICB: Interlocking concrete block
- IRCB: interlocking recycled concrete block
- W/C: water-cement ratio
- C&D: Construction and demolition
- STS: splitting tensile strength
- CS: Compressive strength
- Ref: Reference
- RM: Recycled materials

Author contributions

Ahmad Aswad: Draft preparation, Investigation, Visualization, Writing**. Mahmut Cem Yılmaz:** Conceptualization, planning, literature review, Editing**, Salah Hajismail:** Methodology, Data curation, Review, proof reading.

Conflicts of interest

The authors declare no conflicts of interest.

REFERENCES

Abdel-Hay A S (2017). Properties of recycled concrete aggregate under different curing conditions. HBRC Journal, 13(3), 271–276.

Ajmani H Al, Suleiman F, Abuzayed I & Tamimi A (2019). Evaluation of concrete strength made with recycled aggregate. Buildings, 9, 1–14.

Akhtar A & Sarmah A K (2018). Construction and demolition waste generation and properties of recycled aggregate concrete: A global perspective. Journal of Cleaner Production.

Ali M, Gultom R J & Chouw N (2012). Capacity of innovative interlocking blocks under monotonic loading. Construction and Building Materials, 37, 812–821. 002

Deepak B (2012). Sustainable Dry Interlocking Block Masonry Construction. 15th International Brick and Block Masonry Conference. Brazil, 1–11.

Ferriz-Papi J A & Thomas S (2020). Recycled Aggregates from Construction and Demolition Waste in the Production of Concrete Blocks. Journal of Construction Materials, 2(1).

Ganesh S Jai & Lokeshwaran N (2017). Experimental investigation on behavior of shear wall assembled with interlocking concrete block. International Journal of Civil Engineering and Technology (IJCIET), 8(3), 111–117.

Guo Z, Tu A, Chen C & Lehman D E (2018). Mechanical properties, durability, and life-cycle assessment of concrete building blocks incorporating recycled concrete aggregates. Journal of Cleaner Production.

Haener J A (2005). Two piece interlocking block system (Patent No. 20060150559).

Hamad B S & Dawi A H (2017). Sustainable normal and high strength recycled aggregate concretes using crushed tested cylinders as coarse aggregates. Case Studies in Construction Materials, 7(August 2017), 228–239.

Huang Q, Lin L, Tan E L & Singh B (2017). Mix Design of Recycled Aggregate Concrete Using Packing Density Method. 1st International Conference on Structural Engineering Research (ICSER 2017), 8.

Kintingu S H (2009). Design of interlocking bricks for enhanced wall construction, flexibility, alignment accuracy and load bearing [Warwick university].

Kong D, Lei T, Zheng J, Ma C, Jiang J & Jiang J (2010). Effect and mechanism of surface-coating pozzalanics materials around aggregate on properties and ITZ microstructure of recycled aggregate concrete. Construction and Building Materials, 24(5), 701–708.

Kumar T P & Vigneshvar R (2014). Development of an Innovative Interlock Blocks. Journal of Civil Engineering and Environmental Technology Print, 1(5), 114–118.

Lee Y H, Shek P N & Mohammad S (2017). Structural performance of reinforced interlocking blocks column. Construction and Building Materials, 142, 469–481.

Manasa S, Udaybhaskar M & Kumar G N (2019). Performance of Recycled Aggregate Concrete for M25 Grade Concrete. International Journal of Engineering and Advanced Technology (IJEAT), 9(2).

Mirasa A K & Chong C-S (2020). The Construction of Green Building Using Interlocking Brick System. In A. Z. Yaser (Ed.), Green Engineering for Campus Sustainability (pp. 35–49). Springer Nature Singapore.

Nagaraja Ba, Vinay K V A, Keerthi Gowda B S, & Karisiddappa B. (2017). A study on slump and compressive strength of recycled aggregates embedded concrete. Innovations & Advances in Civil Engineering and Earth Science At: Chamarajanagar, Karnataka, India.

Onyeakpa C & Onundi L (2014). Improvement on the Design and Construction of Interlocking Blocks and

its Moulding Machine. IOSR Journal of Mechanical and Civil Engineering, 11(2), 49–66.

Opara H E, Eziefula U G & Ugwuegbu C C (2016). Experimental Study of Pervious Concrete Using Recycled Coarse Aggregate. International Journal of Materials and Structural Integrity, 10(4), 123–132.

Ozalp F, Yilmaz H D, Aydin O F, Kara M & Kilic Y (2017). Effects of using recycled concrete as aggregate on the engineering properties of concrete. National Symposium on the Use of Recycled Materials in Engineering Construction Journal, 9.

Ozbakkaloglu T, Gholampour A & Xie T (2018). Mechanical and durability properties of recycled aggregate concrete: Effect of recycled aggregate properties and content. Journal of Materials in Civil Engineering, 30(2), 13.

Pacheco J & de Brito J (2019). Structural reliability of recycled aggregate concrete. In New Trends in Eco-efficient and Recycled Concrete. Woodhead Publishing.

Pavlu T, Fortova K, Divis J & Hajek P (2019). The utilization of recycled masonry aggregate and recycled EPS for concrete blocks for mortarless masonry. Materials, 12, 1923.

Purushothaman R, Amirthavalli R R & Karan L (2015). Influence of treatment methods on the strength and performance characteristics of recycled aggregate concrete. Journal of Materials in Civil Engineering, 27(5).

Pavan P S, Babitha Rani H, Deepika Girish, Raghavendra K M, Vinod P N, Dushyanth.V.Babu.R ,& Shaik Numan (2018). A study on recycled concrete aggregates. International Journal of Pure and Applied Mathematics, 118(18), 3239–3263.

Sabai M M, Cox M G D M, Mato R R, Egmond E L C & Lichtenberg J J N (2013). Concrete block production from construction and demolition waste in Tanzania. Resources, Conservation and Recycling, 72, 9–19.

Safiee N A, Nasir M, N A, A, & A F, & Abu Bakar N (2018). Behaviour of interlocking mortarless hollow block walls under in-plane loading. Australian Journal of Structural Engineering, 19(2), 87–95.

Sarath P, Pradeep P, & Shemy S. Babu. (2015a). Investigation on Strength Parameters of Interlocking Hollow Block Strengthened with Steel Fibres. Journal of Engineering Research and Applications, 5(8), 111– 117

Sarath P, Pradeep P & Shemy S B (2015a). Performance of Steel Fibre Reinforced Interlocking Hollow Block as Load Bearing Wall. IOSR Journal of Mechanical and Civil Engineering, 12(5), 38–46.

Sayanthan R, Ilamaran S, Rafiudeen M R & Nanayakkara S M A (2013). Development of Interlocking Lightweight Cement Blocks. In Special Session on Construction Materials & Systems, 4th International Conference on Structural Engineering and Construction Management 2013, Kandy, Sri Lanka, December, 194–202.

Shaban W M, Yang J, Su H, Mo K H, Li L & Xie J (2019). Quality improvement techniques for recycled concrete aggregate: A review. Journal of Advanced Concrete Technology, 17, 151–167.

Taffese W Z (2018). Suitability Investigation of Recycled Concrete Aggregates for Concrete Production: An Experimental Case Study. Advances in Civil Engineering, 2018, 11.

Tembhurne R S, Makwana M M & Kulkarni M S (2018). Strength & Durability Parameter of Recycled Concrete Aggregate. International Journal of Science Technology & Engineering, 5(3), 1–10.

Wani M V & Kumar C (2018). Behaviour of Interlocking Hollow Concrete Blocks. International Journal of Trend in Scientific Research and Development (IJTSRD), 2(4).

Watile R K, Deshmukh S K & Muley H C (2014). Interlocking brick for sustainable housing development. International Journal of Science, Spirituality, Business and Technology (Ijssbt), 2(2), 58–64.

Zahra T (2017). Strategies for Improving the Response of Drystack Masonry to Compression. Queenland University of Technology.

Zahra T & Dhanasekar M (2018). Characterisation and strategies for mitigation of the contact surface unevenness in dry-stack masonry. Construction and Building Materials, 169, 612–628.

Zheng C, Lou C, Du G, Li X, Liu Z & Li L (2018). Mechanical properties of recycled concrete with demolished waste concrete aggregate and clay brick aggregate. Results in Physics, 9, 1317–1322.